TECHNICAL REPORT 703-8

NASA CR 109724

AN INVESTIGATION OF TANDEM ROW HIGH HEAD PUMP INDUCERS

By

Robert J. Etter and C. C. Hsu

February 1970

HYDRONAUTICS, incorporated
research in hydrodynamics

Research, consulting, and advanced engineering in the fields of NAVAL and INDUSTRIAL HYRODYNAMICS. Offices and Laboratory in the Washington, D. C., area: Pindell School Road, Howard County, Laurel, Md.

TECHNICAL REPORT 703-8

AN INVESTIGATION OF TANDEM ROW HIGH HEAD PUMP INDUCERS

By

Robert J. Etter and C. C. Hsu

February 1970

INTERIM REPORT
(Phase II)

Prepared Under
National Aeronautics and Space Administration
George C. Marshall Space Flight Center
Huntsville, Alabama
Contract No. NAS 8-20625

TABLE OF CONTENTS

LIST OF FIGURES

LIST OF TABLES

NOTATION

A	Real constant
B	Real constant
B_{nm}	Constant
C	Chord
CAPC	Transformed chord length
C_F	Force coefficient
C_L	Lift coefficient
$C_{L_{camber}}$	Lift coefficient due to camber
C_{L_α}	Lift coefficient due to angle of attack
C_N	Normal force coefficient
C_p	Pressure coefficient
C_ξ, C_η, C_θ	Dimensionless axial, radial, and tangential velocities
D	Foil spacing in cascade, diffusion factor
D_h	Hub diameter
D_m	Model diameter
D_p	Prototype diameter
D_t	Tip diameter
F	Face
FTYPE	Foil type

H	Head
$H(\zeta)$	Fundamental solution
J_m	Bessel function of the first kind
K	Ratio of model stress to prototype stress
K_o, K_1, K_2	Coefficients in streamline equation
LH_2	Liquid Hydrogen
LOX	Liquid Oxygen
N	Integer
NPSH	Net positive suction head
N_s	Specific speed
N_{ss}	Suction specific speed $n\sqrt{Q}/NPSH^{\frac{3}{4}}$
$P(\zeta)$	Rational function
Q	Discharge or $\sqrt{(\cosh \gamma_o)^2 - \sin^2\beta}$
V	Velocity
V_{f_o}	Axial velocity upstream of hub
V_u	Swirl velocity
w_1	Inlet velocity
w_2	Outlet velocity
Y_m	Bessel function of the second kind

$Z_m = J_m + B_{nm} Y_m$

a	Hub radius, vortex spacing, or scaling parameter for partially cavitating blades
b	Casing radius
b/a	Cascade parameter (Ref. 15)
c	Chord
c/d	Solidity
d	Foil spacing in cascade
g	Acceleration due to gravity
i	Imaginary number, $\sqrt{-1}$
k_2, k_3, k_5, k_c	Camber coefficients
ℓ/c	Cavity length/chord length ratio
ℓ/d	Cavity length/foil spacing ratio
m	Integer
n	Integer, rotational speed in RPM, or number of blades
n_m	Rotational speed in model, RPM
n_p	Rotational speed in prototype, RPM
r	Radial coordinate
s	Cavity length in transformed plane (partially cavitating)
t	Transformed dummy variable
$t_{.20}$	Foil thickness at the 20 percent chord
u	Velocity
u_c	Velocity on cavity boundary
u_t	Tip speed

u_1	Approach velocity to cascade
u_2	Velocity far downstream of cascade
v	Velocity
$w(x,y)$	Complex velocity potential
x	Axial coordinate
y_f	Face coordinate of blade
$z = x + iy$	complex coordinates in z-plane
Γ	Circulation
Γ_b	Blade circulation
Φ	Dimensionless velocity potential
α	Angle of attack
α_2	Direction of flow far downstream of cascade
β	Stagger angle
β_n	Mean flow angle relative to axial direction
β_{nm}	Constant
β_1	Inflow angle relative to axial direction (stagger angle)
β_2	Outflow angle relative to axial direction
γ	Central angle of a circular foil
γ_{nm}	Constant
$\gamma_o = \ell n \ (b/a)$	
$\zeta = \xi + i\eta$	Complex coordinates in ζ-plane
$\bar{\zeta} = \xi - i\eta$	Complex conjugate
η	Efficiency, or dimensionless radial coordinate, r/b

η_H	Hub ratio, a/b
θ	Angular coordinate
μ_{nm}	Dimensionless Eigenvalue, $\lambda_{nm}a$
ξ	Dimensionless axial coordinate, x/b
ξ_t	Axial extent
π	3.14159
ρ	Fluid mass density
ρ_m	Fluid mass density in model
ρ_p	Fluid mass density in prototype
ρ_1	See Equation [2e]
ρ_2	See Equation [2f]
σ	Cavitation number or stress
$\sigma_{B.M.}$	Stress due to bending moment
σ_ℓ	Local cavitation number
σ_m	Model stress
σ_p	Prototype stress
Φ	Scaling parameter for partially cavitating blades
Φ_o	Flow coefficient, V_{f_o}/u_t
ψ	Head coefficient, GH/u_t^2
ψ_1	See Equation [2g]
ψ_2	See Equation [2h]
ω	Rotational speed, radians/sec. or complex velocity potential
∞	Infinity

ABSTRACT

The present work is a continuation and expansion of an investigation of tandem row high head pump inducers in which the first stage is designed to be supercavitating at the design operating point. Previous work (1) utilized first stages with constant pressure camber and second stages designed using a method (4) which does not require theoretical or experimental cascade performance data. In the present report, supercavitating cascades having cambers other than constant pressure are studied theoretically and the results compared to existing experimental data. The "five term" cambered shape is shown to be particularly suited to first stage inducer application. Other types considered include flat plate, circular arc, two term cambered, and three term cambered shapes. The performance of partially cavitating cascades is also formulated and the necessary expressions are presented to calculate the significant performance parameters. A study of the three-dimensional velocity field generated by a radial vortex filament in a cylindrical annulus is presented. This study provides the basic data required to use the second stage design technique for a larger range of hub/diameter ratios than previously available. Using the vortex filament study, refinements in second stage interference streamline calculations are developed. Finally a first stage inducer design is presented utilizing the five term cambered shape and a 0.60 hub/diameter ratio. A matching second stage having a 0.70 hub/diameter ratio is also designed and presented.

1.0 INTRODUCTION

A detailed introduction to the problems and motivation for the program of theoretical and experimental investigations into tandem row inducer pumps is presented in HYDRONAUTICS, Incorporated Technical Report 703-4 — the Interim Report on Phase I of the project (1). The present report on Phase II is a continuation of the same investigation incorporating many of the recommendations for further study resulting from the Phase I work.

To briefly summarize the background and motivation:

(a) "Inducers" preceding main fuel/oxidizer pumps in rocket applications allow operation of the systems at higher values of suction specific speed (lower inlet pressures and higher speeds).

(b) High suction specific speed operation allows lower propulsion system weight and, therefore, larger payloads.

(c) While operating under these conditions, the inducers (usually high solidity, axial flow impellers with helical blades) cavitate and under some conditions experience violently unsteady flow regimes leading to unsteady discharge and ultimately unsteady thrust.

(d) One solution which has been proposed to help reduce the tendency toward unstable flow is a tandem-row inducer with the first stage developing only part of the required head rise and the second stage, the remainder.

(e) The present study utilizes the innovation of a supercavitating first stage coupled with a non-cavitating high solidity second stage.

Phase I of the present work concerned the theoretical and experimental investigations of an inducer having the first stage designed with supercavitating blades with constant pressure camber (2,3) and the second stage designed by the method of Reference 4. A stability analysis (5) based on the occurrence of rotating stall type instabilities in axial flow machines was used to calculate the limiting value of first stage head rise.

The design requirements chosen for the tandem inducer were as follows:

$$\text{Head coefficient, } \psi = \frac{gH}{u_t^2} = 0.25$$

$$\text{Flow coefficient, } \Phi_o = \frac{V_{f_o}}{U_t} = 0.10$$

$$\text{Suction specific speed, } N_{ss} = \frac{n\sqrt{Q}}{NPSH^{\frac{3}{4}}} = 30{,}000$$

The original design for an inducer to meet these requirements and maintain stable flow required that 15 percent of the total head be generated by stage 1 and 85 percent by stage 2.

A test program conducted in the HYDRONAUTICS, Incorporated pump loop (1) indicated that for optimum performance, both stages required empirical modification to solidity and pitch angle (Inducers No. 2 and 3). Tests conducted on each stage separately indicated that the best performance among the models tested was obtained from a first stage with 3 blades (c/d = 0.810) at the design pitch of 63.5° and a second stage with 6 blades c/d = 2.41) with a blade pitch of 55.8°, ten degrees less than the original design pitch. Section geometry was unchanged during these tests.

The best first and second stages were then tested in tandem with a -1.5 and -6 inch overlap. A complete summary of performance parameters for the tandem inducer operated at both overlaps is presented in Table 1. The tandem model produced more than the design head coefficient (0.29/0.25) at slightly less than the design flow coefficient (.083/.100) and less than the design suction specific speed (22,000/30,000). First stage cavity lengths were approximately as required by the original design (1.50-1.75/1.50).

The experimental performance, while not quite reaching the design objectives did indicate that the tandem inducer using a supercavitating first stage has definite potential as a high

TABLE 1

Summary of Tandem Inducer Performance (After (1))

Operating Parameter	Original Design Value	Experimental Value at -1.5 inch overlap	Experimental Value at -6 inch overlap
N_{ss}, entrance	30,000	22,000	22,000
Φ_o, average	0.100	0.083	0.083
ψ, total	0.250	0.283	0.296
ψ_{2nd}/ψ_{1st}	0.85	0.85	0.85
η_T, total	65% (1st stage only)	66%	62%
Stage 1 Pitch	63.5°	63.5°	63.5°
Stage 1, No. of blades	2	3	3
Stage 1, Char.solidity	0.540	0.810	0.810
Stage 1, ℓ/c	1.50	1.50	1.75
Stage 2, N_{ss}	13,250	10,600	10,600
Stage 2, Pitch	65.8°	55.8°	55.8°
Stage 2, No. of blades	6	6	6
Stage 2, Char.solidity	2.43	2.43	2.43

suction specific speed design concept. Low frequency instabilities or oscillations were noted at breakdown but appeared to stem from unstable cavity lengths rather than from Yeh (5) type instabilities which the original design was intended to avoid.

It became apparent, however, from the Phase I test program that the design goal of N_{ss} = 30,000 was unlikely to be reached using cascades of constant pressure cambered foils. One characteristic of such cascades is that as solidity is increased, the camber of the foil is reduced and finally approaches a flat plat. This is detrimental to the stability of the flow since flat plate profiles create a higher drag for the same lift than cambered profiles. The flat plate must rely entirely on angle of attack for lift generation.

Phase II of the project has aimed at further improving the capability for tandem inducer design through a theoretical study of higher term cambered supercavitating cascades. The types of foils considered in this study were the circular arc and two, three, and five term cambered sections (6). A separate report (7) has been issued describing the theory and results of this study. The theory for partially cavitating cascades of foils has also been studied and reported (8). As an extension and refinement of the second stage design procedure (4), a theoretical study of a radial line vortex in annular space (9) has been completed for various hub/diameter ratios and smaller axial and tangential spacings (10). Improved methods for calculating interference streamlines and coefficients have been developed. And finally, a tentative new first and second stage inducer design has been conducted.

Summary results of each of these tasks is reported in the remainder of this report. As noted separate reports have previously covered much of the work (7,8,10).

2.0 HIGHER TERM CAMBERED SUPERCAVITATING CASCADES

2.1 General Formulation

A theoretical study of supercavitating cascades utilizing foils of higher term camber was conducted. A computer program (actually an interdependent set of programs) to compute cascade characteristics was written, compiled and first verified by comparison with isolated foils and with cascades of flat plate foils in the existing literature.

The difficulty in this case can be appreciated by considering the much simpler problem of incompressible flow past a single supercavitating hydrofoil. The only exact analytical method known, based on certain artificial models of cavity termination, is the hodograph technique, which is rather complex. To solve such complex problems, one usually introduces suitable approximations. The most convenient of them is the linearized, closed-cavity theory of Tulin (12). Realizing the complication involved, a similar approximation is made in the present analysis. The problem of finding the cascade flow characteristics is then reduced to one of quadratures.

The method is inherently limited in its applications because it is based on the assumption of small thickness of the blades being treated and relatively small disturbances being generated. However, in practice, the inducer pump blades are thin and consequently the linearized results may be useful for design applications.

Consider the flow schematically illustrated in Figure 1. The cascade consists of an infinite array of identically cambered blades having a stagger angle β and an angle of attack α_1. The mean chord length of each blade is c and the spacing of the blades in the direction of the stagger angle is d. The flow is turned by the cascade from its original horizontal direction and velocity U_1 at upstream infinity to the direction α_2 and velocity U_2 at a location far downstream.

The types of foils under consideration are those which are outlined by Johnson (6). The shapes which he derives are those resulting from the optimization of a finite number of terms of the vorticity distribution in the airfoil plane such that maximum lift-drag ratio results for each hydrofoil shape. Strictly speaking, the foils thus generated can only be called two, three, or five term cambered foils in the isolated case, since the effects of cascade may modify the optimum shapes slightly. For continuity with the isolated foil case and for ease of calculation, the physical shapes presented by Johnson (6) have been used in the present program. This is further justifiable from a physical standpoint since it permits the computation of the performance of the same physical shape under a variety of conditions. This is in contrast to the constant pressure camber case where each change of cascade geometry or flow conditions results in a different foil shape. For the constant pressure camber case, therefore, off-design performance cannot be directly calculated.

In the analysis it is assumed that the blade and cavity, with length $\ell > c$, are equivalent to a slender body which causes only small distrubances in an otherwise uniform stream. As a first approximation the boundary conditions may be applied on the x-axis instead of on the slender body. The cavities are assumed to be detached from the sharp leading and trailing edges of each blade. The linearized boundary conditions on the blade surface, cavity boundary, and upstream infinity, and the closure conditions are given in Reference 7.

The linearized problem may be stated as follows: Given a cascade defined by β, ℓ/d, c/d, α_1 and y_f it is required to find the harmonic function $w(x,y) = u/U_c - i\, v/U_c$ on an infinitely connected domain which satisfies the mixed boundary conditions on the body, the conditions at upstream infinity and the closure condition.

The problem as formulated may be greatly simplified, (since the flow is periodic) with the aid of the conformal transformation

$$z = x + iy = \frac{d}{2\pi}\left[e^{-i\beta}\ \ell n\,\frac{1 - \zeta/\zeta_1}{1 - \zeta/\zeta_2} + e^{i\beta}\ \ell n\,\frac{1 - \zeta/\bar{\zeta}_1}{1 - \zeta/\bar{\zeta}_2}\right] \qquad [1]$$

which maps the multiple-connected region in the z-plane onto the $\zeta = (\xi + i\eta)$ plane as shown in Figures 2 and 3. The function has branch points at $\zeta_1 = r_1\ e^{i(\pi/2-\phi)}$ and $\zeta_2 = r_2\ e^{i(\pi/2+\phi)}$ corresponding respectively to up- and down-stream infinity in the physical z-plane. The line between ζ_1 and ζ_2 is a branch cut of the mapping function. By crossing the cut, the value of the logarithmic function in Equation [1] changes by $2\pi i$ or $-2\pi i$. Each Riemann sheet in the ζ-plane corresponds to the flow region over a different blade-cavity body in the cascade. The leading edge of the blade-cavity body is mapped to the origin of the ζ-plane and the trailing edge to a point at infinity. The juncture of the lower blade surface and cavity maps to $\zeta = -\mathrm{CAPC}$.

The linearized cascade problem is now reduced to that of finding a harmonic function $w(\zeta)$ in the ζ-plane which satisfies the boundary conditions. This boundary-value problem resembles closely that of the flow past an isolated supercavitating hydrofoil and is a special case of the Riemann-Hilbert problem for a half-plane (13).

To obtain the solution, it is expedient, to introduce the cascade parameters, given originally by Cohen and Sutherland (14), which characterize the geometry of the cascade:

$$\gamma_o = \ell n \, (b/a) \tag{2a}$$

$$Q = \sqrt{(\cosh \gamma_o)^2 - \sin^2\beta} \tag{2b}$$

$$\phi = \tan^{-1} \left(\frac{\sin \beta}{Q} \right) \tag{2c}$$

$$\ell/d = \frac{2}{\pi} \cos\beta \, \ln\left[\frac{(Q+\cos\beta)}{\sinh\gamma_o}\right] + \Phi \sin\beta \qquad [2d]$$

$$\rho_1 = \frac{(Q+\cos\beta)\cosh\gamma_o \sqrt{\cos\beta}}{2Q^{1.5}\sqrt{2\pi}} \qquad [2e]$$

$$\rho_2 = \frac{\sinh^2\gamma_o \cosh\gamma_o \sqrt{\cos\beta}}{2Q^{1.5}(Q+\cos\beta)\sqrt{2\pi}} \qquad [2f]$$

$$\psi_1 = \tan^{-1}\left[\frac{-(CAPC)\rho_1 \cos\Phi}{(1+(CAPC)\rho_1 \sin\Phi)}\right] \qquad [2g]$$

$$\psi_2 = \tan^{-1}\left[\frac{-(CAPC)\rho_2 \cos\Phi}{1-(CAPC)\rho_2 \sin\Phi}\right] \qquad [2h]$$

$$C/d = \cos\beta \, \ln\left[\frac{1+2(CAPC)\rho_1 \sin\Phi + (CAPC)^2\rho_1^2}{1-2(CAPC)\rho_2 \sin\Phi + (CAPC)^2\rho_2^2}\right]$$

$$+ 2\sin\beta\,(\psi_1 - \psi_2) \qquad [2i]$$

Equation [2d] gives the length of the slender (blade-cavity) body as functions of given parameters β and b/a. Equation [2i] determines the value of chord length, CAPC, in the transformed ζ-plane for given values of β, b/a and solidity c/d.

2.2 Solution of the Boundary-Value Problem

The general solution of the reduced boundary-value problem stated in the previous section, may be shown to be of the form

$$w(\zeta) = -\frac{1}{\pi} H(\zeta) \int_{-\infty}^{\infty} \frac{iw(t)}{H(t)} \frac{dt}{t-\zeta} + H(\zeta)\ P(\zeta) \qquad [3]$$

where

$H(\zeta)$ is the fundamental solution which depends on the flow behavior at the edge points $\zeta = 0$ and $\zeta = -CAPC$,

$P(\zeta)$ is a rational function which depends on the flow behavior at the edge points and $\pm\infty$.

The first term of Equation [3] is the particular solution which satisfies the mixed boundary conditions on the real ξ-axis while the second term is the general solution of the corresponding homogeneous problem.

In accordance with the linearized formulation, the functions $H(\zeta)$ and $P(\zeta)$ take the forms

$$\begin{aligned} H(\zeta) &= i\sqrt{\frac{\zeta+CAPC}{\zeta}} \\ P(\zeta) &= A\zeta + B \end{aligned} \qquad [4]$$

where A and B are real constants. The general solution of the boundary-value problem, in this case, becomes

$$w(\zeta) = i\sqrt{\frac{\zeta+CAPC}{\zeta}}\left[-\frac{1}{\pi}\int_{-CAPC}^{o}\frac{\left(-\alpha_1 + \frac{dy_f}{dx}(t)\right)}{t-\zeta}\sqrt{\frac{-t}{t+CAPC}}\,dt + A\zeta + B\right] \qquad [5]$$

which must also satisfy the uniform flow conditions at upstream infinity and the closure conditions.

The flow field $w(\zeta)$ is thus completely determined for a prescribed oncoming flow direction, body shape, cavity length and cascade geometry.

In the case of flat plate cascade, i.e., $dy_f/dx = 0$, the complex velocity field is of the form

$$w(\zeta) = i\sqrt{\frac{\zeta+CAPC}{\zeta}}\left[\alpha\left(1 - \sqrt{\frac{\zeta}{\zeta+CAPC}}\right) + A\zeta + B\right] \qquad [6]$$

which may be shown to yield a solution identical to that given by Cohen and Sutherland (14).

Expressions for the lift, drag, cavity shapes and exit flow characteristics are given in Reference 7.

2.3 Numerical Results and Discussion

The method of calculating the flow field around a supercavitating cascade, as presented in the previous sections is in many respects similar to that given for isolated supercavitating hydrofoils. The calculations generally involve only numerical integrations and algebraic operations.

The slopes of the foil shapes used in the present case are defined as follows:

flat plate

$$\frac{dy}{dx} = 0 \qquad [7a]$$

two term camber

$$\frac{dy}{dx} = \frac{4}{5\pi} k_2 \left(1 + 4\left(\frac{x}{c}\right)^{.5} - 8\left(\frac{x}{c}\right)\right) \qquad [7b]$$

three term camber

$$\frac{dy}{dx} = \frac{2}{15\pi} k_3 \left(5 - 30\left(\frac{x}{c}\right)^{.5} + 160\left(\frac{x}{c}\right) - 160\left(\frac{x}{c}\right)^{1.5}\right) \qquad [7c]$$

five term camber

$$\frac{dy}{dx} = \frac{4}{5\pi} k_5 \left(1 - 16\left(\frac{x}{c}\right)^{.5} + 120\left(\frac{x}{c}\right) - 368\left(\frac{x}{c}\right)^{1.5} + 512\left(\frac{x}{c}\right)^{2} - 256\left(\frac{x}{c}\right)^{2.5}\right) \qquad [7d]$$

circular arc

$$\frac{dy}{dx} = \frac{16}{9\pi} k_c \left(1 - 2\left(\frac{x}{c}\right)\right) \qquad [7e]$$

The angle of attack term is handled separately and is thus not included in the dy/dx term, with the exception of the circular arc case. For the circular arc, the convention of Johnson (6) is used where the chord of the foil is rotated through 1/8 of the central angle to insure a positive pressure over the entire wetted face of the foil. The camber indices k_2, k_3, k_5, k_c are the respective lift coefficients of the isolated, infinite depth, zero sigma, zero angle of attack foils. The higher the camber index the greater the camber of the respective foils.

In addition to the first order linearized results, the program also calculates second order approximations using equations presented by Hsu (11) and verified for the isolated circular arc case. While there is no available method for verifying the second order approximation for cascades or for cambers other than the circular arc, it was included since little additional programming was required to do so. When one undertakes a calculation involving finite cavities, there are essentially 6 parameters which must be fixed to specify a unique cascade. These are:

1. the stagger angle of the cascade, β
2. the solidity of the cascade, C/d
3. the camber type (shape)of the foils, FTYPE
4. the amount of camber (camber coefficient,) k
5. the angle of attack of the foils, α_o
6. the cavity length to chord ratio, ℓ/c

Four of these parameters: β, FTYPE, k, and α_o may be chosen in a straight forward manner. The remaining two: C/d and ℓ/c, are dependent variables determined by the stagger angle, β, the transformed chord length, CAPC, and another cascade parameter, b/a. The parameter b/a also is used in fully wetted cascades and is discussed by Garrick in Reference 15. In fully wetted flow, the value of b/a uniquely relates a given β and solidity. For the supercavitating case the relationship is identical except that instead of solidity, C/d, the value of ℓ/d (cavity length to foil spacing) is determined. This essentially amounts to considering the entire length of foil and cavity to correspond to the foil length in fully wetted flow.

The solution of Equation [2d] is shown in Figure 4 for β over the range 45° to 90° and b/a = 1.00001 to 20.0. Note that the relationships shown in Figure 10 are independent of solidity, foil type, camber, and transformed chord. The curves representing small values of b/a become very "compressed" at high values of β. For this reason, as the stagger angle of a cascade becomes higher and higher, the possible range of ℓ/d values which can be obtained is restricted. Thus the possible range of ℓ/c values for a given C/d is also restricted.

The solution to Equation [2i] is slightly more involved in that the transformed chord, CAPC, is introduced. In this case, a single graph cannot demonstrate the relationship among C/d, β, b/a and CAPC. Each value of β requires a separate graph. Figure 5, 6 and 7 are typical of the relationships and are calculated for

$\beta = 45^\circ$, 65° and 85°. As the stagger angle increases, the relation between β and CAPC for a given b/a becomes steeper thus requiring larger values of CAPC to be chosen to yield a given C/d. For example, say that a solidity of 0.40 is desired at $\beta = 45$, 65, and 85° with b/a = 1.02. The respective transformed chords required would be 29., 120., and 200. At other b/a's the change may be even more dramatic. For example, with C/d = .40 and b/a = 1.001, the required CAPC's are 29., 120., and 46,500. From Figure 10 we see that higher b/a values yield lower ℓ/d values and thus lower ℓ/c values for a given C/d. The following table indicates the cavity length parameters which would result from the examples considered above.

TABLE 2

Effect of b/a on ℓ/c at Constant C/d = 0.40

β	b/a	CAPC	ℓ/d	ℓ/c
45°	1.02	29.	2.27	5.67
	1.001	29.	3.56	8.90
65°	1.02	120.	1.66	4.15
	1.001	120.	2.47	6.17
85°	1.02	200.	1.06	2.65
	1.001	46,500.	1.23	3.08

Note that rather significant changes in ℓ/c resulted at the lower stagger angles even though CAPC remained unchanged while little change occurred at $\beta = 85^o$ even though CAPC changed by more than two orders of magnitude. Thus we see that the range of cavity length to chord ratios which can be calculated is limited at high stagger angles.

A second characteristic of the relationships shown in Figures 15, 16 and 17 is that for each b/a a certain maximum CAPC is reached for which a positive C/d results. This effect occurs suddenly for a very small incremental change in CAPC. In order to illustrate the point more clearly, Figure 8 shows a computation for $\beta = 75^o$, b/a = 1.00001, 1.15, 1.50, and 3.00 in which small incremental changes in CAPC were used to calculate the corresponding solidities. The 1.00001 and 1.15 curves are well behaved over the entire range plotted. The 1.50 and 3.00 curves, however, are not and show similar behavior to one another. Each drops abruptly to a negative solidity (which has no physical meaning) at a critical value of transformed chord. For the b/a = 1.50 curve, the critical CAPC is between 15.1 and 15.2. For the b/a = 3.00 curve it is between 14.6 and 14.7. Thus to calculate cascade characteristics for $\beta = 75^o$ and b/a = 3.00, 1.50 one is limited to maximum solidities of 0.548 and 0.336 respectively.

The same phenomenon just described occurs for every b/a and stagger angle at some value of CAPC. The critical value of CAPC (and thus maximum obtainable C/d) increases when either

β or b/a becomes smaller. The phenomenon becomes restrictive if the maximum C/d falls in the region of interest, $0.50 < C/d < 1.50$.

With these limitations in mind we will now discuss further cascade calculations.

2.3.1 Infinite Cavity Flat Plate and Circular Arc Results - Acosta (16) has calculated the theoretical performance of flat plate and circular arc cascades with infinite cavities using a linearized theory. Verification of his method is obtained by comparing the results for a flat plate cascade with the exact solution of Betz and Petersohn (17) which they obtained with the aid of the Hodograph method. The definitions of stagger angle and angle of attack used in (16) are slightly different from the present case. In addition, Reference 16 uses the normal force coefficient C_N, rather than the lift coefficient C_L in the present work. The results presented in Figures 9 thru 14 are in terms of the system of Reference 16.

Figures 9, 10 and 11 compare the results of the present computations for flat plate cascades with long cavities to the results of Acosta (16) and Betz and Petersohn (17) over the range of solidities 0.50 to 1.50, stagger angles 0° to 75°, and angles of attack 0° to 7°. Agreement among the methods is excellent. The present calculations yield solutions closer to the exact solution than did the calculations of Acosta. This is especially true at the higher stagger angles likely to be of interest for inducer designs.

Included in Figures 12, 13 and 14 are the first order results for circular arc cascades from the present program and the approximate second order results as calculated by the method of Hsu (11) as previously mentioned. Agreement between the present method and the results of Acosta is fairly good. The present calculations tend to estimate lower normal force coefficients especially at high solidities and high stagger angles. As expected the approximate second order results yield lower values of C_N. The difference between first and second order results becomes smaller, however, as solidity increases and also as stagger angles increase. The trends noted for the circular arc cascades are the same as those for flat plate cascades.

2.3.2 Comparison to Constant-Pressure-Cambered Case - The computations of Yim (2) are different from the present case in two ways. First, the foil shape used by Yim was a constant pressure cambered geometry. This is different from any shape used in the present case but may be approximated by the present circular arc. Secondly, the results of Yim do not yield a particular cavitation number, lift coefficient and foil shape for each cascade geometry but rather the ratio cavitation of number and foil shape to lift coefficient. Thus σ/C_L and $y/_{cC_L}$ are the primary parameters for a given stagger, solidity and cavity length. Angle of attack α is given as α/C_L and is not an independent variable in the scheme of Yim (2).

It is therefore, rather difficult to compare these results directly to the present case; however, an attempt at such a comparison has been made. One case presented by Yim was a constant pressure cambered cascade with stagger angle $\beta = 75^{\circ}$ and solidity $C/d = 0.410$, ℓ/c = variable. This case was chosen for comparison. Figure 15 shows the variation of lift coefficient and cavitation number with cavity length for the circular arc cascade chosen for comparison. A camber coefficient of $k = .185$ (central angle of foils $= 12^{\circ}$) and angles of attack, $\alpha = 7.0^{\circ}$ and 4.5° were arbitrarily chosen hoping to approximate the shape and angle of attack of the constant pressure-cambered foils.

A rather unexpected behavior is illustrated in Figure 15. Note that the lift coefficient is essentially constant for cavity lengths above 5.0. Below this value, however, a sharp increase in lift coefficient occurs climbing to impossibly high values of 3.6 and 4.3 at $\ell/c = 2.50$. Beyond this point, the value of C_L drops sharply again. To understand this characteristic, we must look at the input in terms of b/a and CAPC used to obtain each cavity length. These values are presented in Table 3.

Note particularly that the values of CAPC do not change up to the point ($\ell/c = 4.50$) where the sharp up turn in lift coefficient occurred. In fact,when one looks at the $C/d - \beta - b/a -$ CAPC relation (similar to Figure 6) for this case it is apparent that the relations for $b/a = 1.00001$ to 1.0009 are identically the same line. However, the $\ell/d - \beta - b/a$ relations (see Figure 4) are not the same for these b/a values and thus some variation in ℓ/c results.

TABLE 3

Program Inputs to Cascades of Figure 15

ℓ/c	b/a	CAPC (Transformed Chord)
6.31	1.00001	980.0
5.66	1.00005	980.0
5.38	1.0001	980.0
4.73	1.0005	980.0
4.50	1.0009	980.0
4.04	1.003	930.0
3.85	1.005	880.0
3.73	1.007	810.0
3.60	1.009	780.0
3.31	1.019	500.0
3.18	1.027	350.0
2.48	1.14	36.0
1.94	1.40	13.5
1.63	1.70	11.8
1.55	1.80	11.9
1.473	1.95	12.1
1.47	2.00	12.0
1.38	2.10	12.8

The cavitation number in Figure 15 also remains quite constant above a certain value of ℓ/c. This value is slightly lower than the critical value for lift coefficient. Above this ℓ/c, σ increases sharply and continues to increase as ℓ/c is decreased. The assumptions made in linearization require that the value of σ be quite small compared with 1.0. For example, a value of $\sigma = 0.25$ has considerably exceeded the linearized assumptions. We see from Figure 15, however that by the time $\sigma = 0.25$ has been reached, the value of C_L is already reached its unreasonably high peak.

Figure 16 compares the ratio σ/C_L for the constant-pressure-camber (CPC) cascade to the ratio σ/C_L for the circular arc cascade as a function of cavity length. Note that the CPC result shows little variation in the ratio σ/C_L above $\ell/c = 3.0$. Below this value, a continuous increase in σ/C_L occurs as $\ell/c \rightarrow 1$. In contrast, the circular arc cases show a sharp dip followed by a steep increase. The values of α_o chosen for the circular arc foils effectively bracket the CPC performance at large ℓ/c.

Although the camber distributions of the two types of foils being compared are different, the angle of attack α_o and maximum camber y_c/cC_L will be used to compare the two geometries at $\ell/c > 5.0$. From Figure 16 an interpolated value of $\alpha_o = 5.9^o$ would result in good agreement as far as σ/C_L is concerned. Note that the definition of angle of attack for the circular arc case excludes a value of 1/8 the central angle of the foil (after Johnson (6)) to assure positive pressure on the fully wetted face of the foil. For the circular arc foil, the true geometric angle of attack and camber are:

$$\alpha_{TRUE} = \alpha_o + \gamma/8 = 7.4^\circ, \text{ Camber } /cC_L = .146$$

For the CPC foil angle of attack and camber are:

$$\alpha = 5.05^\circ \text{ and Camber}/cC_L = .106$$

This means that for a particular C_L and ratio of σ to C_L at a given cavity length, β, and C/d the CPC result indicates less physical camber and angle of attack required than for the circular arc case. In other words, the CPC case is shown to have a more effective or efficient camber distribution in cascade. Since the cascade characteristics were calculated by different methods it is not possible at this time to say whether the difference in the two results is an accurate reflection of their relative efficiencies or whether the technique of calculation and method of linearization have introduced part of the difference. We do know however from the experimental program (1) that the experimental value of the parameter (C_L/σ) (c/d) for stage 1 of inducer 1 was less than 1/3 of the predicted theoretical value. Even acknowledging real fluid and three-dimensional effects have contributed to this reduction, the results indicate that the CPC theory tends to overestimate the ratio C_L/σ.

A comparison of the actual physical shapes of the two foils being considered is shown in Figure 17. The vertical scale is distorted. The camber distributions are different but not different enough that one would expect the large difference in camber and angle of attack indicated for similar lift-cavitation number performance. We may tentatively conclude, therefore, that the present calculations indicate a more conservative relation between σ and C_L for similar geometries, i.e., that more camber and angle of attack is required for a similar camber distribution to yield a particular lift coefficient at a particular cavitation number than in the calculation of Yim (2).

In the previous comparison, the camber index of the circular arc foil used was arbitrarily chosen as 0.185, corresponding to a central foil angle of 12°. To study the effect of camber index on the relative performance of circular arc and CPC foils, a number of camber indices were used corresponding to a range of foil central angles from 4° to 32° in steps of 4°.

Figure 18 shows the relationship between σ/C_L and angle of attack for the various cambers under the cascade characteristics previously used. Using a constant $\sigma/C_L = 0.82$, values of α_o can be obtained from this curve for each value of camber index. Figure 19 shows a similar relation for camber/cC_L as a function of α_o at the same camber coefficients. Using the values of α_o from Figure 18 corresponding values of camber/cC_L can be obtained from Figure 19. In Figure 20, the values of camber/cC_L versus α/C_L for constant $\sigma/C_L = .082$ for the entire range of camber constants are plotted using circular symbols. Note that all the points fall in a cluster showing that regardless of the amount of camber, the ratio of camber to angle of attack is approximately constant for constant σ/C_L. This does not mean that C_L is constant for each of the cambers calculated. Figure 21 shows the large variation in actual C_L over the range calculated. Lines of constant σ/C_L are nearly linear on this plot.

In Figure 20, the Yim constant-pressure-camber case is indicated by a square symbol. Calculations for $\sigma/C_L = .082$ were also made for the other types of camber presently under consideration using a camber index of 0.185. These results are shown as the triangular symbols in Figure 20. The circular arc case is replotted and is shifted slightly from the circular cluster because $\gamma/8$ was excluded from α_o. Figure 20 indicates that the cascades become progressively more efficient as the foils assume higher term camber distributions. The three term camber case falls near the Yim CPC case and the five term case is considerably better. It is significant that the difference between the three and five term camber cases is large indicating that even higher term cambers might continue to produce significantly better results.

2.3.3 Comparison to Experimental Cascade Performance - The experimental data on supercavitating cascades is very limited. The extensive work of Numachi (for example, 18) is concerned with the cavitation performance of subcavitating airfoil sections and is aimed at the development of a section with the best cavitation performance in cascade with respect to late cavitation inception and high lift drag ratio, at low cavitation number.

A recent and extensive test program conducted by United Aircraft Research Laboratories (19) has similar goals using circular arc sections. Wade and Acosta (20) have reported a limited amount of data covering the entire range of cavitation from inception and partial cavitation to full cavitation and supercavitation. The foil sections were of a plano-convex nature with the "pressure side" a flat surface, and the "suction side" a circular arc. In the cavitating range many experimental difficulties were encountered. At angles of attack reported as 6° or less, the cavities were found to develop on the flat side of the foils resulting in a cascade with negative effective camber when supercavitating. Above 6° angle of attack, the cavities developed on the circular arc side of the foils and thus an effective flat plate cascade was encountered in the supercavitating range of operation. In a discussion of the results of Wade and Acosta, Pearsall (21), referencing theoretical results according to Duller (22), shows fairly good agreement between theory and experimental at $C/d = 0.625$, but poor agreement at $C/d = 1.25$. Pearsall, however, incorrectly blames the limitation of the potential flow approach for the discrepancy at the higher solidity. The high solidity data presented by Acosta is all in the range of 0° to 6° angle of attack and thus has the cavity on the flat (nominally pressure) side of the foil. Obviously these foils must have experienced a net negative angle of attack over this range and therefore increases in α from 0° to 6° were in reality decreases in α from some negative value toward true 0° angle of attack. This conclusion is verified by the Wade and

Acosta data showing that at C/d = 1.25 to maintain a constant cavity length (say $\ell/c = 2.0$), the cavitation number had to be decreased as the nominal angle of attack was increased. For this reason comparison of the present calculations to Wade and Acosta's data has been limited to a case where the cavity was on the correct (convex) side of the foils, the case of $\beta = 45^\circ$, C/d = 0.625 and $\alpha = 8^\circ, 9^\circ$.

Figures 22 and 23 compare lift coefficient as a function of cavitation number for the present theory to the experimental results for 8° and 9° respectively. Note that a large portion of the experimental range is partially cavitating. Also included on each figure is a line showing the approximate isolated linearized theory as a reference. Agreement between the theory and experiment is less than perfect, but encouraging considering the limited number and difficulty of the experimental measurements and the theoretical approximations. Figure 24 compares the predicted to measured cavity lengths in each case. Note that the theory correctly predicts the observed result that below a certain value of cavitation number, the cavity length is not well defined but may quickly change from a rather short to essentially infinite length with infinitesimal changes in σ.

Similar results may be obtained for the other cambers under study. Figures 25 and 26 show calculations for a circular arc cascade with the same solidity and stagger angle and a camber index of 0.247.

Pearsall (23) presents some limited data for flat plate and circular arc cascades reduced from experimental results of tests on actual axial flow pump impellers. The data reported by Pearsall are for the following conditions:

TABLE 4

Test Conditions for Data of Pearsall (23)

Circular Arc Cascade	Flat Plate Cascade
$\beta = 69.53^\circ$ $C/d = .420$ $k = .247$ $\alpha = 7^\circ - 11^\circ$ $\sigma = .02 - .07$ ℓ/c not reported	$\beta = 68.03^\circ$ $C/d = .365$ $\alpha = 6.7^\circ - 9.3^\circ$ $\sigma = .02 - .10$ ℓ/c not reported

Figures 27 and 28 compare some calculations using the present theory to the results reported by Pearsall. It can be concluded that agreement between the data and theory is closer for the flat plate case than the circular arc. Much greater sensitivity to cavitation number is indicated from the theory than is shown in the experiments with the agreement between the two better at long cavity lengths (as calculated, since ℓ/c is not reported in the experiments) than at shorter cavity lengths. The calculation in Figure 28 indicates the sharp up-turn in C_L with σ as shown in Figures 22 and 23.

It is noteworthy that the Pearsall data shows a rather constant value of C_L over a wide range of σ for a given cascade condition. The theory on the other hand predicts a very narrow range of σ over which a particular cascade may operate. Little else can be conjectured about this comparison since the experimental conditions are so loosely defined, and since the experiments must include the three-dimensional effects not accounted for by a cascade calculation. These effects would be minimized in experiments with actual cascades such as those of Wade and Acosta. It should be apparent from the above discussion that good, reliable supercavitating cascade data is virtually nonexistant.

2.3.4 Influence of Foil Type and Camber Index on Performance - The complex nature of the computational procedure has been previously outlined. In order to compare the influence of foil type and camber index on typical cascade geometries, a series of calculations were undertaken with $b/a = 1.00001$. This value is sufficient to place the resultant ℓ/c values in the "long-cavity" range in which lift and cavitation number vary little with ℓ/c. This is the range where curves typified by Figures 16, 24, 25 and 26 are flat.

Figure 29 illustrates the effect of stagger angle on the lift coefficient of a series of cascades with all five camber types and $C/d = 0.75$, $\alpha = 10^{\circ}$, and $k = 0.15$. (The flat plate case of course has $k = 0$). Over the entire range of stagger angles calculated, the five term camber foils show higher lift coefficients than any of the other types, but as stagger angle increases, the five term camber performance degrades at a rate slightly higher than the others and its relative advantage decreases. For example at $\beta = 45^{\circ}$, the 5 term case has 169 percent of the circular arc lift while at 75° it has 150 percent. Figure 30 shows the corresponding cavitation number range for the foils of Figure 29. As the stagger angle becomes higher and higher, the range of σ becomes narrower. This is probably part of the reason for the narrowing of the C_L range in Figure 29.

Figure 31 shows the influence of solidity on lift coefficient for cascades using all five camber types, $\beta = 65^{\circ}$, $\alpha = 10^{\circ}$ and $k = 0.15$. Each type degrades sharply with increasing solidity. Again the five term camber case is best over the entire range but it degrades more rapidly with increasing solidity than the other types. At $C/d = 0.50$ the five term case has 175 percent of the lift of the circular arc case while at $C/d = 1.0$ it has decreased to 155 percent. Figure 32 shows the corresponding values of cavitation number for the cascades of Figure 31. Note the narrow range for the cascades considered.

Figure 33 shows the effect of camber type and two camber indices, 0.25 and 0.15, on the lift coefficient and cavitation number for cascades of $\beta = 65^{\circ}$, $C/d = 0.75$ and $\alpha = 10^{\circ}$.

3.0 PARTIALLY CAVITATING CAMBERED CASCADES

The flow past a supercavitating cascade of cambered blades has been discussed in some detail in the previous section. The only available theoretical study on flow past a cascade of partially cavitating blades, (i.e., the cavity length is shorter than the chord length,) is due to Wade (24) who dealt with the problem of thin flat plate hydrofoils.

In the present case the problem of the flow of incompressible, inviscid fluid past a partially cavitating cascade of cambered blades is formulated. The analysis is based on the assumptions that the flow is two-dimensional and that disturbances are small. With the aid of conformal transformation, it is possible to calculate such complex flow problems.

3.1 General Formulation

Consider the flow schematically illustrated in Figure 34. The cascade consists of an infinite array of identical thin cambered blades having a stagger angle β and a small angle of attack α_1. The mean chord length of each blade is c and the spacing of the blade in the direction of stagger angle is d.

The flow approaches the cascade with velocity U_1 and is turned by the aggregate effect of the cascade from its original horizontal direction to the direction α_2 and velocity U_2 at far downstream. The cavities of length $\ell < c$ are assumed to be thin and spring from the leading edge and terminate on the upper surface of each blade. As a first approximation the boundary conditions, may be applied along the x-axis. Boundary conditions on the wetted portion of the blade, on the cavity, at upstream infinity, and the cavity closure condition, are given in Reference (8).

In order to find the perturbed velocity field

$$w = \frac{u}{U_c} - i\,\frac{v}{U_c} \qquad [8]$$

it is expedient, first, to introduce a transformation function

$$z = x + iy = \frac{d}{2\pi}\left[e^{-i\beta}\,\ell n\,\frac{1-\frac{\zeta}{\zeta_1}}{1-\frac{\zeta}{\zeta_2}} + e^{i\beta}\,\ell n\,\frac{1-\frac{\zeta}{\zeta_1}}{1-\frac{\zeta}{\zeta_2}}\right] \qquad [9]$$

similar to the one used for the supercavitating case (7). This maps the multiple-connected region in the z-plane onto the ζ-plane. The function again has branch points at $\zeta_1 = e^{i(\pi/2-\varphi)}$ and $\zeta_2 = a^{i(\pi/2+\varphi)}$ corresponding to up and down-stream infinity respectively in the physical z-plane. By crossing the branch cut $\overline{\zeta_1\zeta_2}$, that is proceeding from one blade to the next one, the value of log $(1-\zeta/\zeta_1)$ or log $(1-\zeta/\zeta_2)$ changes by $2\pi i$ or $-2\pi i$. The leading and trailing edges of the blade are mapped to the origin and to infinity. The problem is now reduced to that of finding a harmonic function $w(\zeta)$ in the ζ-plane which satisfies the boundary conditions and closure condition.

The cascade parameters are determined by the following equations

$$\tan\varphi = \frac{a-1}{a+1}\tan\beta \qquad [10]$$

$$\frac{c}{d} = \frac{1}{\pi}\left(\cos\beta \,\ln a + 2\varphi\sin\beta\right) \qquad [11]$$

$$\frac{\ell}{d} = \frac{1}{\pi}\left\{\frac{\cos\beta}{2}\ln\frac{1-2s\sin\varphi + s^2}{1+2(s/a)\sin\varphi + (s/a)^2} + \sin\beta\left[\tan^{-1}\frac{s\cos\varphi}{1-s\sin\varphi} - \tan^{-1}\frac{(s/a)\cos\varphi}{1+(s/a)\sin\varphi}\right]\right\} \qquad [12]$$

The value of the cavity length s in the transformed plane, and the scaling parameters, a and φ can be computed once the geometrical characteristics of cascade c/d, ℓ/d and β are given.

3.2 Solution of the Boundary Value Problem

The boundary value problem in the transformed ζ-plane resembles closely that of flows past isolated partially cavitated hydrofoils and is a special case of the Rieman-Hilbert problem for a half plane (13). As in the case of the supercavitating cascade, the general solution may be shown to be of the form

$$w(\zeta) = -\frac{1}{\pi} H(\zeta) \int_{-\infty}^{\infty} \frac{iw(t)}{H(t)} \frac{dt}{t-\zeta} + P(\zeta)\, H(\zeta) \qquad [13]$$

where

$H(\zeta)$ is the fundamental solution which depends on flow behavior at edge points $\zeta = 0$ and $\zeta = s$,

$P(\zeta)$ is a rational function which may have isolated singularities only at edge points $\zeta = 0$ and $\zeta = s$ and at infinities.

The first term of Equation [13] is the particular solution which satisfies the mixed boundary conditions on the real ξ-axis while the second term is the general solution of the corresponding homogeneous problem.

In accordance with the linearized formulation (25) it is required that $w(\zeta)$ satisfy the boundary conditions given in Reference (8) which lead the functions $H(\zeta)$ and $P(\zeta)$ to take the form:

$$\left.\begin{aligned} H(\zeta) &= \sqrt{\zeta(\zeta-s)} \\ P(\zeta) &= \frac{A\zeta+B}{\zeta(\zeta-s)} \end{aligned}\right\} \qquad [14]$$

With A and B real constants. The final form of the general solution is given by

$$w(\zeta) = \frac{\sqrt{\zeta(\zeta-s)}}{\pi}\left[\int_{-\infty}^{0} \frac{-\alpha_1 + \frac{dy_f}{dx}(t)}{\sqrt{t(t-s)}}\,\frac{dt}{t-\zeta}\right.$$

$$\left. + \int_{s}^{\infty} \frac{-\alpha_1 + \frac{dy_f}{dx}(t)}{\sqrt{t(t-s)}}\,\frac{dt}{t-\zeta}\right] + \frac{A\zeta+B}{\sqrt{\zeta(\zeta-s)}} \qquad [15]$$

which should, in addition, satisfy

at $\zeta = \zeta_1$ (upstream infinity)

$$R\ell(w) = \frac{1}{\sqrt{1+\sigma}} - 1 \qquad [16]$$

$$Im(w) = 0 \qquad [17]$$

and the closure condition,

$$- Im \oint_{\text{body}} w(\zeta)\,\frac{dz}{d\zeta}\,d\zeta = Im \oint_{\substack{\text{about }\zeta_1\\ \text{and }\zeta_2}} w(\zeta)\,\frac{dz}{d\zeta}\,d\zeta$$

$$= -d\;R\ell\left[e^{-i\beta}\left(1 - \frac{1}{\sqrt{1+\sigma}} + w(\zeta_2)\right)\right] = 0 \qquad [18]$$

Equations [16], [17] and [18] determine, uniquely, the constants A, B and σ.

For flat-plate blades, i.e. $dy_f/dx = 0$, the complex velocity is of the form

$$W(\zeta) = \frac{A\zeta + B}{\sqrt{\zeta(\zeta - s)}} - i\alpha_1 \qquad [19]$$

which, together with boundary and closure conditions Equations [16], [17] and [18] may be shown to yield a solution identical to that given by Wade (24).

Expressions for the lift and drag, experienced by the blade as a result of fluid flow are given in Reference (8), as are expressions for cavity shape and exit flow conditions.

3.3. Discussion and Experimental Data

The formulation presented gives the linearized solution for the flow past a straight cascade of partially cavitating cambered blades. From the analysis, it is possible to determine the lift and drag coefficients, cavitation number, cavity shape and downstream flow conditions for any given specific cascade geometry, blade shape, cavity length and initial inflow conditions.

As indicated by the experiments of Wade and Acosta (20) the flow is unstable when the cavity length-chord ratio is close to unity; the analysis is, therefore, invalid in this flow regime. The present analysis is also limited to cases in which the disturbance, caused by the presence of the blades, is small - an inherent restriction in the linear approximation. However in practice, the blades are, generally, thin. Consequently the linearized results are valuable as a guide in the design of inducers and other turbomachinery applications.

The amount of experimental data available concerning the performance of partially cavitating cascades is also limited but in much greater supply than the fully cavitating cascades previously discussed. The data of Wave and Acosta (20) is largely in the partially cavitating range as is some of the work of Numachi (18) and United Aircraft (19). Furthermore, much of the work on helical inducers in the literature may be considered as three-dimensional data for partially cavitating flat plate cascades. (26, 27, 28, 29, etc.) Since in most cases, however, only overall performance is considered, it is difficult to draw conclusions regarding two-dimensional cascades from this data.

4.0 RADIAL VORTEX FILAMENT IN A CYLINDRICAL ANNULUS AND SECOND STAGE INTERFERENCE STREAMLINE CALCULATIONS

4.1 Introduction

Simplification of the problem of finding the three-dimensional potential flow field for a finite number of blades of constant circulation in an axial turbomachine to the determination of the three-dimensional field due to a single radial vortex filament of uniform strength in a cylindrical annulus has been made by Tyson (9). For more than one blade, the solution may be found by superposition of the single filament fields.

The Laplace equation in cylindrical coordinates

$$\frac{1}{r}\frac{\partial}{\partial r}\; r\,\frac{\partial \varphi}{\partial r} + \frac{1}{r^2}\frac{\partial^2 \varphi}{\partial \theta^2} + \frac{\partial^2 \varphi}{\partial x^2} = 0 \qquad [20]$$

governs the behavior of the velocity potential φ in the annular region with

r = radial coordinate from the centerline,

θ = angular position from a reference line,

x = axial position along the annulus from a reference plane normal to the centerline,

a = hub radius, and

b = casing radius.

The boundary conditions state that the inner and outer cylindrical boundaries of the annulus, r = a and b, are stream surfaces, and that the only singularity in the field is a single radial vortex filament located at θ = 0, x = 0. The total circulation of the filament, Γ, is assumed to be evenly divided upstream and downstream of the filament.

Employing separation of variables and a periodic series representation, the solution for the required velocity potential may be written:

$$\Phi = \pm \frac{1}{4\pi}\left(\theta + 4\sum_{m=1}^{\infty} \frac{\sin m\theta}{m} \sum_{n=1}^{\infty} \frac{\beta_{nm}}{\gamma_{nm}} Z_m\left(\frac{\mu_{nm}\,\eta}{\eta_H}\right) e^{\mp \frac{\mu_{nm}\,\xi}{\eta_H}}\right) \quad [21]$$

where the sign difference refers to the regions upstream and downstream of the filament location, and

Φ = dimensionless velocity potential Φ/Γ,

β_{nm} = constant,

γ_{nm} = constant,

J_m = Bessel function of the first kind,

Y_m = Bessel function of the second kind,

B_{nm} = constant,

$Z_m = J_m + B_{nm}Y_m$,

μ_{nm} = dimensionless Eigenvalue $\lambda_{nm}a$,

η_H = hub ratio, a/b,

η = dimensionless radial coordinate, r/b, and

ξ = dimensionless axial coordinate, x/b.

To superpose the velocity fields due to a number of filaments (see Reference 9)

$$V = v\left(\theta + \frac{2\pi}{N}\right) + v\left(\theta + 2\,\frac{2\pi}{N}\right) + \ldots + v\left(\theta + N\,\frac{2\pi}{N}\right) \qquad [22]$$

where

N = the number of filaments,

V = the resultant tangential, radial, or axial velocity, and

v = the tangential, radial, or axial velocity component due to a single filament.

4.2 Numerical Calculations

The solution presented in Equation [21] has been programmed by HYDRONAUTICS, Incorporated using FORTRAN IV on an IBM 1130 Computer. There are two distinct calculations, required and separate programs were written for each of these. The first calculates the Eigenvalues μ_{nm}, the coefficient ratio β_{nm}/γ_{nm}, and the coefficient B_{nm}. The second uses these values to compute Φ and ultimately the dimensionless axial, tangential and radial velocity components:

$$C_\xi = \frac{\partial\Phi}{\partial\xi} \qquad [23a]$$

$$C_\eta = \frac{\partial\Phi}{\partial\eta}, \text{ and} \qquad [23b]$$

$$C_\theta = \frac{\partial\Phi}{\partial\theta} \qquad [23c]$$

The computer calculation time required to determine each Eigenvalue, μ_{nm}, with coefficients β_{nm}/γ_{nm} and B_{nm}, is approximately four minutes. The time required to compute each set of three velocities is dependent on the maximum values of n and m selected. If $n_{max} = 6$ and $m_{max} = 40$ approximately six minutes is required per set.

4.3 Eigenvalue Calculations

The dimensionless Eigenvalues, μ_{nm} required for the evaluation of Equation [2] were calculated numerically and compared to the values given for a single hub ratio η_H of 0.60 in Reference 9, which cover the range of n = 1,2 and m = 1 through 10, 15 and 20. The values between m = 10, 15 and m = 15, 20 were found in (9) by interpolation, and values from m = 20 to m = 26 were found by extrapolation. The present calculations, based on a trial and error solution of the eigenvalue equation, show agreement with these eigenvalues to the limit of the four significant digits presented. Eigenvalues calculated for n = 1 to 6, m = 1 to 40 and η_H of .70 and .80 as well as .60 are presented in Reference (10).

Reference 9 states that an approximate series representation (Reference 30) for μ_{nm} is available, but is not accurate for small values of n and m. This series representation was programmed and compared to the present numerical solution. The results are presented in Reference (10) where the conclusion drawn was that the series is a more suitable representation of μ_{nm} when n, m are small, the reverse of the conclusion stated in Reference 9.

4.4 Convergence of the Three-Dimensional Solution

In order to check the influence of the number of terms (n, m) on the convergence of the solutions for velocity components at various locations with respect to the vortex filament, calculations were made with varying series lengths. It was known from (9) that convergence becomes more difficult as the filament is approached.

Results presented in (10) show that the number of terms used by in Reference (9) was sufficient to insure the convergence of all three velocity components at $\eta = 0.80$ for $\xi = 0.20$, $\theta = 15^{\circ}$, $\eta_H = 0.6$. Similar results were obtained for $\eta = 0.60$ and $\eta = 1.00$. In attempting to make calculations nearer to the vortex filament the limits of $n = 2$, $m = 26$ are no longer sufficient. In the region $\theta = 5^{\circ}$, $\xi = 0.05$ a series of $n = 6$, $m = 40$ is required with convergence for all three velocity components sensitive to both limits.

It is thus apparent that the series length required for convergence and, therefore, the time required for each calculation is strongly dependent on proximity to the filament. For a hub ratio of 0.60, a series length of $n = 6$, $m = 40$ is apparently adequate to as close as $\theta = 5^{\circ}$, $\alpha = 0.05$.

4.5 Comparison To Previous Results

The calculations of Reference 9 were repeated for the hub ratio of 0.6. Figure 37 for $\xi = 0.20$ and $\theta = 0^{\circ}$ to 180°, shows good agreement for the dimensionless tangential velocity component, C_{θ} at the mid radius, $\eta = 0.80$; but substantial deviation for the hub and tip radii. In general, at all but mid radius, the present calculations indicate a higher value of C_{θ} near the filament and lower value of C_{θ} far away from the filament than the results of (9).

In the case of the dimensionless axial velocity component, C_{ξ}, the present results again agree with Reference 9 at the mid radius, but not at the hub or tip. The present calculations indicate the axial velocity to be greater than reported in (9) for all values of θ.

It is difficult to explain the discrepancies between the present calculations and the previous results (9), especially since the eigenvalues have been shown to agree and the dimensionless velocities agree at the mid radius. One might only conclude that the calculations of (9) done in 1952 and probably by desk calculator may have contained certain systematic computational errors not found in the present calculations by high speed computer.

4.6 The Two-Dimensional Approximation of the Problem

The complex velocity potential, w at position z due to a single rectilinear (two-dimensional) vortex filament with circulation, Γ, at position z_1 is given by

$$w = \frac{\Gamma}{2\pi} i \ln (z - z_1) \qquad [24]$$

For a series of 2n + 1 vortices of equal strength spaced along the x axis at intervals, a, with the center filament at the origin, the potential is

$$w = \frac{i\Gamma}{2\pi} \ln z \, (z-a)(z+a)(z-2a)(z+2a)\ldots(z-na)\,(z+na)$$

This may be rewritten

$$w = \frac{i\Gamma}{2\pi} \ln \left[\frac{\pi z}{a} \left(1 - \frac{z^2}{a^2}\right) \left(1 - \frac{z^2}{4a^2}\right) \ldots \left(1 - \frac{z^2}{n^2 a^2}\right) \right] + \text{constant}$$

Neglecting the constant term which has no influence on the velocity and allowing $n \to \infty$

$$\omega = \frac{i\Gamma}{2\pi} \ln \sin \left(\frac{\pi z}{a} \right) \qquad [25]$$

The resulting complex velocity is

$$-\frac{d\omega}{dz} = u - iv = -\frac{i\Gamma}{4\pi a} \cot \frac{\pi z}{a} \qquad [26]$$

where

u = the complex velocity component in the x direction, and

v = the complex velocity component in the y direction.

Separating real and imaginary parts,

$$u = -\frac{\Gamma}{2a} \frac{\sinh \frac{2\pi y}{a}}{\cosh \frac{2\pi y}{a} - \cos \frac{2\pi x}{a}} \qquad [27a]$$

$$v = \frac{\Gamma}{2a} \frac{\sin \frac{2\pi x}{a}}{\cosh \frac{2\pi y}{a} - \cos \frac{2\pi x}{a}} \qquad [27b]$$

If the spacing, a, is taken to be $2\pi\eta$ and the following substitutions are made

$$y = \xi$$

$$x = \theta\eta$$

$$C_\theta = u/\Gamma$$

$$C_\xi = v/\Gamma$$

we obtain

$$C_\theta = -\frac{1}{4\pi\eta}\frac{\sinh(\xi/\eta)}{\cosh \xi/\eta - \cos\theta} \qquad [28a]$$

$$C_\xi = \frac{1}{4\pi\eta}\frac{\sin\theta}{\cosh \xi/\eta - \cos\theta} \qquad [28b]$$

These are the two-dimensional approximations to the non-dimensional axial and tangential velocities for a vortex filament in an annulus. The radial velocity of course is assumed zero at all points. The hub/diameter ratio does not appear since in two dimensions it has no significance.

These equations are of the same form used in Reference 9 to calculate limited two-dimensional results for comparison to the three-dimensional case. HYDRONAUTICS has programmed the solution to these equations and calculated C_ξ and C_θ for values of $\eta = 0.5$, to 1.0, $\theta = 5^\circ - 90^\circ$ and $\xi = 0.01$ to .80. Typical results as presented in Figures 38 and 39.

4.6.1 <u>The 0.60 Hub Ratio Case</u> - Figure 40 shows the variation of the ratio of 3-D tangential velocities to 2-D values for $\xi = 0.80$. From this figure it can be seen that the mid-radius velocities are equal to the two-dimensional values while the hub and tip values deviate by as much as 20 percent. The hub and tip curves are nearly mirror images of each other about the 1.0 line. The "cross-over" point where hub, tip and mid-values are all near the 2-D values moves closer to the filament in a tangential direction as the plane under consideration moves closer to the filament in an axial direction.

4.6.2 The 0.70 and 0.80 Hub Ratio Cases - Similar results were obtained when calculations were made for η_H of 0.70 and 0.80. Again, the mid radius values were in agreement with the 2-D results while the hub and tip values showed the typical systematic mirror-image deviation from the 2-D values. Figure 41 shows that the 3-D results more closely approach the 2-D values when the hub ratio is increased, an intuitively correct relationship.

4.7 Sample Interference Streamline Calculations

Appendix A of reference (10) presents a tabulation of the eigenvalues, μ_{nm}, and coefficients B_{nm} and β_{nm}/γ_{nm} required for the evaluation of Equation [21] for hub/diameter ratios of 0.60, 0.70 and 0.80. Appendix B of reference (10) presents a tabulation of the three-dimensional non-dimensional velocities calculated for the case of $\eta_H = 0.70$ and $\eta = 0.70$ .775, .850, .925, 1.00. The calculations of Appendix B were made with limits of n = 2, 4, or 6 and m = 26 or 40 depending on proximity to the filament and convergence of the three-dimensional solution.

Bowerman (4) has presented a technique for pump impeller design which utilizes the results of the three dimensional velocity field calculation previously presented. The technique allows the design of an impeller without the use of experimental or theoretical cascade data. This is especially helpful in the case of inducers where high solidity and high stagger angles are required, since cascade performance in this range is not known. The lack of knowledge of cascade performance in this range is a major factor in the adoption of a simple, helical blade to inducer applications.

In Reference 1, the second stage of a tandem-row inducer was designed using the Bowerman design technique. Tests of this stage indicated the need for empirical modifications to improve performance. The results given by Tyson (9), however, were used in this design and as previously shown the present calculations disagree substantially with the results of (9) at all but the mid radius.

Using the present three-dimensional results, a sample interference streamline calculation was conducted using the following conditions:

Impeller diameter = 7.0"
Diameter under consideration, $\eta = 1.00$
Hub/diameter ratio, $\eta_H = 0.70$
Lift parameter, $C_L(C/D) = 0.493$
Solidity, $C/D = 1.795$
Chord, $c = 9.87"$
Axial extent ratio, $\xi_t = 0.641$

Diffusion factor = 0.275
Number of blades = 4
Vortex filaments/blade = 6
Design flow coefficient = 0.10
2nd stage design head coefficient = .2125
rpm of impeller = 4000
1st stage design head coefficient = .0375

Figure 42 indicates the variation of $C_{\theta_{\text{total}}}$ with axial location, ξ, as obtained using the three-dimensional and two-dimensional results. While there are discernable differences, the calculation indicates that, at least for hub/diameter ratios of 0.70 or greater, there is not enough difference between the results to justify the calculation of the more complicated three-dimensional values.

4.8 Summary and Conclusions

In summary:

(a) A computer program to solve the three-dimensional flow field from a radial vortex filament in a cylindircal annulus has been written.

(b) The convergence of the solutions depends on proximity to the vortex filament, with more and more terms required in the summation as the filament is approached in either the axial or tangential direction.

(c) The eigenvalues used in Reference 9 agree with the present values. The series representation of the eigenvalues (30) is valid for small values of m and n only.

(d) Considerable disagreement was found between the present three-dimensional results and the results reported in Reference 9 except at the mid-radius.

(e) A systematic deviation was found between the present three-dimensional calculations and the two-dimensional approximation with maximum differences on the order of 25 percent. The larger the hub/diameter ratio, the closer the three-dimensional results are to the two-dimensional.

(f) Eigenvalues and coefficients required for the three-dimensional calculations at hub/diameter ratios, η_H, of 0.60, 0.70 and 0.80 and actual velocities for $\eta_H = 0.70$ are tabulated in Reference 10.

(g) A sample interference streamline calculation showed little difference between $C_{\theta_{total}}$ using three-dimensional results or two-dimensional results in the summation in the case of $\eta_H = 0.70$. For this case, therefore, the more complicated three dimensional calculations are unjustified.

5.0 FIRST AND SECOND STAGE INDUCER DESIGNS

5.1 Basic First Stage Design Procedure

A basic difference in the form of the output of the higher term cambered supercavitating cascades (7) from that of the previously calculated constant pressure cambered cascades (2) leads to a slightly modified design procedure for the first stage.

To review the design procedure for the constant pressure cambered blades, the following general outline was followed:

(a) Select the desired flow coefficient, φ_o; head coefficient, ψ; maximum suction specific speed, N_{ss}; tip diameter, D_t; hub ratio, D_h/D_t; rpm; and head distribution between first and second stages.

(b) Choose a form of radial head variation (free vortex or constant head with radius has been used) and calculate the swirl (ΔV_u) variation from the required "Euler head", $\Delta V_u = gH/U$.

(c) Construct the inlet and outlet velocity triangles and calculate the local cavitation number variation, σ_ℓ.

(d) Assume a mean angle of attack (therefore lift/drag ratio) for the foils and using this and the cascade stagger get the cascade efficiency, η.

(e) Compute the required $\frac{C_L}{\sigma}\frac{c}{d}$ from

$$\frac{C_L}{\sigma}\frac{c}{d} = \frac{2gH}{\sigma w_1^2}\frac{V_f}{U\eta}\frac{\cos\alpha_1}{\cos(\beta_1 - \alpha_1)} \quad \text{(ref. 1)}$$

(f) From the theoretical plots of $\frac{C_L}{\sigma}\frac{c}{d}$ versus c/d for the desired cavity length, ℓ/c, obtain the required c/d and ratio α/C_L

(g) Calculate C_L from $\frac{C_L}{\sigma}\frac{c}{d}$, σ, and c/d

(h) Knowing C_L and α/C_L, calculate α and check to see if $\alpha = \alpha$ assumed in step (d). If $\alpha \neq \alpha$ assumed choose a new α and iterate until agreement is obtained.

(i) When iteration is complete, check the design against the Yeh (5) stability criterion. If the flow is shown to be unstable, the usual step is to reduce the first stage head coefficient and repeat the design.

Other non-hydrodynamic design considerations include leading edge radius and blade strength. The blade shape is uniquely determined once the stagger, angle of attack, cavity length and $(C_L/\sigma)(c/d)$ are fixed in the above procedure. The method does not permit off design point performance to be computed since each change in flow conditions results in a new and unique blade profile to satisfy the constant pressure cambered condition.

In the case of the higher term cambered (or more properly, arbitrarily cambered) case, the theory of Hsu (7) was used to generate cascade characteristics. The design procedure developed to utilize these results is outlined by the following:

(a) Select the desired flow coefficient, φ_o; head coefficient, ψ; maximum suction specific speed, N_{ss}; tip diameter, D_t; hub ratio, D_h/D_t; rpm; and head distribution between first and second stages.

(b) Choose the form of radial head variation (again free vortex or constant head with radius has been used) and calculate the swirl (ΔV_u) variation from the required Eulerhead, $\Delta V_u = \frac{gH}{U}$.

(c) Construct the inlet and outlet velocity triangles and calculate the local cavitation number variation, σ_ℓ .

(d) Calculate the required value of $\frac{C_L}{\sigma}\frac{c}{d}$ from $\frac{C_L}{\sigma}\frac{c}{d} = \frac{2gH}{\sigma U^2}\sin\beta$. (ref. 1)

(e) Select the desired camber type (circular arc, 2-term, 3-term or 5-term cambered) and an arbitrary camber coefficient, k.

(f) From a plot of cavitation number, σ, versus solidity, c/d for various angles of attack, α_o, (for the stagger angle, camber type, and camber coefficient selected) assume a value of c/d and get the corresponding α_o for the local cavitation number.

(g) From the corresponding $\frac{C_L}{\sigma}\frac{c}{d}$ versus c/d plot (for the long ℓ/c range as discussed in Section 2.3) using the value of α_o selected find the value of c/d which yields the required $\frac{C_L}{\sigma}\frac{c}{d}$. If this c/d doesn't agree with the one selected in step (f), return to step (f) and repeat. Continue to iterate until the values agree.

(h) Using the value of c/d and σ obtain the value of C_L from $\frac{C_L}{\sigma}\frac{c}{d}$. As a check compare this to the value on the plot of C_L versus c/d for the required α_o.

(i) Repeat steps (b) - (h) for a range of camber coefficients and radii of interest. Then using the results, construct the following plots for each radius.

C_L versus k

c/d versus k

and α_o versus k

for constant σ, $\frac{C_L}{\sigma}\frac{c}{d}$, and β.

These plots then allow flexibility in the choice of camber coefficient for a given design requirement.

(j) Select an arbitrary design parameter variation which is desired to be characteristic of the design. For example, one might choose:

linear C_L variation with radius
constant chord length with radius
constant solidity
linear chord length variation
or some other variation as desired.

(k) After selection of the parameter variation in step (j), use the C_L, c/d, and α_o versus k plots to select the final cascades required for the design.

(l) From the theory, calculate the exact cascades required and check against the interpolated values. If the agreement is satisfactory, check the stability of the design using the Yeh (5) stability criterion. If unstable, reduce the stage 1 head coefficient and repeat the design procedure.

Once a particular design has been selected, the off design (still supercavitating) performance can be estimated through modification of the flow coefficient. A change in φ_o for a given cascade geometry changes both the angle of attack and stagger angle of the cascade. This calculation is possible since the geometry of the blades is independent of the flow conditions. That is, any solidity, camber type and camber coefficient may be computed at any stagger angle and angle of attack within the limits of the range of cascades calculable using the theoretical method.

Basic structural considerations are similar to those presented in Reference 1. The overriding requirement for supercavitating sections is always that the upper surface of the foil lie within the cavity generated by the wetted portion of the blade. When this condition is satisfied, the upper surface does not contribute to the hydrodynamics of the flow and is entirely determined from structural considerations.

The relationship between the model and prototype stress is (1)

$$\frac{\text{Model Stress}}{\text{Prototype Stress}} = \frac{\rho_m}{\rho_p}\left(\frac{n_m}{n_p}\right)^2\left(\frac{D_m}{D_p}\right)^2 = k \qquad [29]$$

This is derived by the following reasoning. The hydrodynamic force on any element is determined in general by

$$F \sim C_F \, \rho \frac{V^2}{2g} D^2 \qquad [30]$$

where F is any hydrodynamic force

C_F is a force coefficient determined entirely from geometry

ρ is the fluid density

V is a representative velocity

D is a representative length (diameter)

The representative velocity and stress can be characterized by:

$$V \sim nD \text{ and } \sigma \sim F/D^2$$

Substituting those values

$$\sigma \sim F/D^2 \sim C_F \, \rho \frac{n^2 D^2 D^2}{2g \; D^2} \sim C_F \rho n^2 D^2$$

If the model and prototype are geometrically similar, $C_{F_{model}} = C_{F_{proto}}$.

$$\therefore \frac{\sigma_{model}}{\sigma_{prototype}} = \frac{\rho_m}{\rho_p} \left(\frac{n_m}{n_p}\right)^2 \left(\frac{D_m}{D_p}\right)^2 \qquad [31]$$

which is the form of Equation [29]. As discussed in Reference 1 a survey of typical rocket inducers established a range of k values of 0.2 - 0.4 for the models presently under consideration.

If the titanium alloy Ti-Al6-V4 is assumed for the prototype, the fatigue limit with a load factor of 0.40 at room temperature in a non-corrosive environment is about 100,000 psi (31). A factor of safety of 2 will provide a prototype design stress of 50,000 psi or a model design stress of 10,000 psi. It should be noted that the selection of the load factor and factor of safety in this case was arbitrary. In addition the ultimate strength and yield stress of Ti-Al6-V4 increases by nearly 100 percent as the temperature is reduced from 78°F to -420°F (31). This behavior is typical for most metals and alloys (32). Thus the use of room temperature values appears extremely conservative for cyrogenic applications. Fatigue data in LH_2 or LOX, however, is not available and stress-corrosion considerations may severely reduce the allowable design stress. Further discussion of the material problems in a prototype inducer is beyond the scope and intent of the present study.

The critical stress in supercavitating foil sections as are presently being considered is nearly always in the leading edge chordwise bending mode.

Experience with supercavitating propellers has indicated that calculation of the chordwise bending stress at a location 20 percent from the leading edge provides a good criterion for maximum stress in this mode. This greatly simplified calculation which considers the blade to be composed of an infinite number of parallel and independent cantilever beams has also been checked using a complex stress calculation based on a shell structure of varying thickness and non-uniform loading. Agreement between the complex and simplified methods has been within 5 - 10 percent. This is very close agreement considering the assumptions of the simplified approach. The same approach is therefore used for the stress calculation in a supercavitating inducer blade.

Figure 43 based on (6) shows the theoretical pressure distributions on four isolated supercavitating foil sections showing the separate contributions of camber and angle of attack. The total pressure distribution on a foil section may be obtained from

$$\left(C_p\right)_{total} = \left(\frac{C_p}{C_{L_{camber}}}\right)\left(C_{L_{camber}}\right) + \left(\frac{C_p}{C_{L_\alpha}}\right)\left(C_{L_\alpha}\right) \qquad [32]$$

Note that near the leading edge (first 30 percent of chord) the contribution due to 5-term camber is near zero while the angle of attack contribution is maximum in this region.

The stress calculation for chordwise bending over the leasing 20 percent of the blade need, therefore, only include the angle of attack contribution to load in this region. The loading can be approximated by three rectangles and three triangles as shown in Figure 43. Using this dimensionless loading pattern and the rectangular cross-section of each cantilevered portion of the blade leading edge, we may derive the following equation for the stress in bending at the 0.20 chord.

$$\sigma_{B.M.} = 0.30 \left(\frac{c}{t_{.20}}\right)^2 C_{L_\alpha} \rho w_1{}^2 \text{ psf.} \qquad [33]$$

5.2 First Stage Design

As described in Section 5.1, a considerable degree of freedom exists in selection of the higher term cambered geometry. Section 2.3.4 compared the various camber types and as shown in Figures 29 and 31, the five-term cambered shape (with the center of pressure shifted further aft than the other shapes) showed the best performance in terms of lift coefficient over a range of both stagger angles and solidities. For this reason, the five term cambered shape was selected for the present first stage design. In addition, the approximate second order results were used rather than the first order results as described in Section 2.3.

For a first design, the chord length variation was specified to be linear with radius and to closely approximate the chord length variation which resulted from the first stage constant pressure cambered design of Reference 1. Table 5 presents the results of this design.

TABLE 5

Summary of Stage 1 Two Bladed, Second Order Design Using Five-Term Cambered Sections and Specified Linear Chord Length Variation

Quantity	Tip Radius R = 3.50"	Mid-Radius R = 2.80"	Hub Radius R = 2.10"
Head Coefficient, ψ	.0375	.0375	.0375
Cavitation Number, σ	.0132	.0203	.0352
Peripheral Speed, U, fps	122.2	97.9	73.3
Relative Inlet Angle, β_1	$81^{\circ}07'$	$78^{\circ}56'$	$75^{\circ}22'$
Relative Mean Angle, β_{∞}	$80^{\circ}55'$	$78^{\circ}36'$	$74^{\circ}36'$
Relative Outlet Angle, β_2	$80^{\circ}46'$	$78^{\circ}17'$	$73^{\circ}45'$
Axial Flow Velocity, V_f, fps	19.12	19.12	19.12
ΔV_u, fps	4.58	5.72	7.65
$\frac{C_L}{\sigma}\frac{c}{d}$	5.62	5.66	5.72
c (inches)	5.50	4.75	4.00
Nominal Ref. Line Angle of attack, α_1	7.10°	8.80°	11.65°
Geometric Chord Line Angle of attack, α_c	5.63°	6.78°	8.80°
Solidity, C/D	.500	.540	.606
Camber coefficient, k	.152	.206	.291
Section Efficiency, η	.604	.613	.627
Lift Coefficient	.148	.213	.332

Overall conditions:

discharge, Q = 1464 gpm = 3.26 cfs
tandem total head = 116 ft.
first stage total head = 17.40 ft
tandem specific speed, N_s = 4310
first stage specific speed, N_s = 18,010
pump rpm = 4000
NPSH = 8.81 ft.
number of blades = 2

Figure 44 shows a sketch of the model as designed. If the back surface of the balde is allowed to follow a helical shape as shown, the structural analysis as described in Section 5.1 yieldsmodel design point stresses as follows:

shear stress at hub - 103 psi
spanwise bending stress at hub - 1100 psi
tensile centrifugal stress at hub - 560 psi
chordwise bending about 20 percent chord at tip - 6100 psi

As can be seen, the first three stresses are negligible when compared to chordwise bending.

For an allowable prototype stress of 50,000 psi, the maximum ratio of σ_m/σ_p is.122. This makes the model under consideration structurally compatible with a prototype LOX inducer 8 inches in diameter and operating at 10,000 rpm.

5.3 Second Stage Design

As discussed in Reference 1 the design procedure presented by Bowerman (4) allows the design of axial flow pumps without the use of experimental or theoretical cascade data. This procedure is attractive for the present second stage design since no data exists for the high solidity, high stagger angle cascades required. The original design procedure as presented in (4) made use of the results of (9) in which the distribution of the three dimensional tangential, axial and radial velocity components due to a single radial line vortex in an annular space are given.

The design method consists of representing each impeller blade by a number of radial line vortices. One blade is removed from the impeller and the interference streamline due to all the other blades and the total downstream vorticity is calculated. The camber and thickness distributions are then superimposed on the interference streamline, resulting in the final impeller design.

Section 4.0 discusses the results of (10) in which the calculations of (9) were repeated and extended to cover larger hub diameter ratios then the 0.60 originally calculated. Larger hub diameter ratios were required principally to lower the value of the diffusion factor (33) below the critical value of 0.60 at all radii.

During the tests of the second stage inducer of Phase I (1) neither the total head nor the axial velocity remained constant along the radius as assumed in the design. A contributing factor causing this difficulty was flow separation along the hub section and resulting flow "pile up" at the tip sections. The diffusion factor has been shown to correlate well with limiting blade loading or separation in axial flow compressor blades.

$$D = \left(1 - \frac{w_a}{w_1}\right) + \frac{\Delta V_u}{2(c/d)w_1} \qquad [34]$$

Correlation with NACA compressor data shows that to avoid separation this factor should be less than 0.60. The Phase I second stage design called for diffusion factors at the tip radius, mid radius, and hub radius of 0.259, 0.362, and 0.701 respectively. The diffusion factor at the hub was too large because of the high head coefficient and low peripheral speed. It could have been reduced by increasing the hub diameter ratio, but the necessary annular velocity distributions for the Bowerman method were only available for a 0.60 hub at the time.

For the new second stage design, a hub ratio of 0.70 was chosen. The design technique was that of Bowerman (4) with slight modifications. Specifically, the Bowerman technique results in a prescribed variation of chord with radius as a result of the optimization of cavitation performance.

In the present designs, the variation of chord with radius was arbitrarily prescribed. This is a minor consideration for the high solidity blades and large hub ratio of the present design for which Bowerman's cavitation optimization has little effect. The chord variations considered included:

(a) Constant solidity, C/D
(b) Constant axial extent, ξ_t
(c) Constant chord, C
(d) 180° wrap at hub and 45° leading edge sweep
(e) 180° wrap at hub and 60° leading edge sweep

Case (e) was chosen for a complete design. The parameters of this design are tabulated in Table 6. The overall design utilized the following:

Number of blades - 4
Vortices per blade in Bowerman technique - 6
Camber type - NACA "65"
Thickness distribution - NACA 16-009 function
Thickness - tip 1.5%, mid 2.5%, hub 4.5%
Hub ratio - 0.70

TABLE 6
SUMMARY OF STAGE 2 - FOUR BLADED DESIGN

Quantity	Tip Radius (3.5")	Mid Radius (2.975")	Hub Radius (2.45")
Head coefficient, ψ	0.2125	0.2125	0.2125
Peripheral speed	122.2 fps	103.8	85.5
Axial flow velocity	24.0 fps	24.0	24.0
V_u, inlet	4.57 fps	5.38	6.53
ΔV_u	26.0 fps	30.65	37.20
C_ℓ c/d	.493	.710	1.114
C	9.87 inches	8.95	8.26
C/D	1.795	1.92	2.15
C_ℓ	.275	.370	.519
ξ_t, axial extent	.641	.709	.849
Diffusion factor	.275	.385	.511
θ, tangential extent	157.3°	165.6°	180°
β_1	78° 15'	76° 18'	73° 28'
β_2	76° 51'	73° 54'	68° 56'
β_m	75° 02'	70° 29'	61° 17'

The tangential component of velocity V_u due to all of the other blades is non-dimensionalized as follows:

$$C_\theta = \frac{V_u r_t}{\Gamma} \qquad [35]$$

The value of C_θ in (1) and (4) was found to vary almost linearly with non-dimensional axial distance $\xi = z/r_t$. Thus,

$$C_\theta \approx k_o + k_1 \frac{\xi}{\xi_t} \qquad [36]$$

where ξ_t is the value of ξ at the trailing edge of the foil.

In the present design, a slightly closer fit to the variation of C_θ with ξ was found to be

$$C_\theta = k_o + k_1 \frac{\xi}{\xi_t} + k_2 \sin\left(2\pi \frac{\xi}{\xi_t}\right) \qquad [37]$$

The streamline equation, which defines the streamline at each radius about which the isolated cambered blade shape must be placed is thus found to be

$$\theta = \frac{\xi}{\varphi}\left(1 - \frac{\lambda}{\eta}\right) - \frac{n\Gamma_b}{\varphi r_t^2 \omega \eta}\left[k_o \xi + \frac{k_1}{2}\frac{\xi^2}{\xi_t} - \frac{k_2}{2\pi}\xi_t \cos\left(2\pi \frac{\xi}{\xi_t}\right)\right] \qquad [38]$$

where:

$$\varphi = \frac{V_a}{U_t} = \frac{V_a}{\omega r_t}$$

$$\lambda = \frac{V_{\theta_1}}{u_t} = \frac{V_a}{\omega r_t}$$

n = number of blades

V_a = axial velocity

V_{θ_1} = inlet tangential velocity

$\eta = r/r_t$

$\xi = z/r_t$

Γ_b = circulation per blade

ω = rotational speed

k_o, k_1 and k_2 are as previously defined and based on total circulation for all blades.

The values of k_o, k_1 and k_2 for three radii are presented below:

r/r_t	k_o	k_1	k_2	ξ_t
0.70	.0199	.1875	.010	.849
0.85	.0217	.1441	.010	.709
1.00	.0214	.1162	.008	.641

A camber line of the NACA 67 series was chosen so that the pressure distribution would be such that possible blade cavitation would be minimized (4). A thickness distribution of the NACA 16 series was used. These distributions along with the above design procedure determine the final coordinates of the foil.

Figure 45 shows the final blade profiles for the second stage and Figure 46 presents a view of the three dimensional impeller as it appears when the sections are wrapped around the required 0.70 hub.

REFERENCES

1. Contractor, D. N., and Etter, R. J., "An Investigation of Tandem Row High Head Pump Inducers - Interim Report, Phase I," HYDRONAUTICS, Incorporated Technical Report 703-4, May 1969.

2. Yim, B., "Supercavitating Cascades with Constant Pressure Cambered Blades," HYDRONAUTICS, Incorporated Technical Report 703-2, July 1967. (NASA CR-90426)

3. Yim, B., "The Higher Order Theory of Supercavitating Cascades with Constant Pressure Cambered Blades," HYDRONAUTICS, Incorporated Technical Report 703-3, October 1967. (NASA CR-91444)

4. Bowerman, R. D., "The Design of Axial-Flow Pumps," Trans. ASME, Vol. 78, No. 8, 1956.

5. Yeh, H., "An Actuator Disk Analysis of Inlet Distortions and Rotating Stall in Axial-Flow Turbumachines," Journal of the Aeronautical Sciences, Vol. 26, No. 11, 1959.

6. Johnson, V. E., Jr., "Theoretical and Experimental Investigation of Supercavitating Hydrofoils Operating Near the Free Water Surface," N.A.S.A. Technical Report R-93, 1961.

7. Hsu, C. C., "On the Flow Past a Supercavitating Cascade of Cambered Blades," HYDRONAUTICS, Incorporated Technical Report 703-5, February 1969. (NASA CR-100773)

8. Hsu, C. C., "On the Flow Past a Cascade of Partially Cavitating Cambered Blades," HYDRONAUTICS, Incorporated Technical Report 703-6, March 1969.

9. Tyson, H. N., Jr., "Three-Dimensional Interference Effects of a Finite Number of Blades in an Axial Turbomachine," C.I.T. Report E19.1, November 1952.

10. Etter, R. J. and Van Dyke, P., "Three Dimensional Flow Field from a Radial Vortex Filament in a Cylindrical Annulus," HYDRONAUTICS, Incorporated Technical Report 703-7, December 1969.

11. Hsu, C. C., "Supercavitating Lifting Hydrofoils--Second Order Theory," HYDRONAUTICS, Incorporated Technical Report 121-6, March 1966.

12. Tulin, M. P., "Steady Two-Dimensional Cavity Flow About Slender Bodies," David Taylor Model Basin Report 834, Navy Department, Washington, D. C., May 1953.

13. Muskhelishvili, N. I., Singular Integral Equations, P. Noordhoff, N. B., Groningen, Holland, 1953.

14. Cohen, H. and Sutherland, C. D., "Finite Cavity Cascade Flow," Proceedings of the Third U. S. National Congress of Applied Mechanics, pp. 837-846, American Society of Mechanical Engineers, 1958.

15. Garrick, I. E., "On the Plane Potential Flow Past a Lattice of Arbitrary Airfoils," NACA Report 788, 1944.

16. Acosta, A. J., "Cavitating Flow Past a Cascade of Circular Arc Hydrofoils," California Inst. of Tech., Report No. E-79-2, March 1960.

17. Betz, A., and Petersohn, E., "Application of the Theory of Free Jets," NACA TN 667, April 1932.

18. Numachi, F., "Cavitation Tests on Hydrofoils Designed for Accelerating Flow Cascade," ASME Paper 61-Hyd-1, May 1961.

19. United Aircraft Research Laboratories Report G910254-50 "Systematic Two Dimensional Cascade Tests of Double Circular-Arc Hydrofoils," 1968.

20. Wade, R. B. and Acosta, A. J., "Investigation of Cavitating Cascades," ASME, Journal of Basic Engineering, Paper No. 66-WA/FE-25, December 1967.

21. Pearsall, J. S., "Discussion of Wade and Acosta ASME Paper 66-WA/FE-25".

22. Duller, G., "On the Linear Theory of Cascades of Supercavitating Hydrofoils," NEL Report No. 218, National Engineering Lab., East Kilbride, Glasgow, February 1966.

23. Pearsall, J. S., "The Use of Potential Flow Methods in Designing Cavitating Pumps "in" 1968 ASME Cavitation Forum," ASME Fluids Engineering Conf., May 6, 7, 1968, Philadelphia, Penn.

24. Wade, R. B., "Flow Past a Partially Cavitating Cascade of Flat Plate Hydrofoils, California Institute of Technology Engineering Report No. 79-4, 1963.

25. Geurst, J. A., "Linearized Theory for Partially Cavitated Hydrofoils," Int. Shipbuilding Progress, Vol. 6, No. 60, August 1969.

26. Lewis, George W., et al., "Cavitation Performance of an 83° Helical Inducer Operated in Liquid Hydrogen," NASA TM X-419, March 1961.

27. Soltis, Richard F., et al., "Investigation of the Performance of a 78° Flat Plate Helical Inducer," NASA TM D-1170, March 1962.

28. Montgomery, J. C., "Analytical Performance Characteristics and Outlet Flow Conditions of Constant and Variable Lead Helical Inducers for Cyrogenic Pumps," NASA TM D-583, March 1961.

29. Acosta, A. J., "An Experimental Study of Cavitating Inducers," 2nd ONR Symposium on Naval Hydrodynamics, August 1958.

30. McMahon, J., "On the Roots of the Bessel and Certain Related Functions," Annals of Math. Vol. 9, No. 1, pp. 29, 1894.

31. Titanium Metals Corp. of America, "Titanium Engineering Bulletin No. 1 - Properties of Ti-6Al-4V," New York, February 1965.

32. Scott, Russell B., Cyrogenic Engineering, D. Van Nostrand Co., Princeton, N. J., 1959.

33. Lieblein, S., Schwenk, F. C., and Broderick, R. L., "Diffusion Factor for Estimating Losses and Limiting Blade Loadings in Axial-Flow-Compressor Blade Elements," NACA RM E53D01, June 1953.

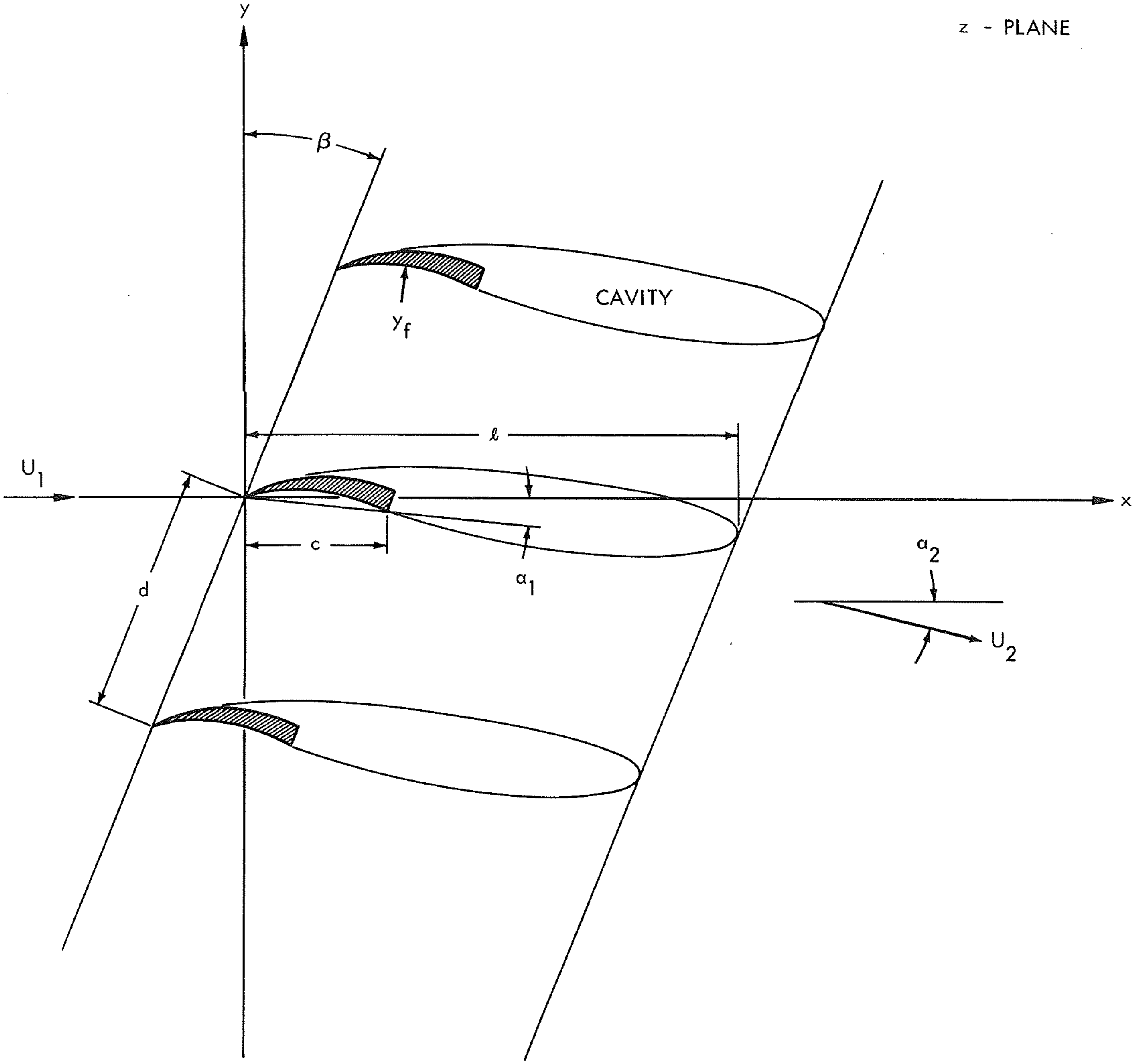

FIGURE 1 - DEFINITION SKETCH FOR A SUPERCAVITATING CASCADE

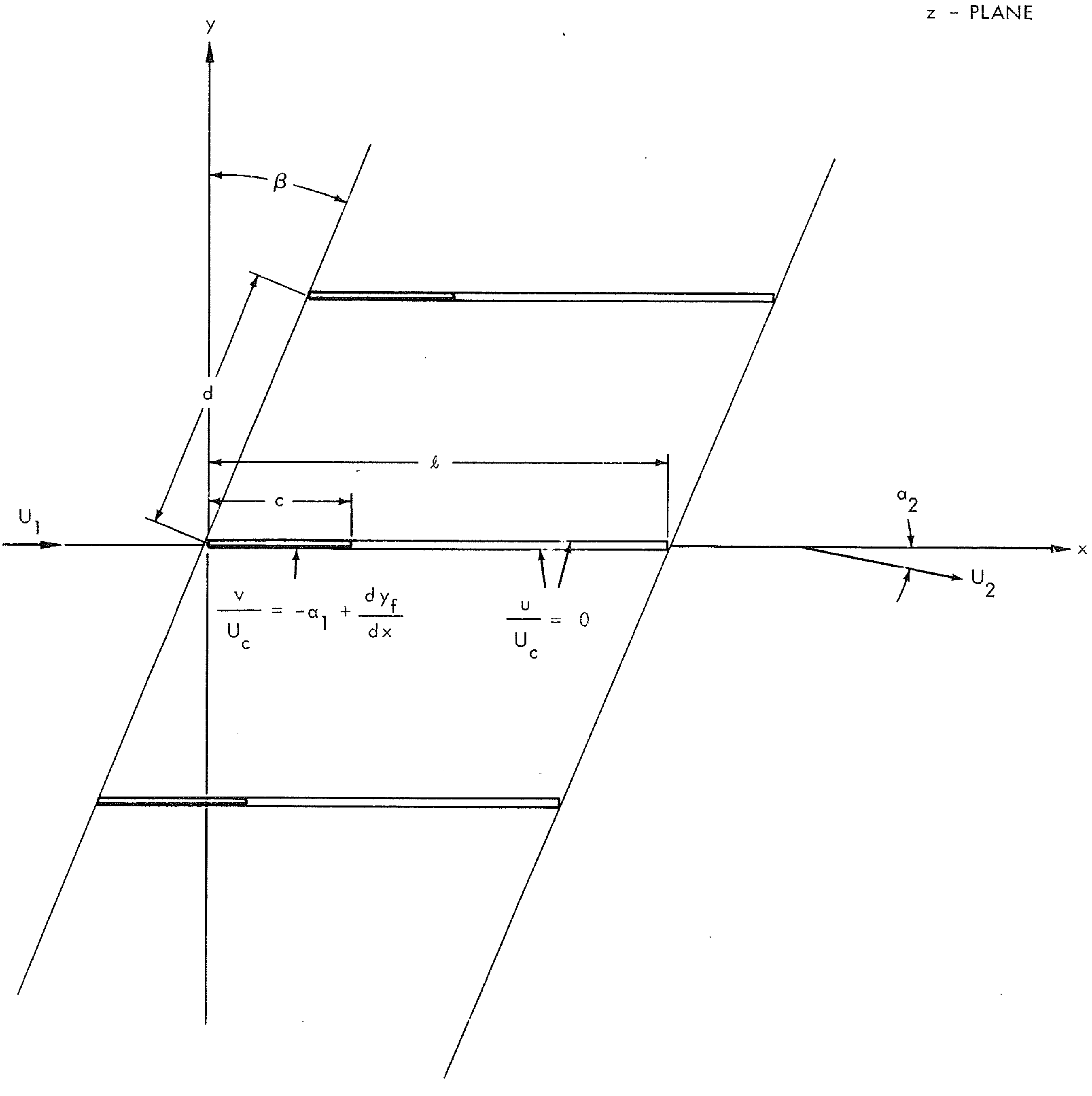

FIGURE 2 - LINEARIZED BOUNDARY VALUE PROBLEM IN THE PHYSICAL PLANE FOR A SUPERCAVITATING CASCADE

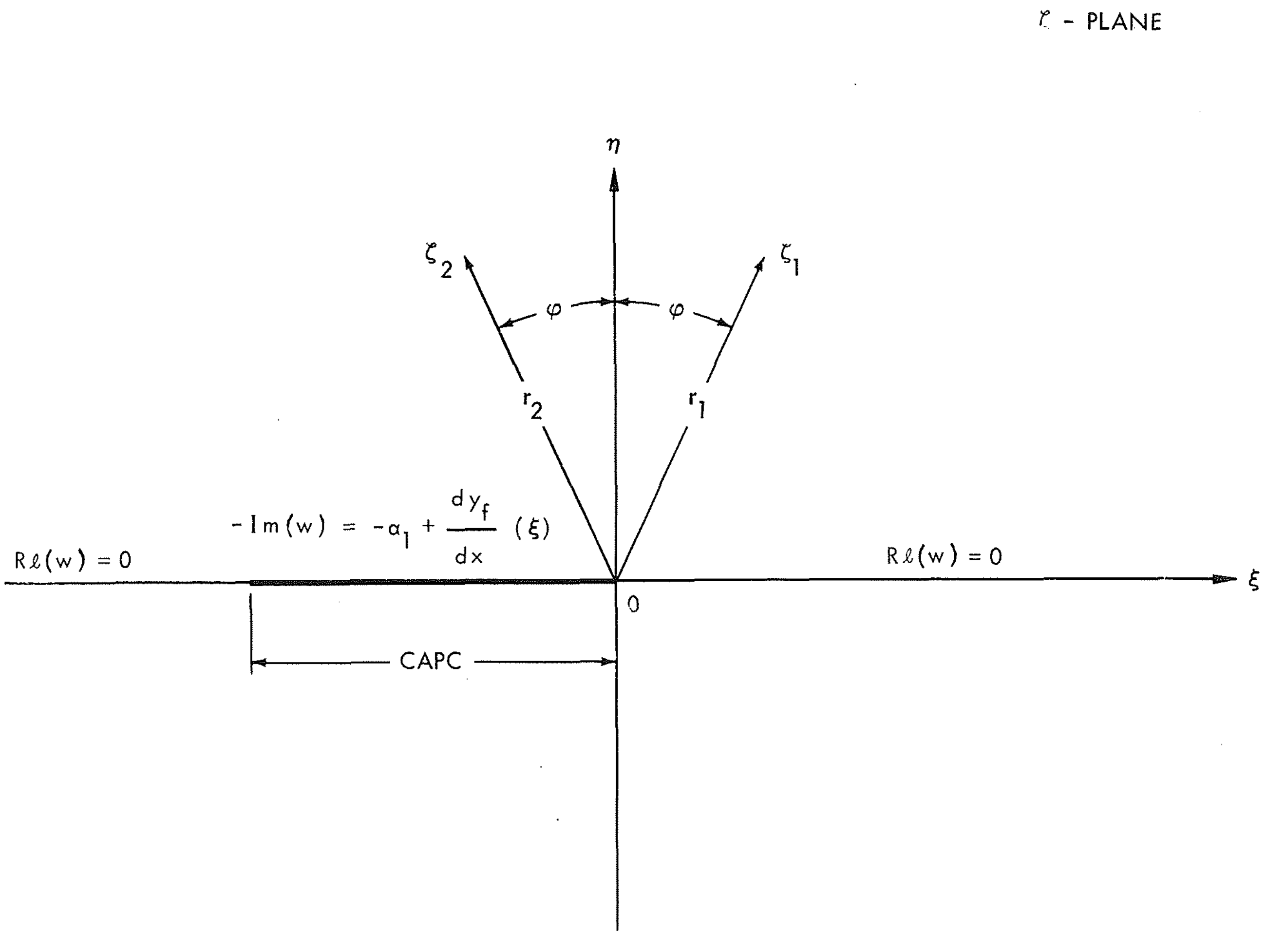

FIGURE 3 - LINEARIZED BOUNDARY VALUE PROBLEM IN THE TRANSFORMED ζ-PLANE FOR A SUPERCAVITATING CASCADE

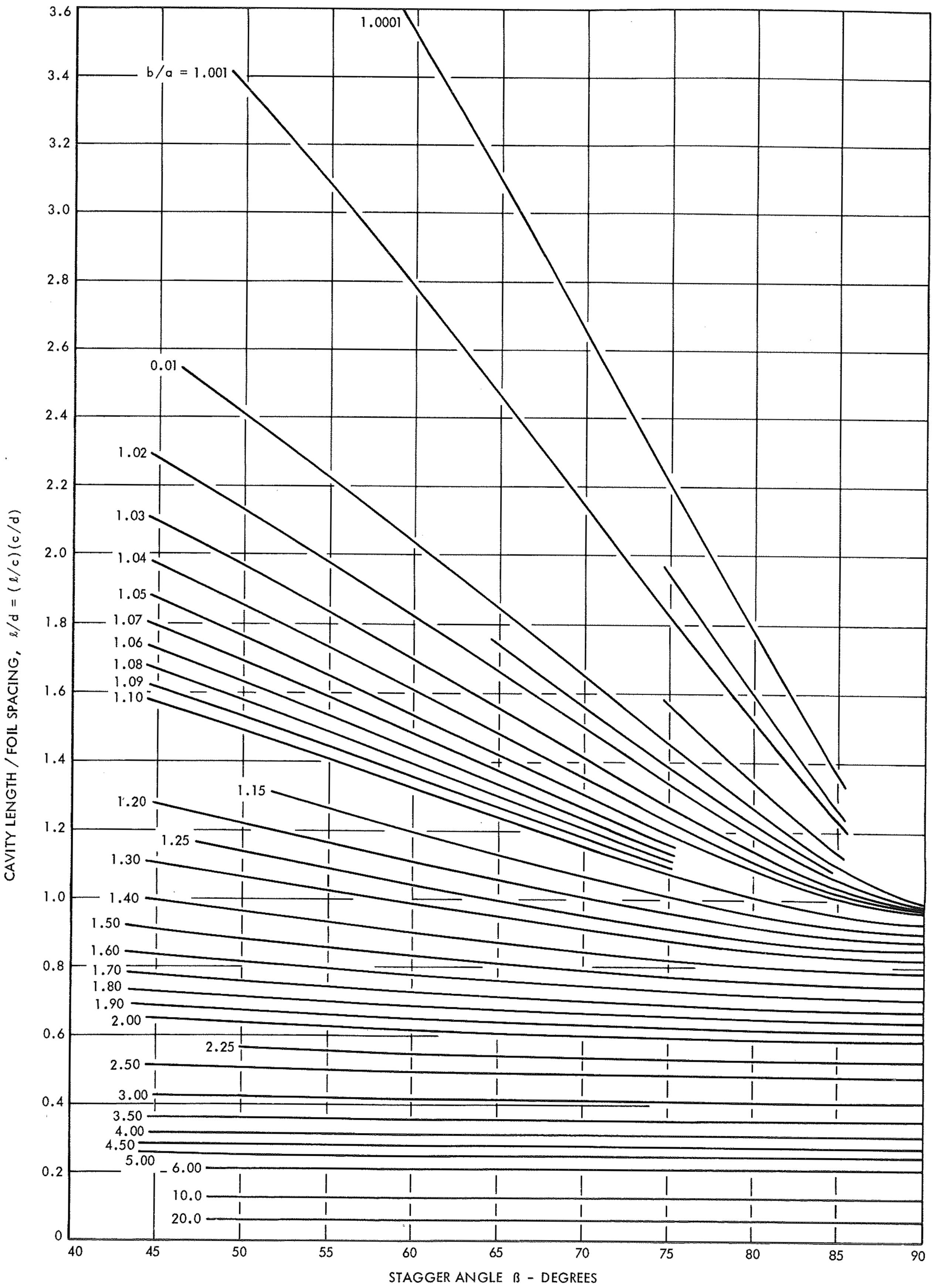

FIGURE 4 - EFFECT OF b/a AND STAGGER ANGLE ON CAVITY LENGTH - FOIL SPACING RATIO

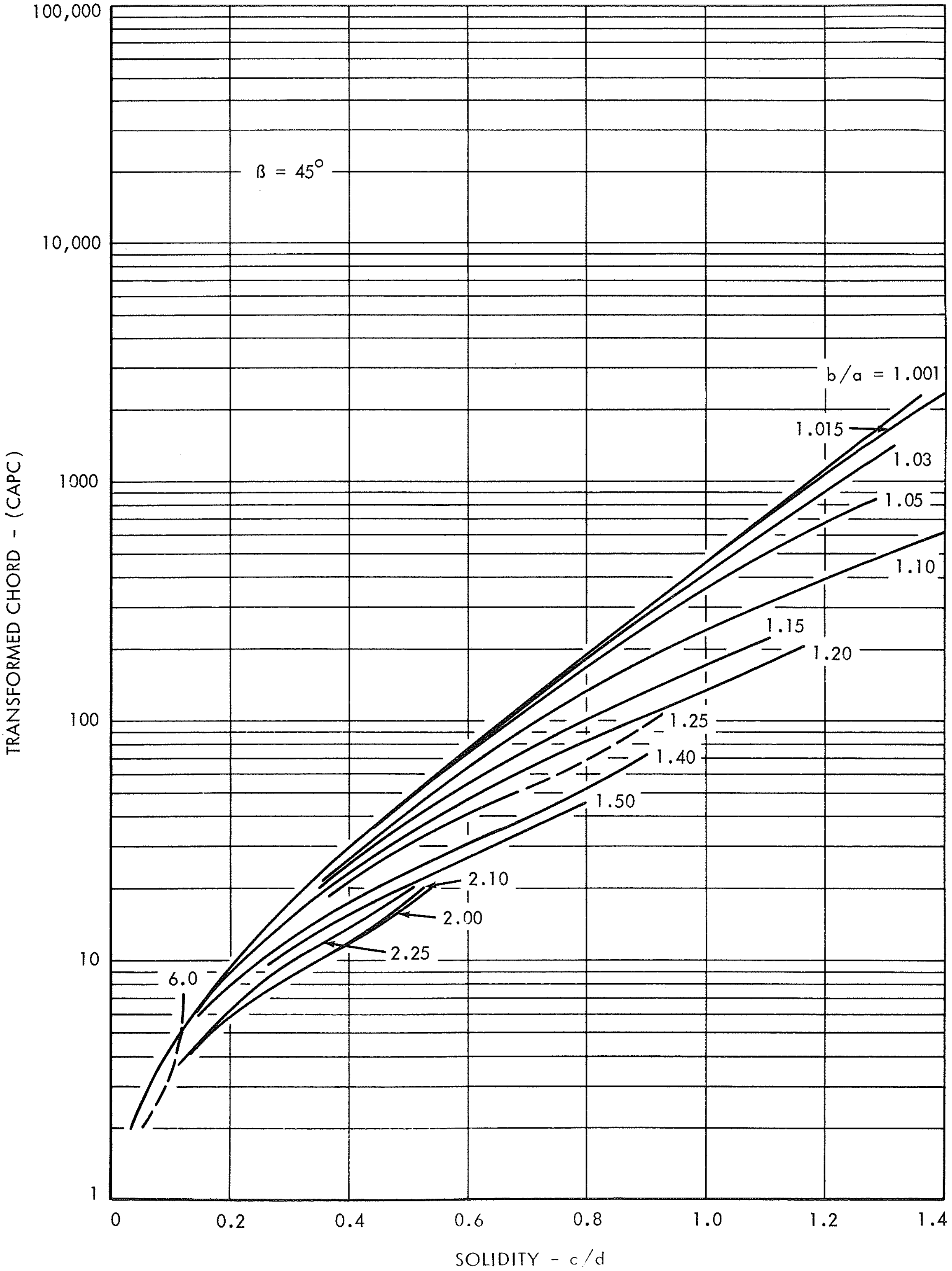

FIGURE 5 - EFFECT OF TRANSFORMED CHORD AND b/a ON SOLIDITY FOR ß = 45°

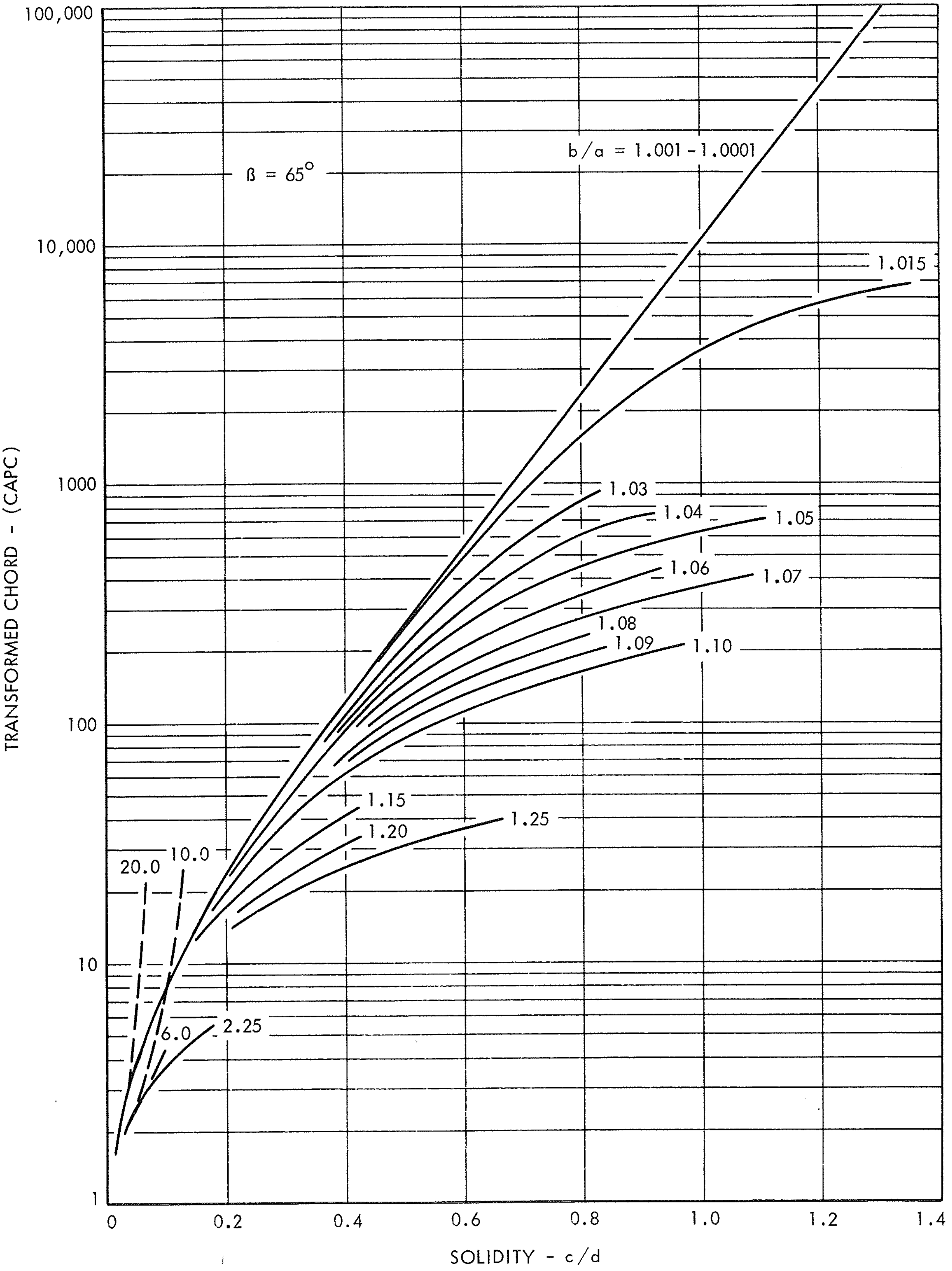

FIGURE 6 - EFFECT OF TRANSFORMED CHORD AND b/a ON SOLIDITY FOR ß = 65°

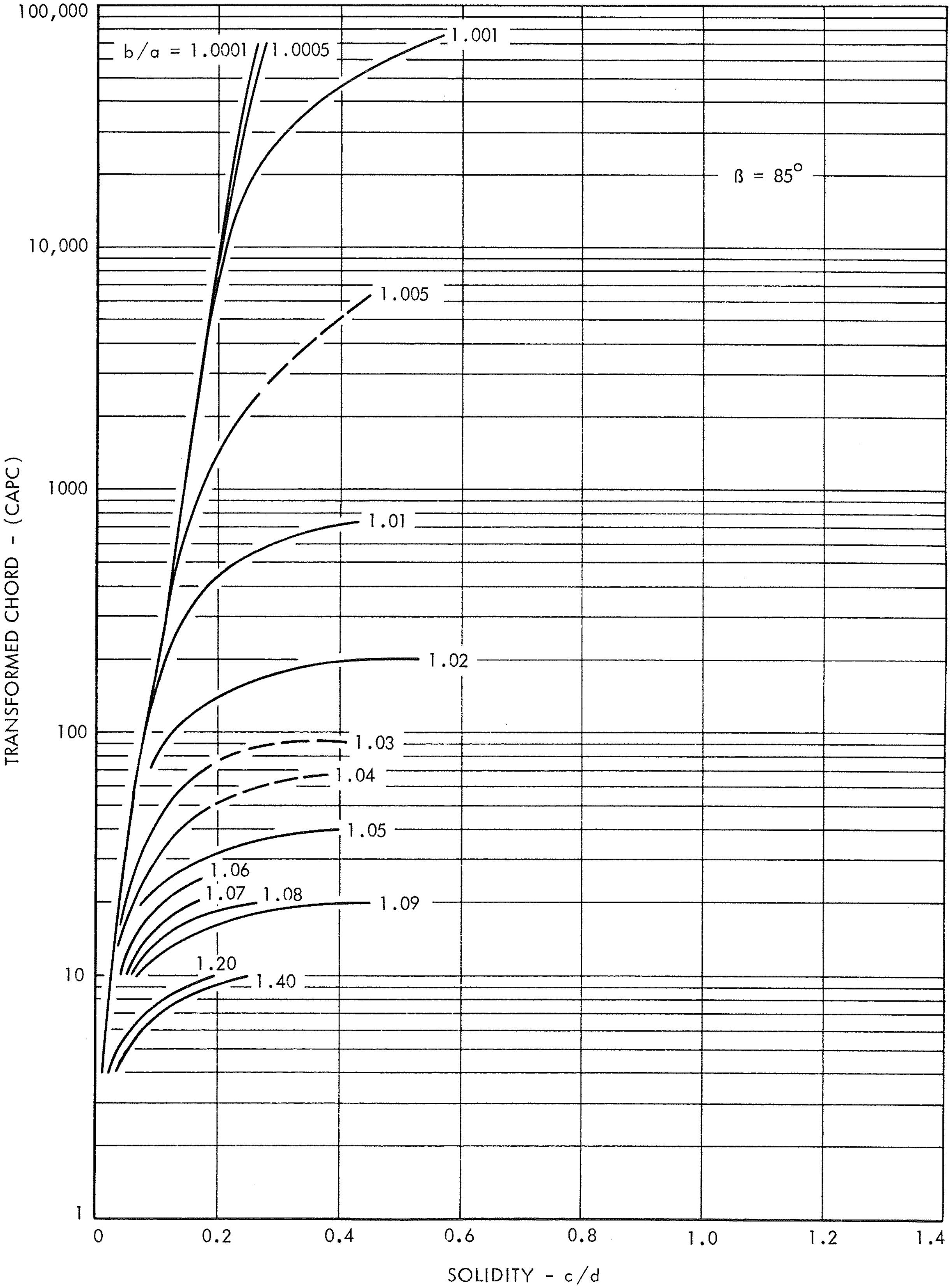

FIGURE 7 - EFFECT OF TRANSFORMED CHORD AND b/a ON SOLIDITY FOR β = 85°

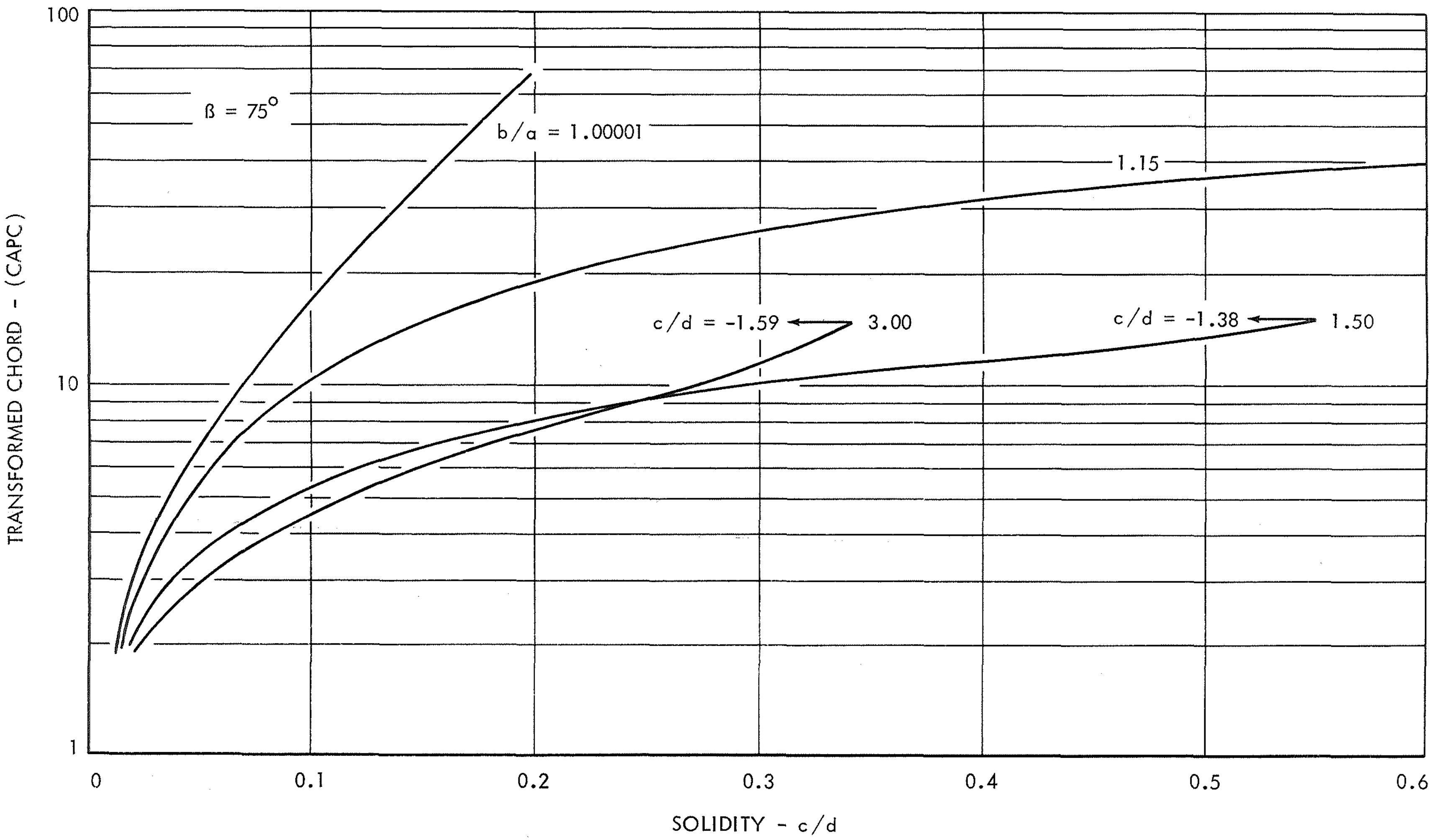

FIGURE 8 - EFFECT OF TRANSFORMED CHORD AND b/a ON SOLIDITY FOR ß = 75°

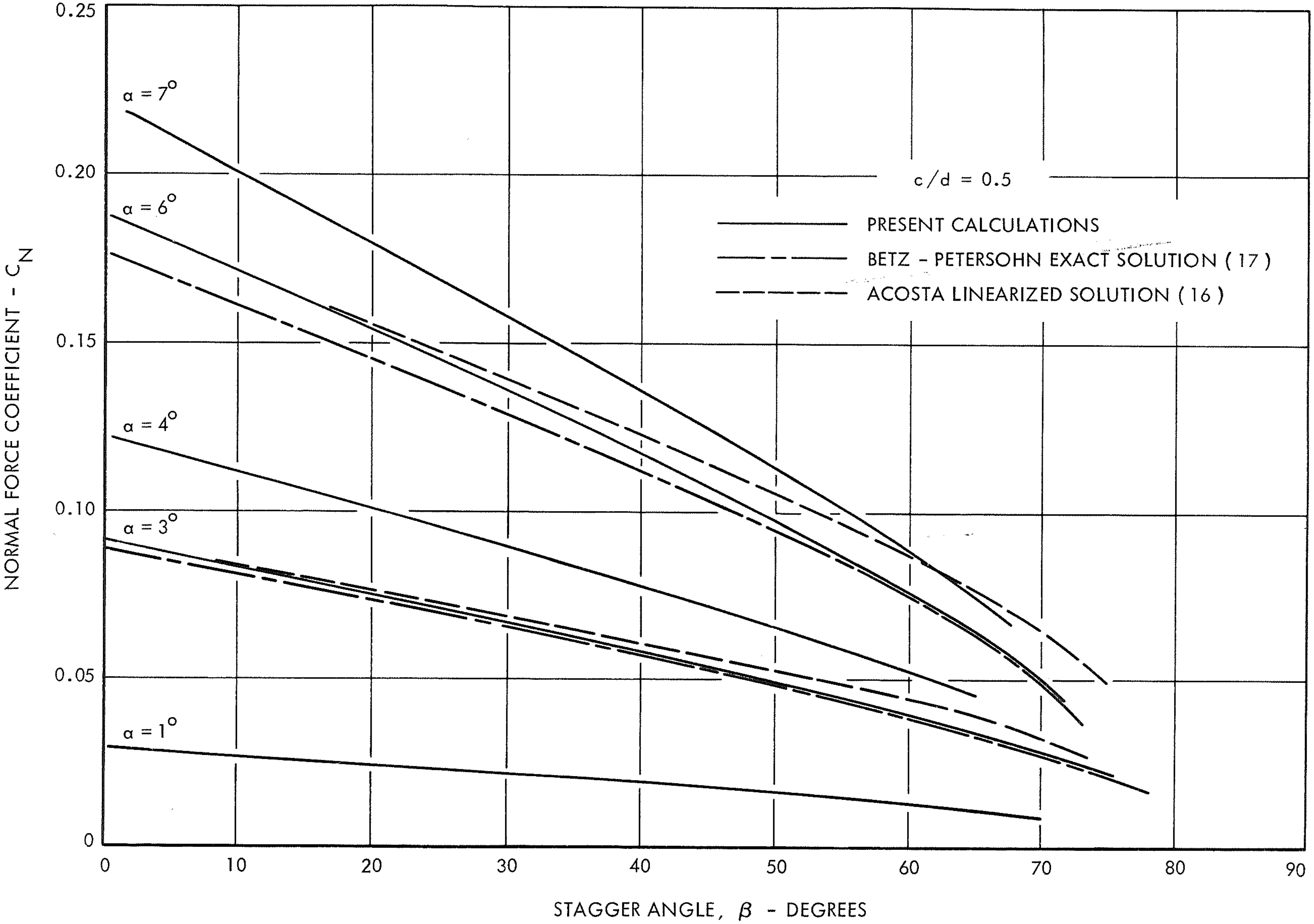

FIGURE 9 - COMPARISON OF PRESENT RESULTS FOR SUPERCAVITATING CASCADES OF FLAT PLATES WITH RESULTS OF BETZ-PETERSOHN (17) AND ACOSTA (16) FOR A SOLIDITY (c/d) OF 0.50.

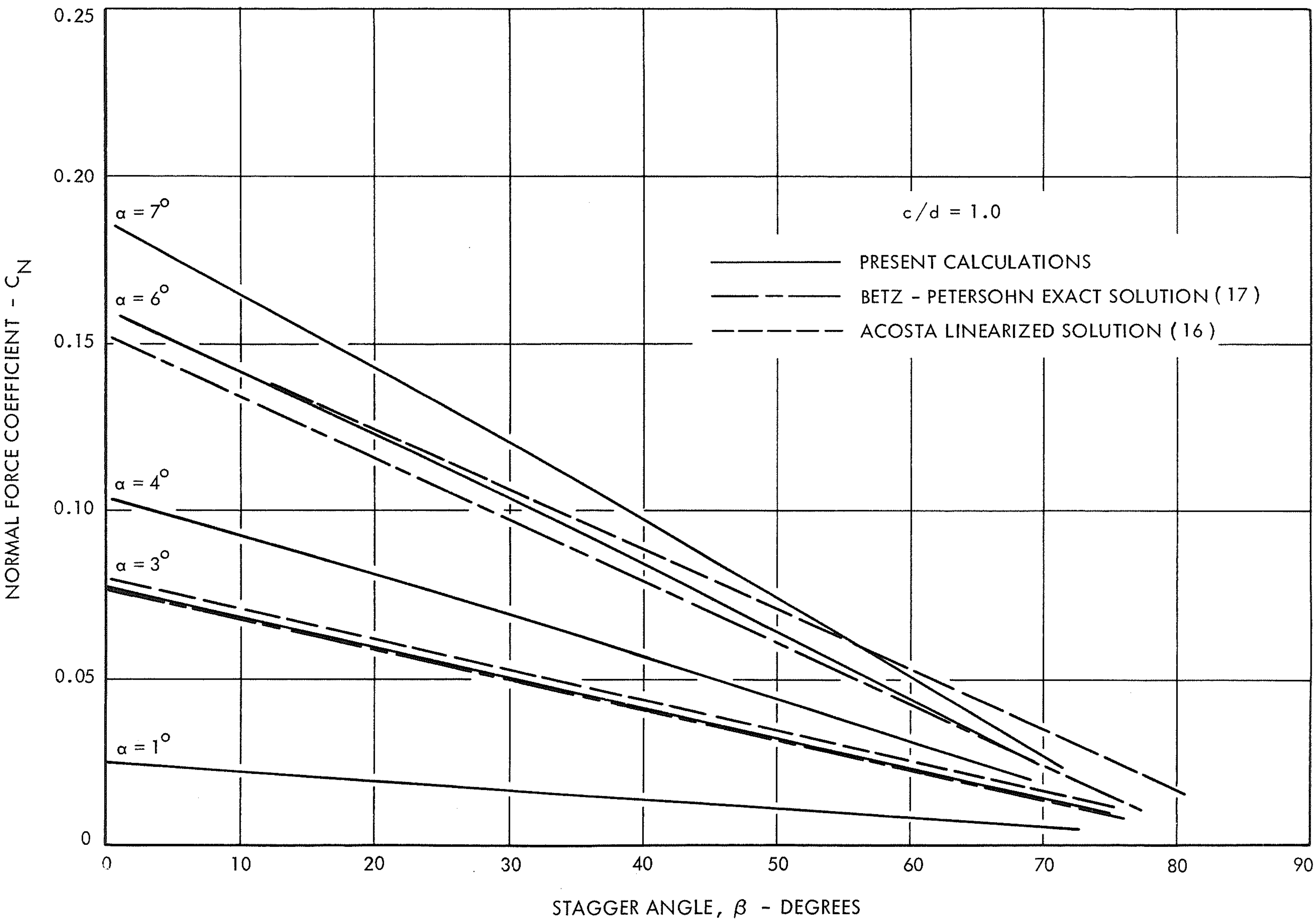

FIGURE 10 - COMPARISON OF PRESENT RESULTS FOR SUPERCAVITATING CASCADES OF FLAT PLATES WITH RESULTS OF BETZ-PETERSOHN (17) AND ACOSTA (16) FOR A SOLIDTY (c/d) OF 1.00.

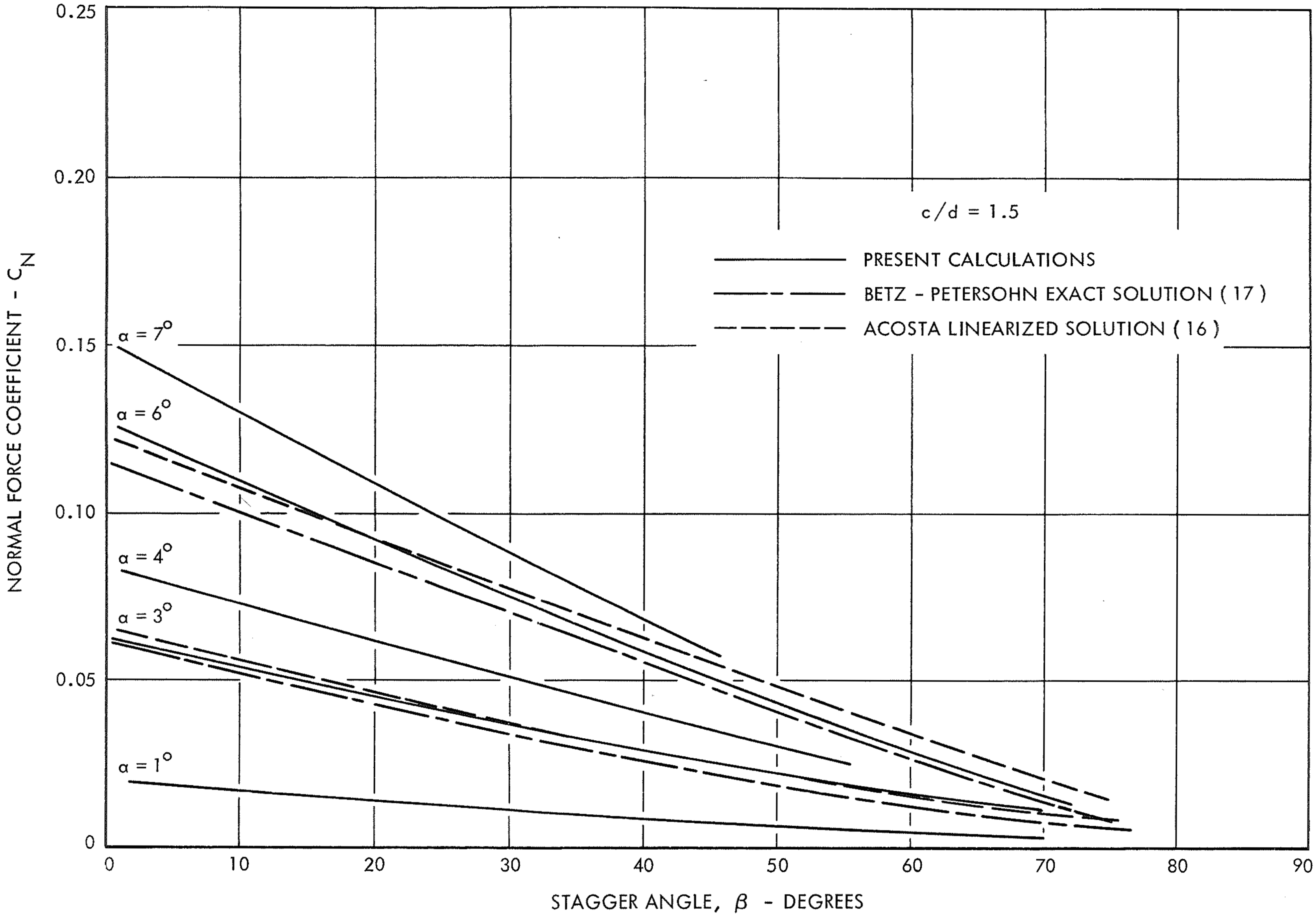

FIGURE 11 - COMPARISON OF PRESENT RESULTS FOR SUPERCAVITATING CASCADES OF FLAT PLATES WITH RESULTS OF BETZ-PETERSOHN (17) AND ACOSTA (16) FOR A SOLIDITY (c/d) OF 1.50.

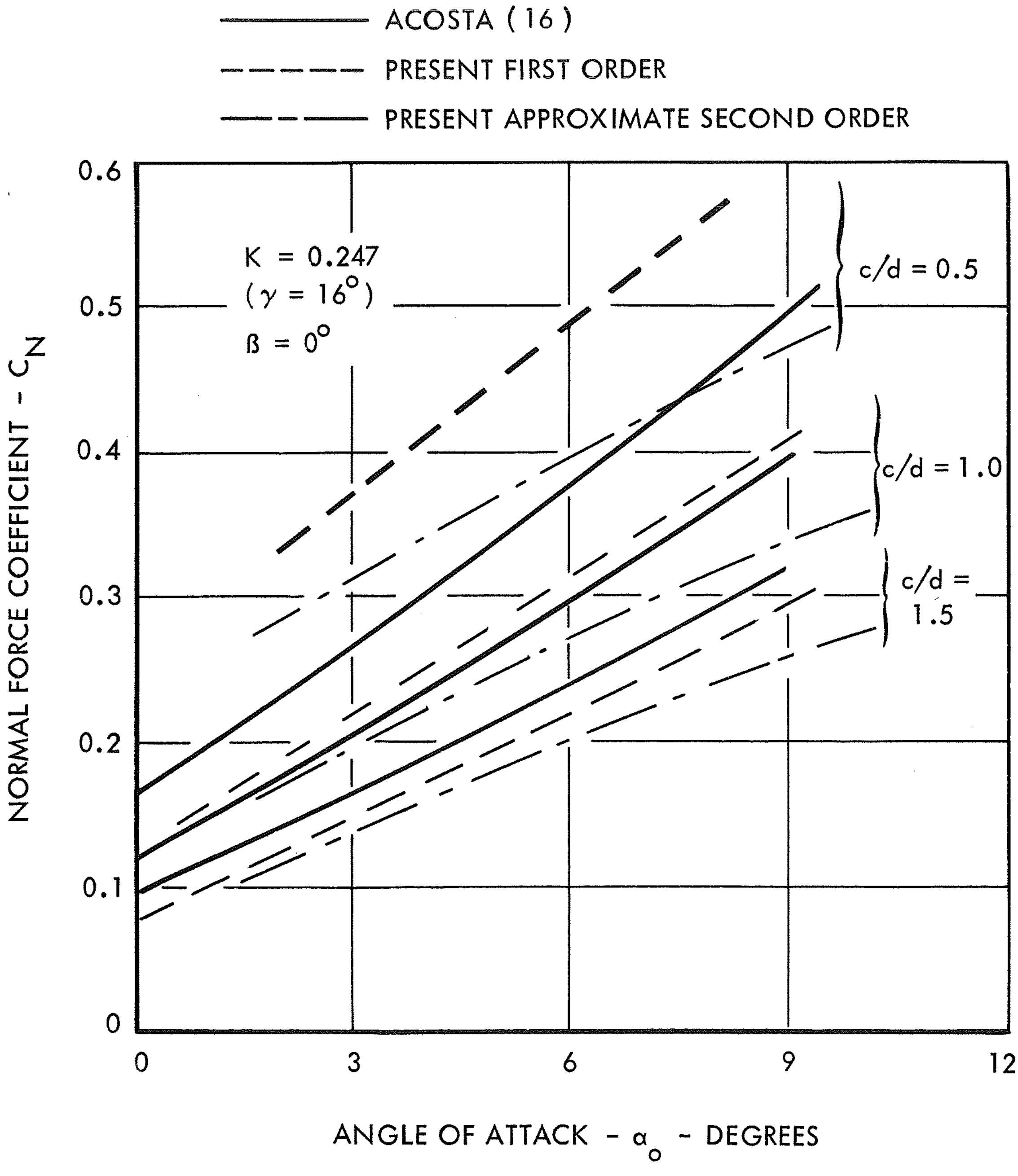

FIGURE 12 - COMPARISON OF ACOSTA'S (16) RESULTS TO THE PRESENT CALCULATIONS FOR CASCADES OF FULLY CAVITATING CIRCULAR ARC HYDROFOILS WITH A STAGGER ANGLE OF 0°

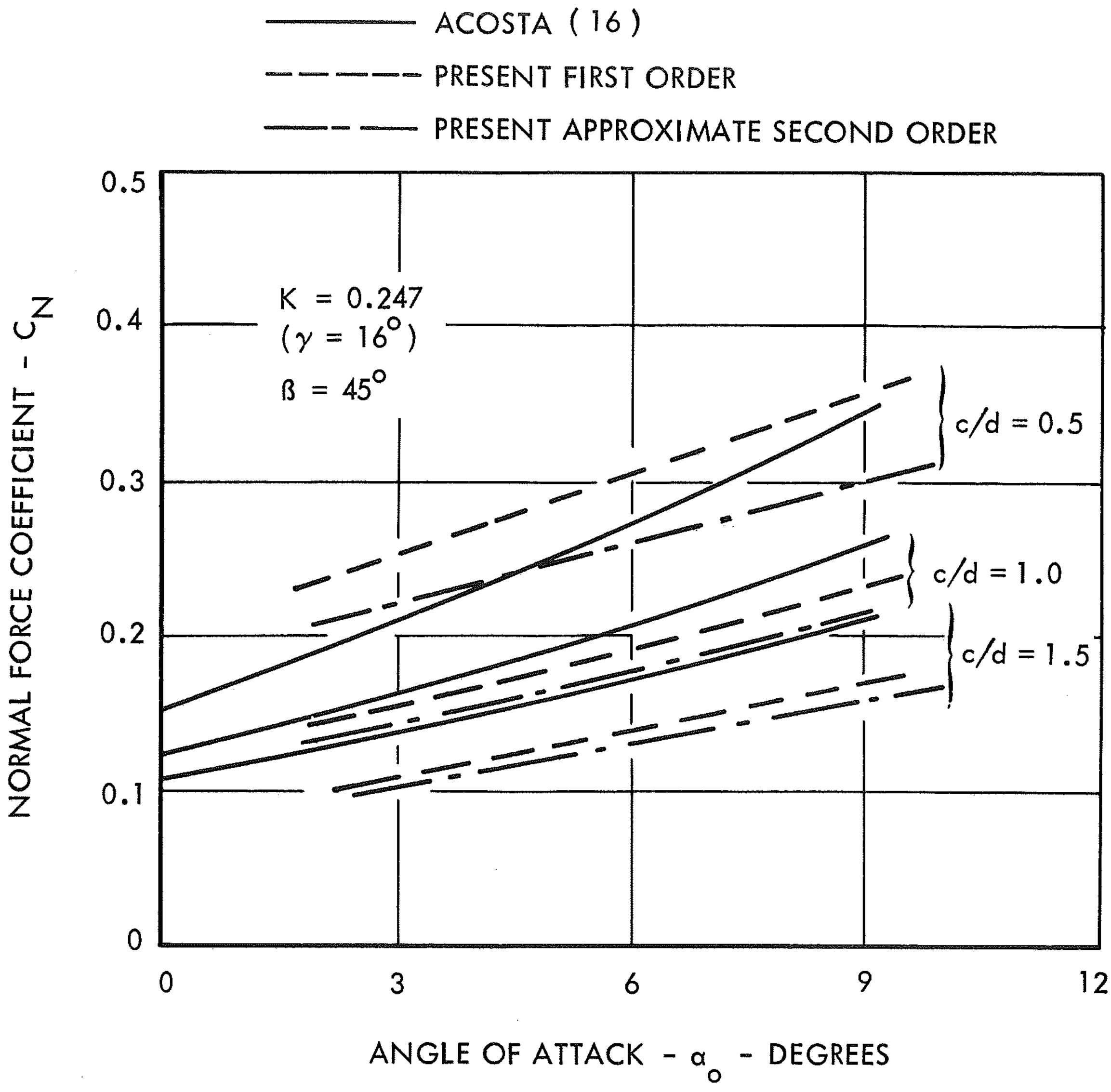

FIGURE 13 - COMPARISON OF ACOSTA'S (16) RESULTS TO THE PRESENT CALCULATIONS FOR CASCADES OF FULLY CAVITATING CIRCULAR ARC HYDROFOILS WITH A STAGGER ANGLE OF 45°

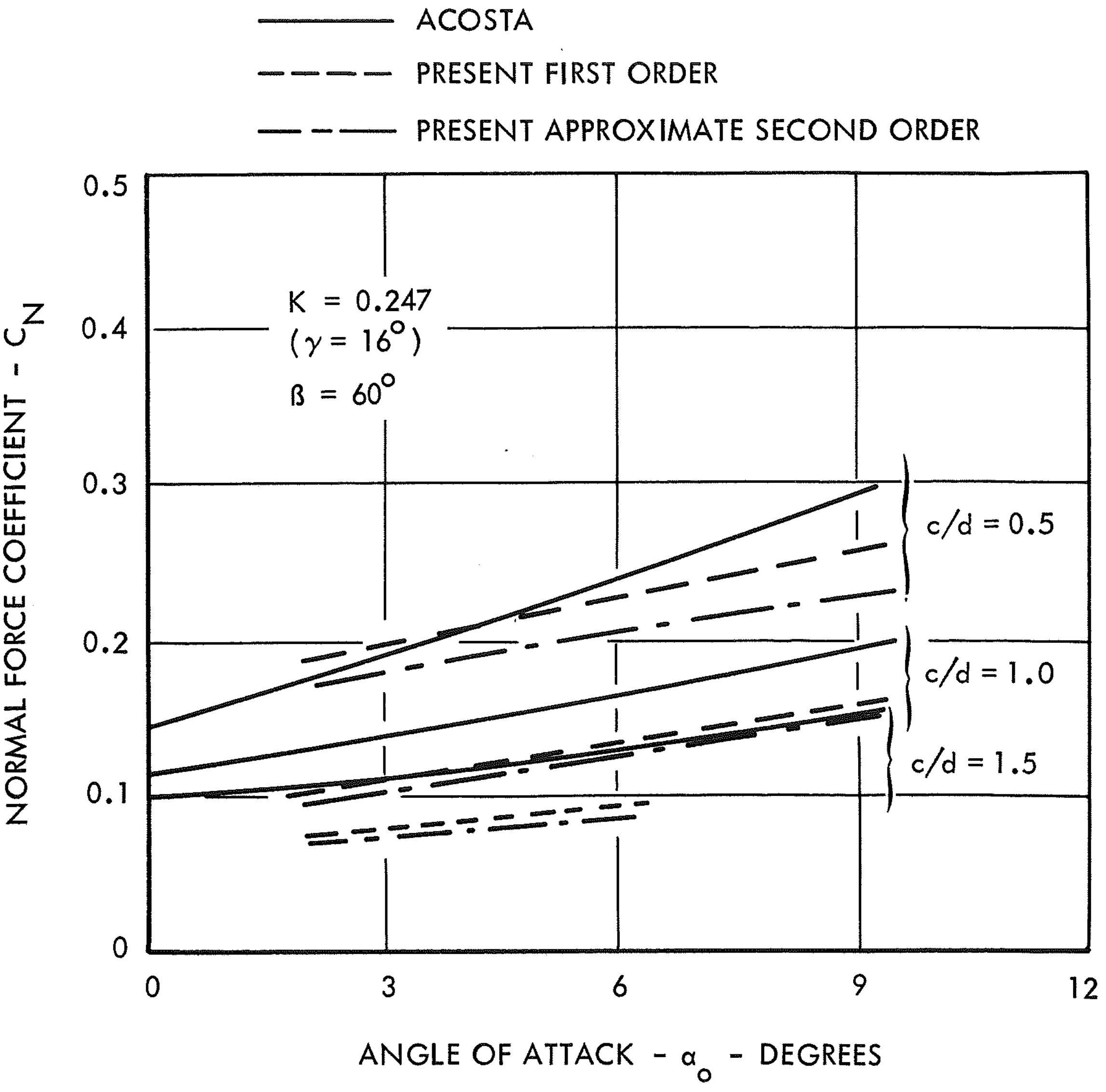

FIGURE 14 - COMPARISON OF ACOSTA'S (16) RESULTS TO THE PRESENT CALCULATIONS FOR CASCADES OF FULLY CAVITATING CIRCULAR ARC HYDROFOILS WITH A STAGGER ANGLE OF 60°

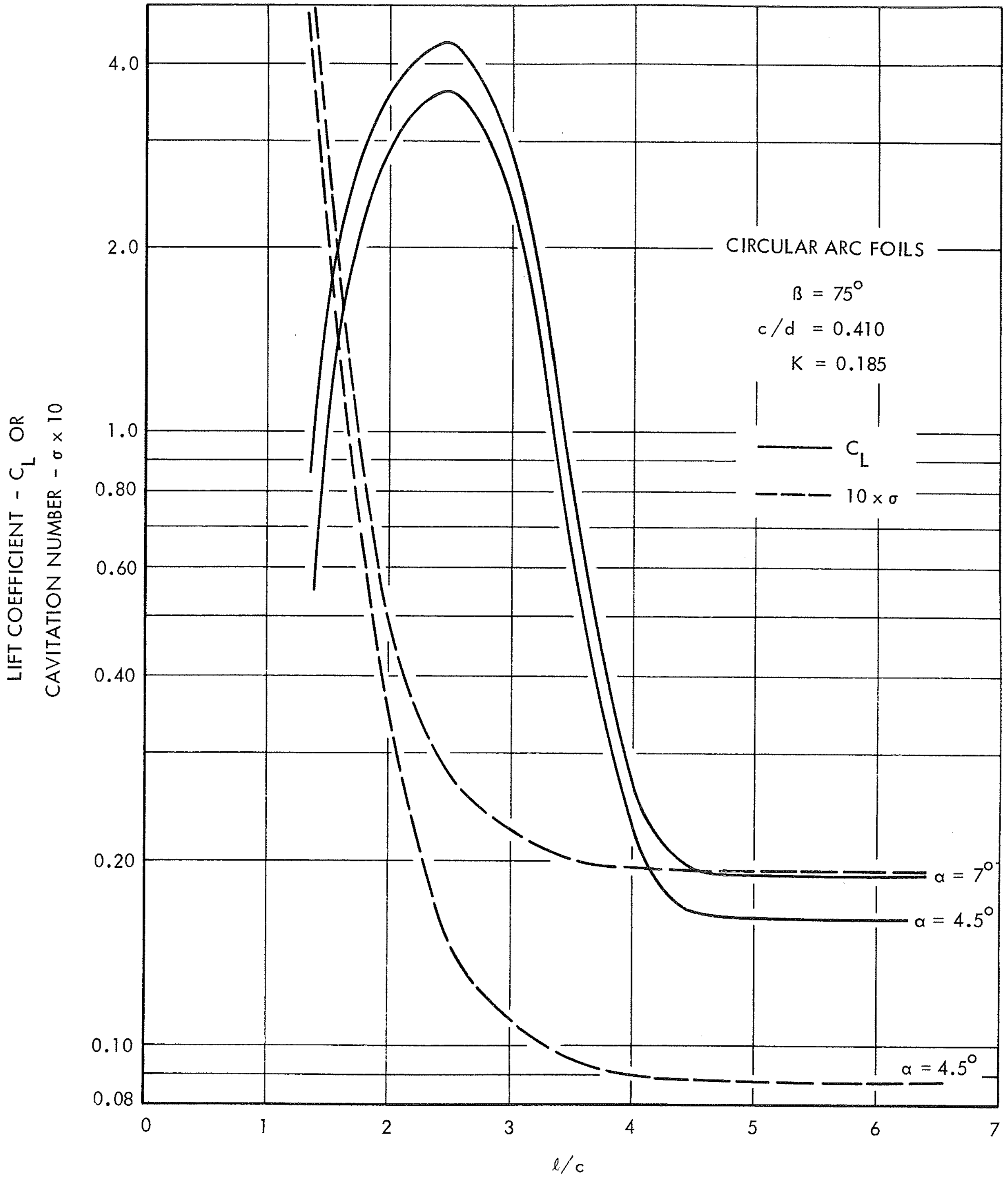

FIGURE 15 - LIFT COEFFICIENT AND CAVITATION NUMBER AS A FUNCTION OF CAVITY LENGTH FOR A CIRCULAR ARC CASCADE

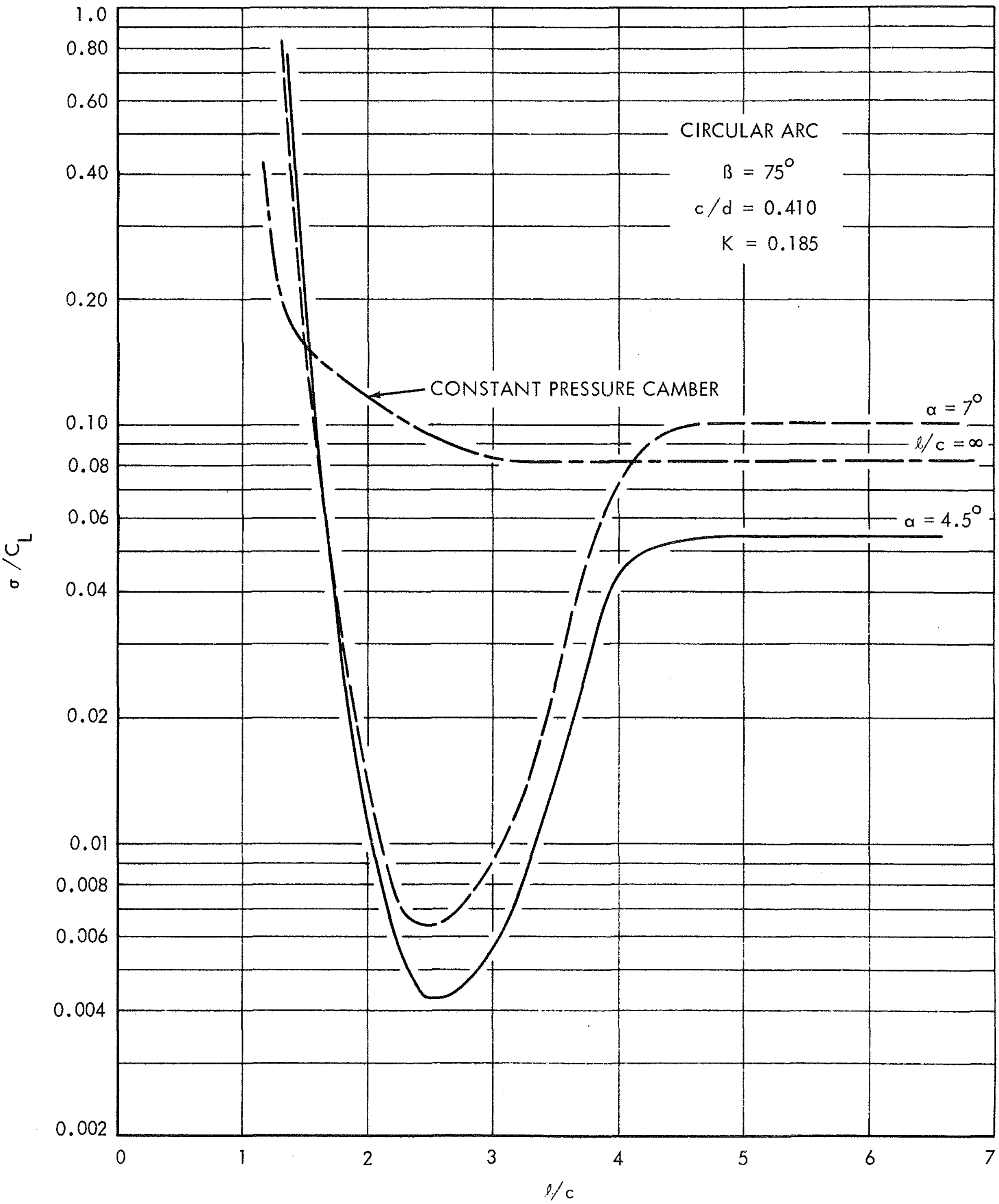

FIGURE 16 - COMPARISON OF CIRCULAR ARC CASCADE TO CONSTANT PRESSURE CAMBER CASCADE OF YIM (2) WITH CAVITY LENGTH VARIABLE

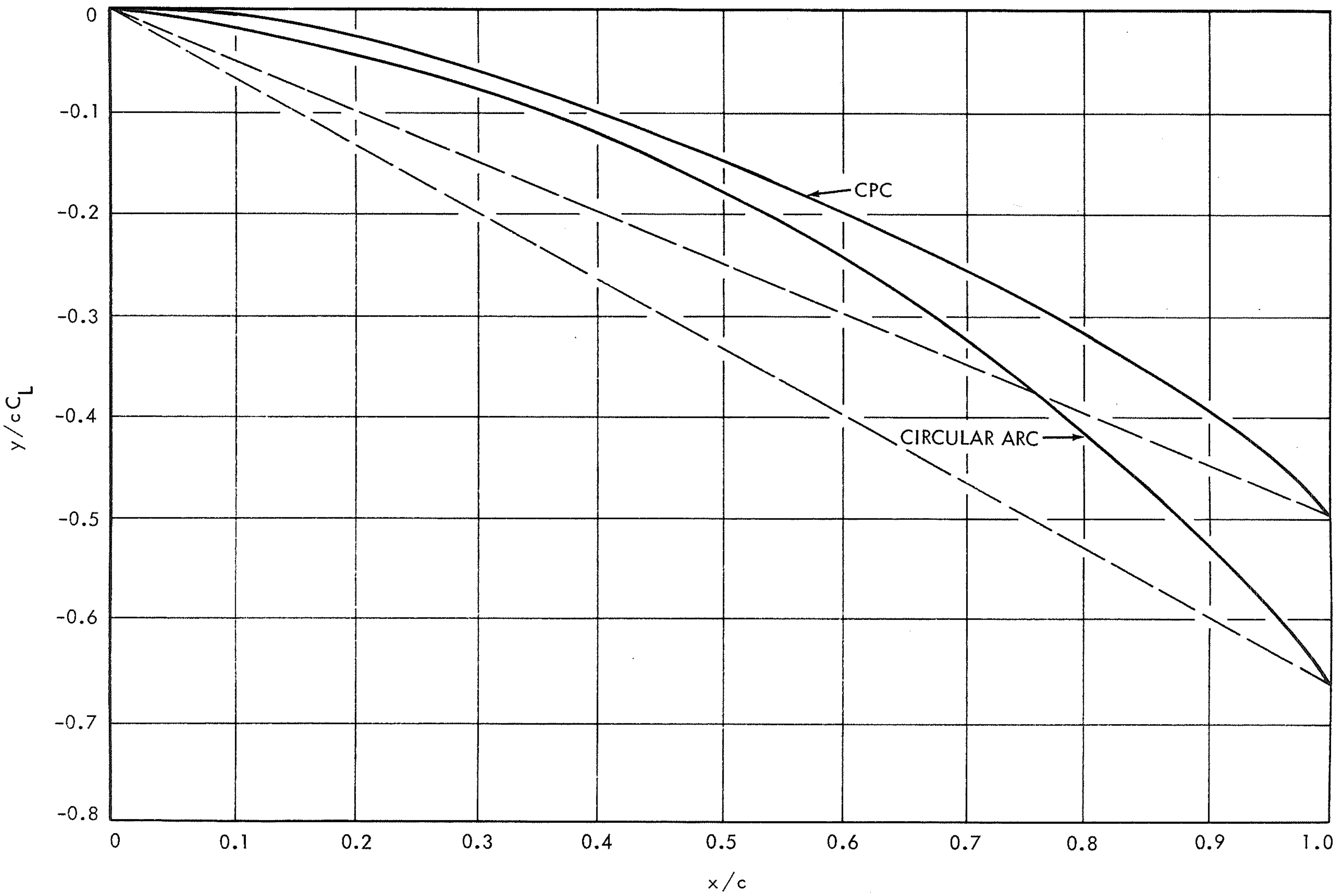

FIGURE 17 - COMPARISON OF FOIL SHAPES FOR CIRCULAR ARC AND CONSTANT PRESSURE CAMBER (AFTER YIM (2)) FOILS IN CASCADE WITH $\beta = 75^\circ$, $c/d = 0.410$, $\sigma / C_L = 0.082$

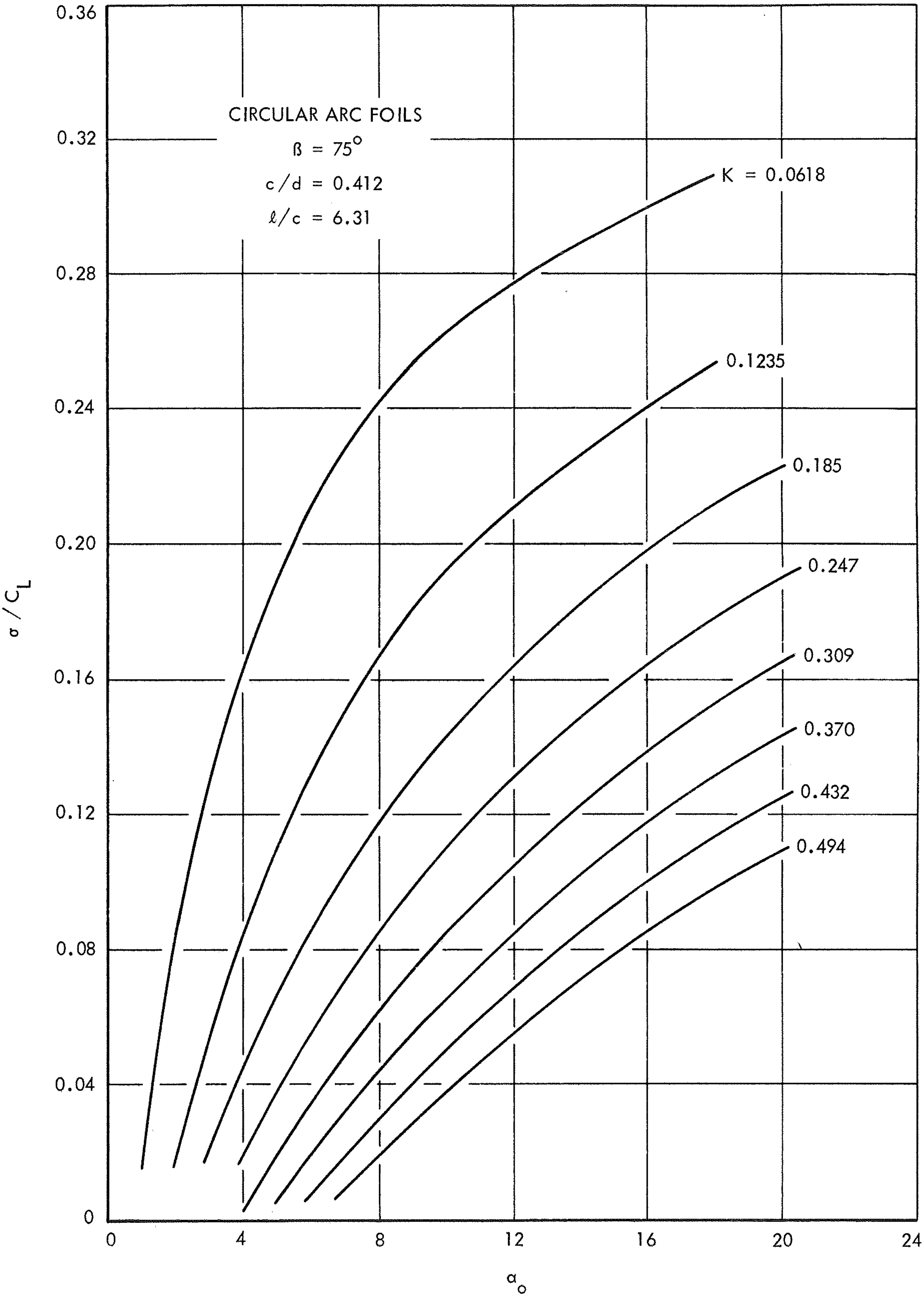

FIGURE 18 - INFLUENCE OF CAMBER INDEX AND ANGLE OF ATTACK ON σ/C_L FOR A SERIES OF CIRCULAR ARC FOILS IN CASCADE

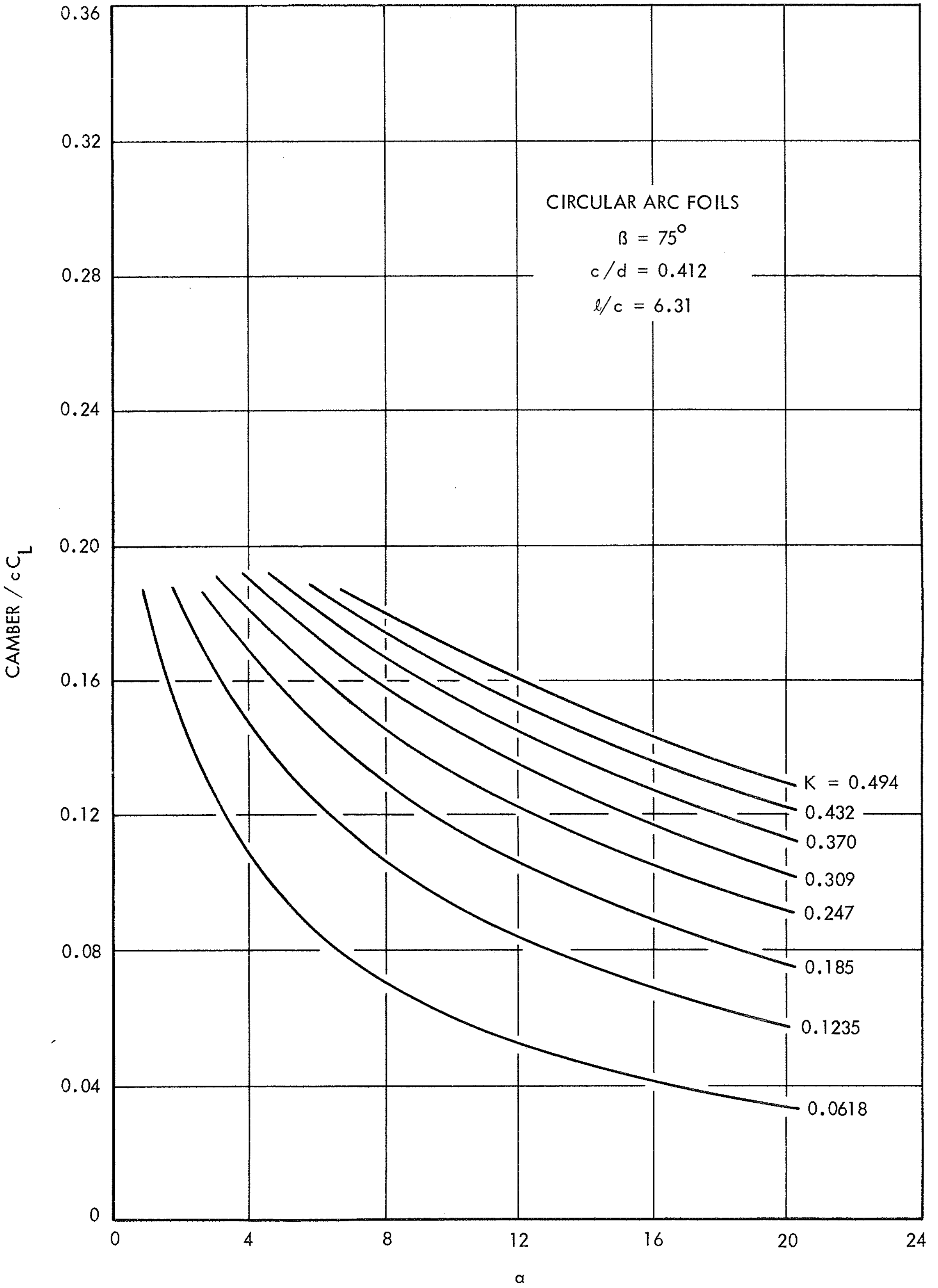

FIGURE 19 - INFLUENCE OF CAMBER INDEX AND ANGLE OF ATTACK ON CAMBER/c C_L FOR A SERIES OF CIRCULAR ARC FOILS IN CASCADE

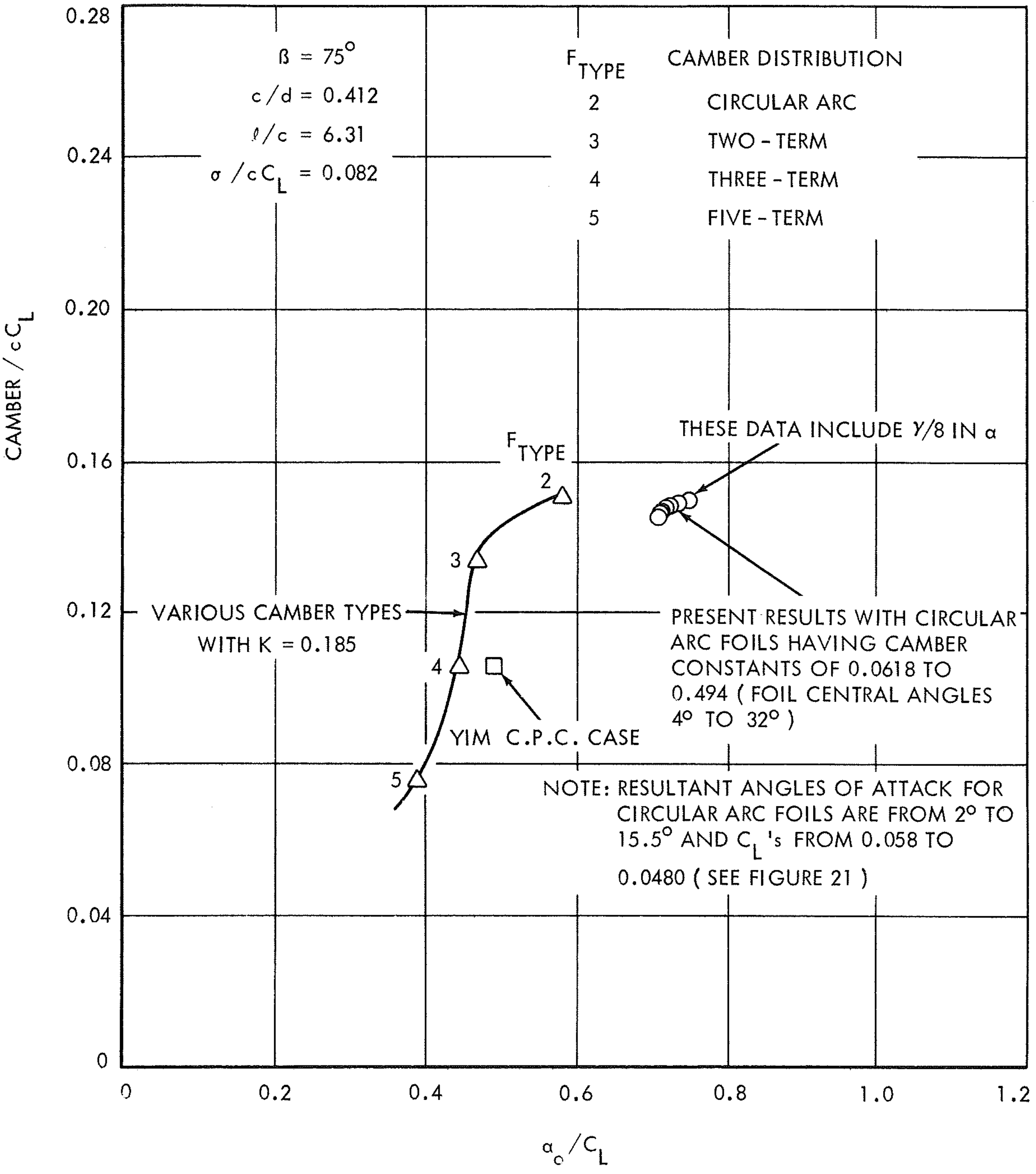

FIGURE 20 - RELATION BETWEEN CAMBER/cC_L AND α_o/C_L FOR CONSTANT σ/C_L = 0.082 FOR SUPERCAVITATING CASCADES WITH VARIOUS FOIL SHAPES AND CAMBER INDICES

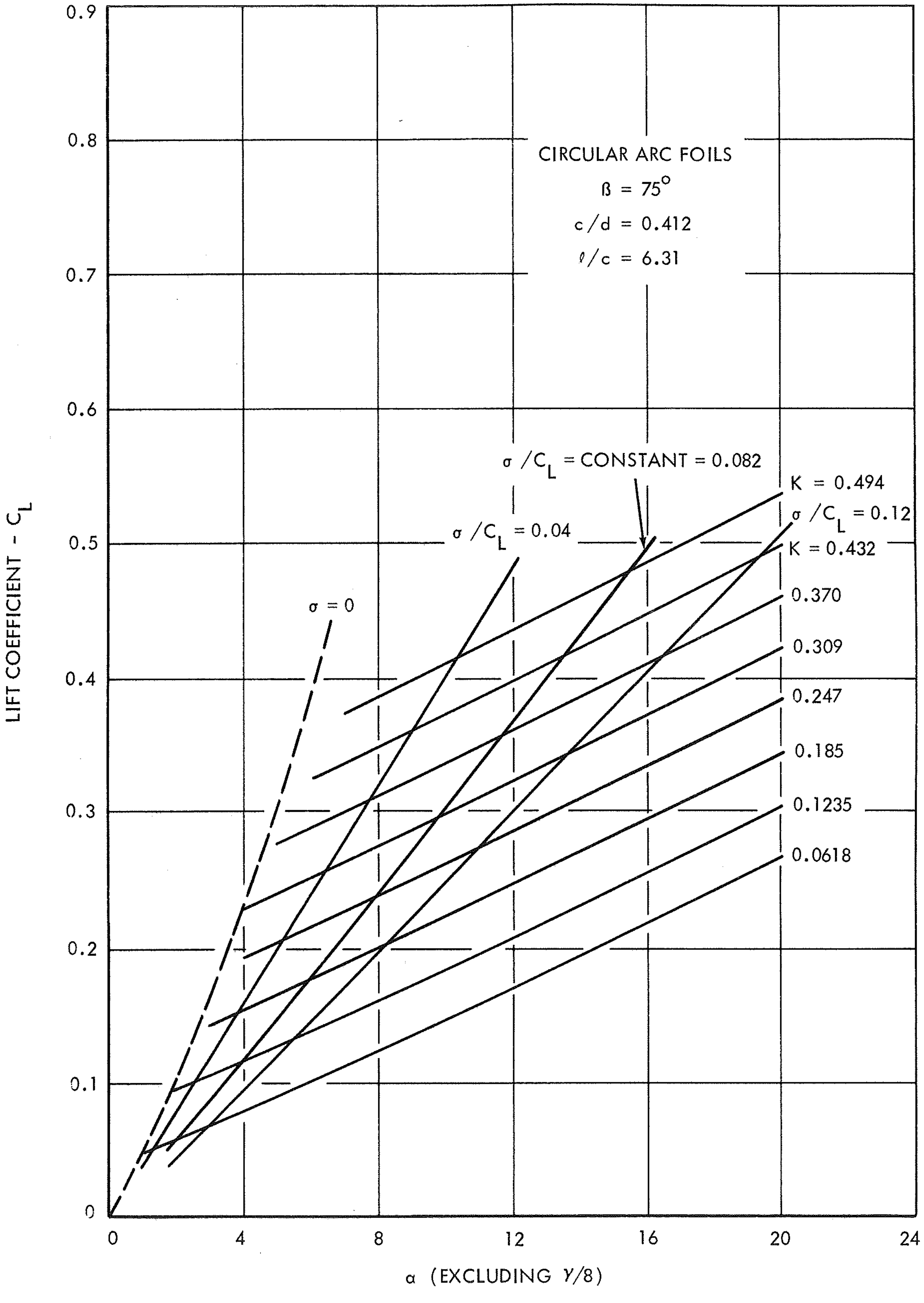

FIGURE 21 - INFLUENCE OF CAMBER COEFFICIENT AND ANGLE OF ATTACK ON LIFT COEFFICIENT AND σ/C_L FOR VARIOUS CIRCULAR ARC FOILS IN CASCADE

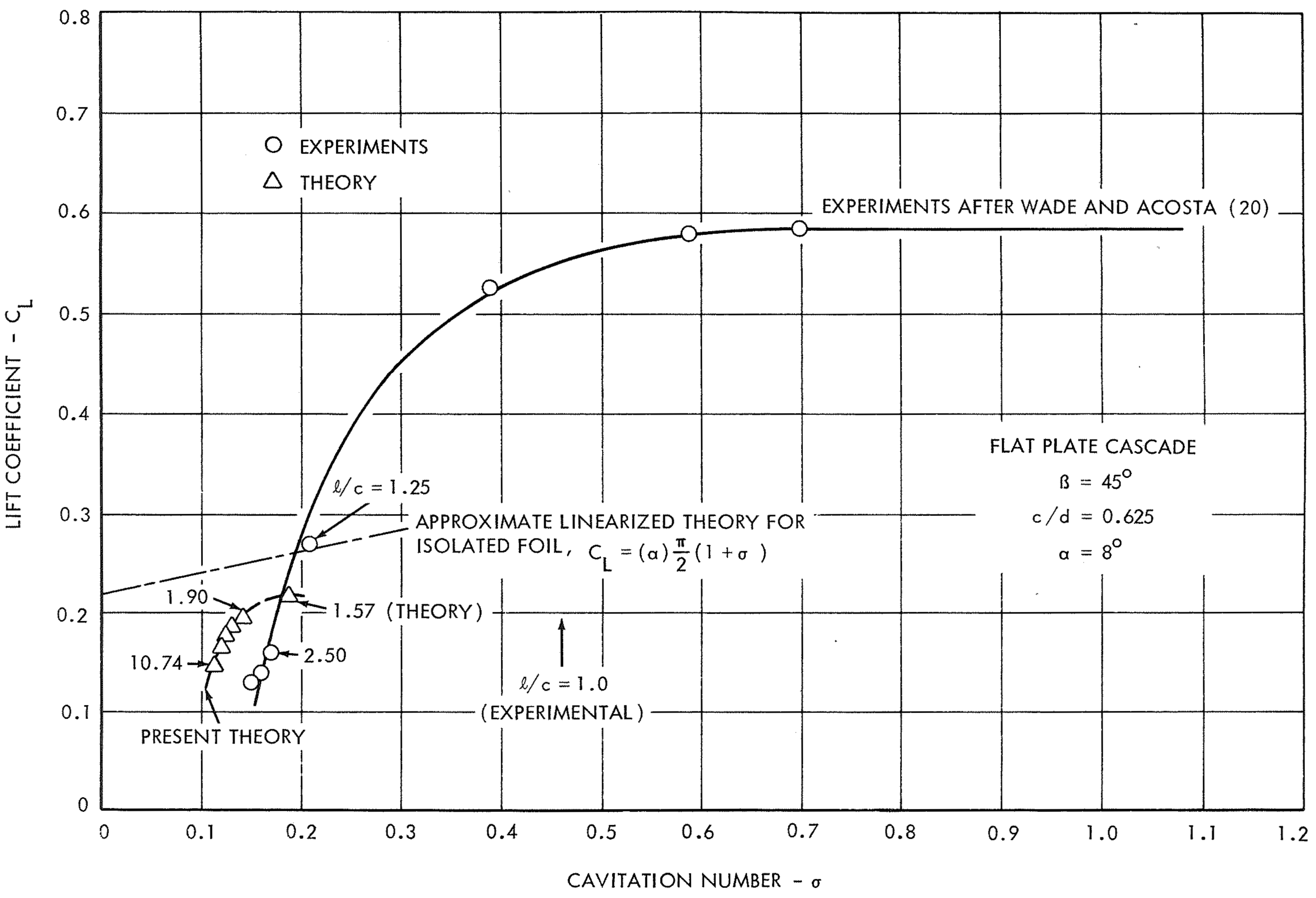

FIGURE 22 - COMPARISON OF PRESENT CALCULATIONS TO THE EXPERIMENTS OF WADE AND ACOSTA (20)

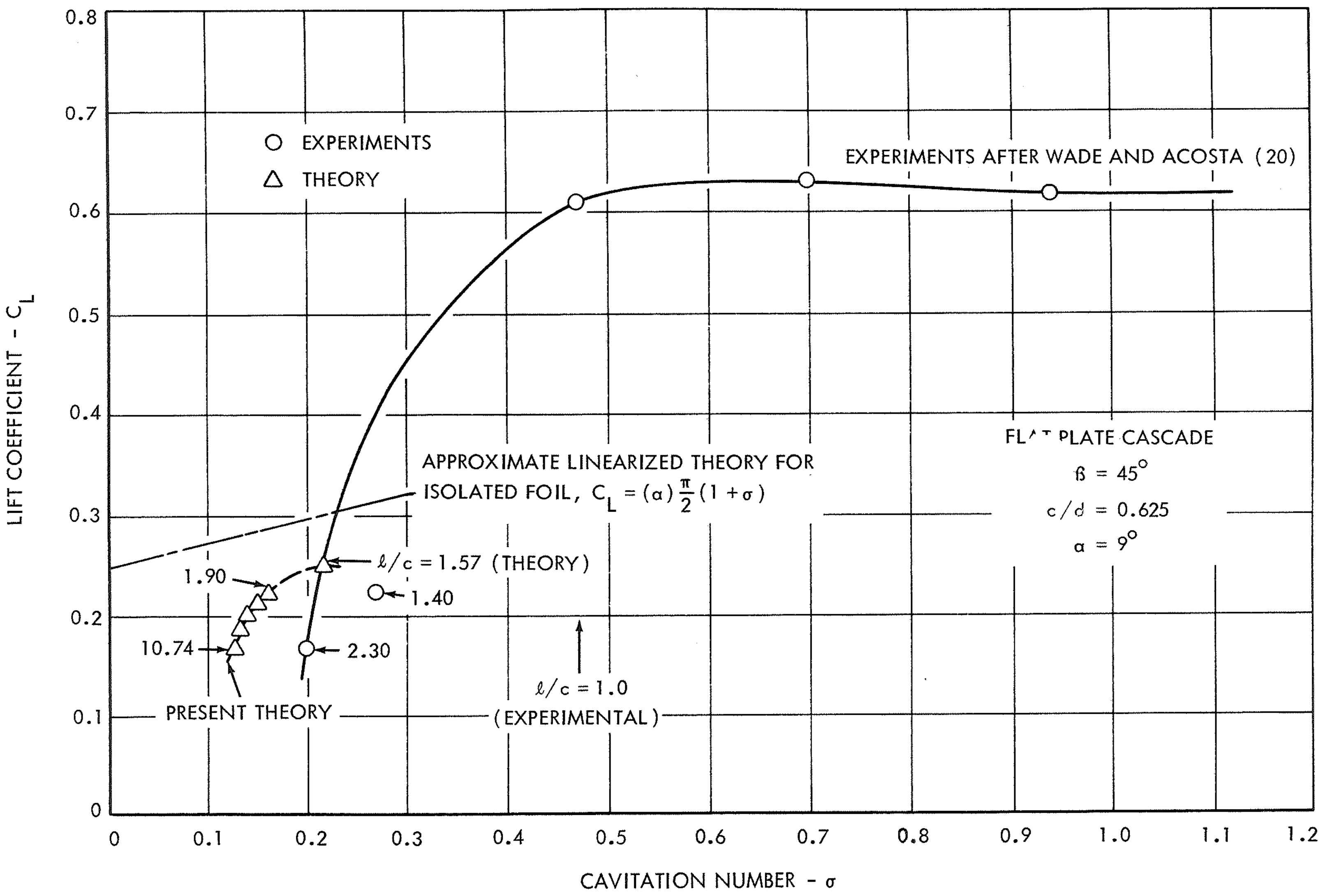

FIGURE 23 - COMPARISON OF PRESENT CALCULATIONS TO THE EXPERIMENTS OF WADE AND ACOSTA (20)

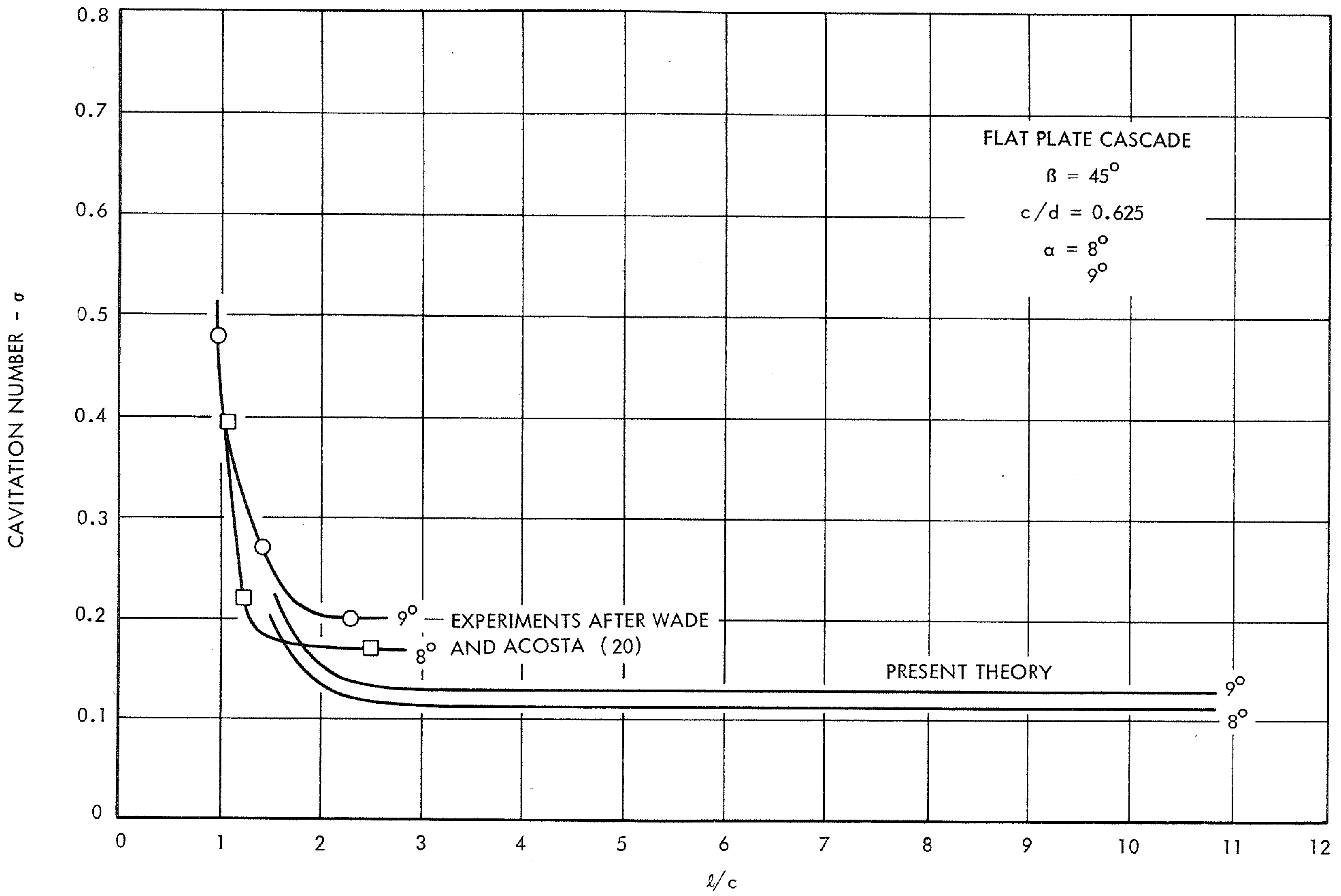

FIGURE 24 - COMPARISON OF PRESENT CALCULATIONS TO THE EXPERIMENTS OF WADE AND ACOSTA (20)

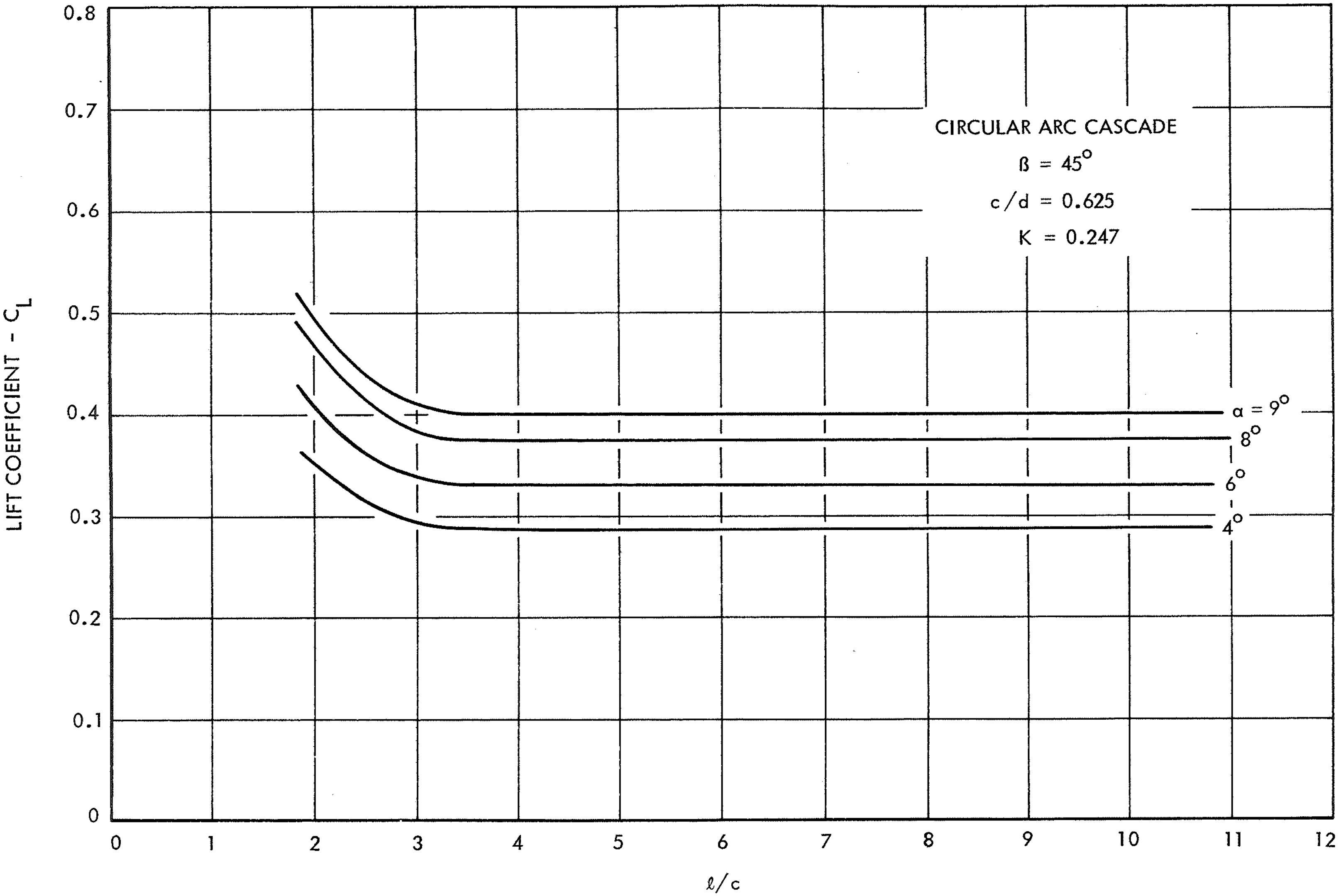

FIGURE 25 - INFLUENCE OF CAVITY LENGTH ON LIFT COEFFICIENT FOR A CIRCULAR ARC CASCADE

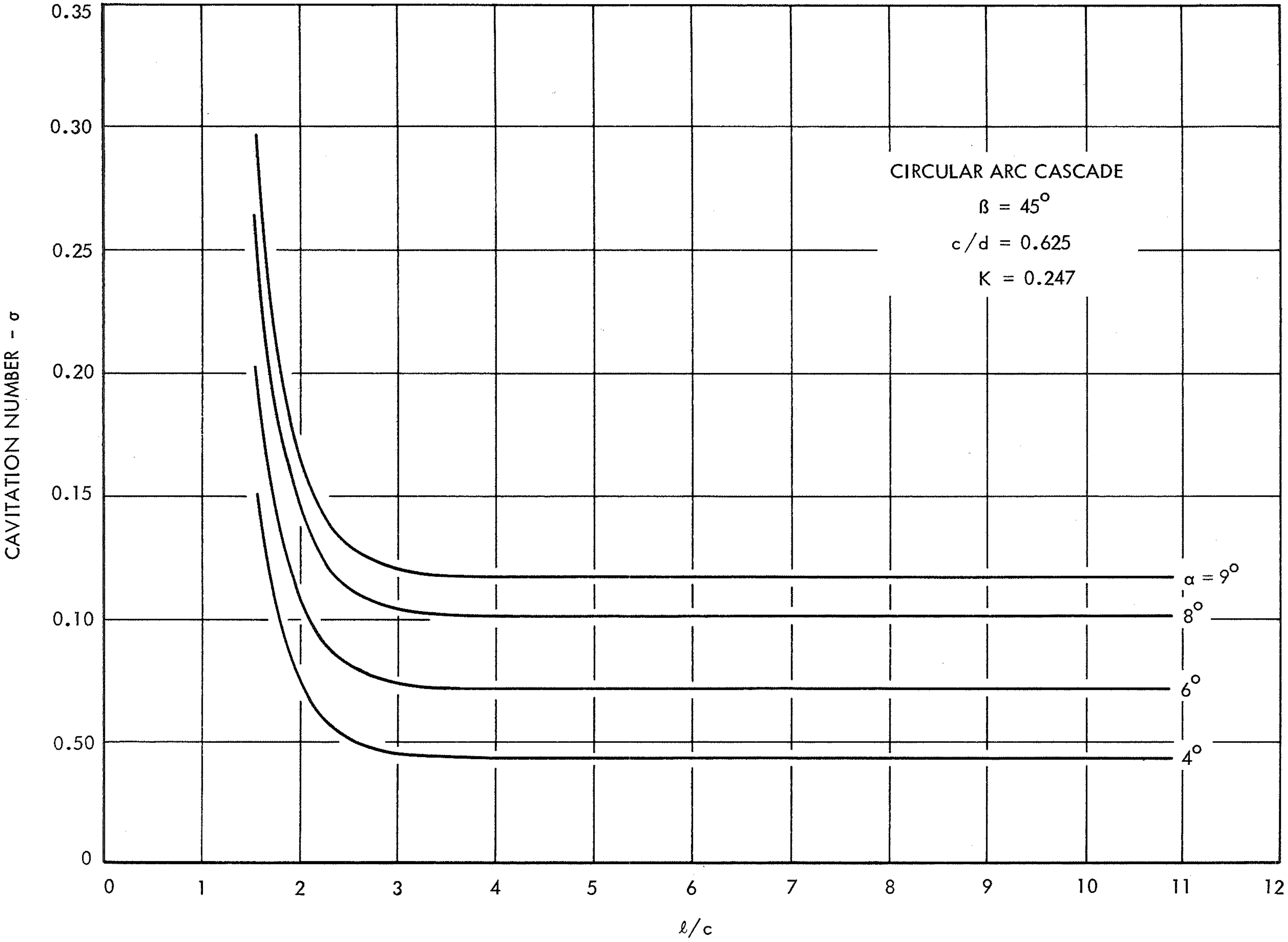

FIGURE 26 - INFLUENCE OF CAVITATION NUMBER ON CAVITY LENGTH FOR A CIRCULAR ARC CASCADE

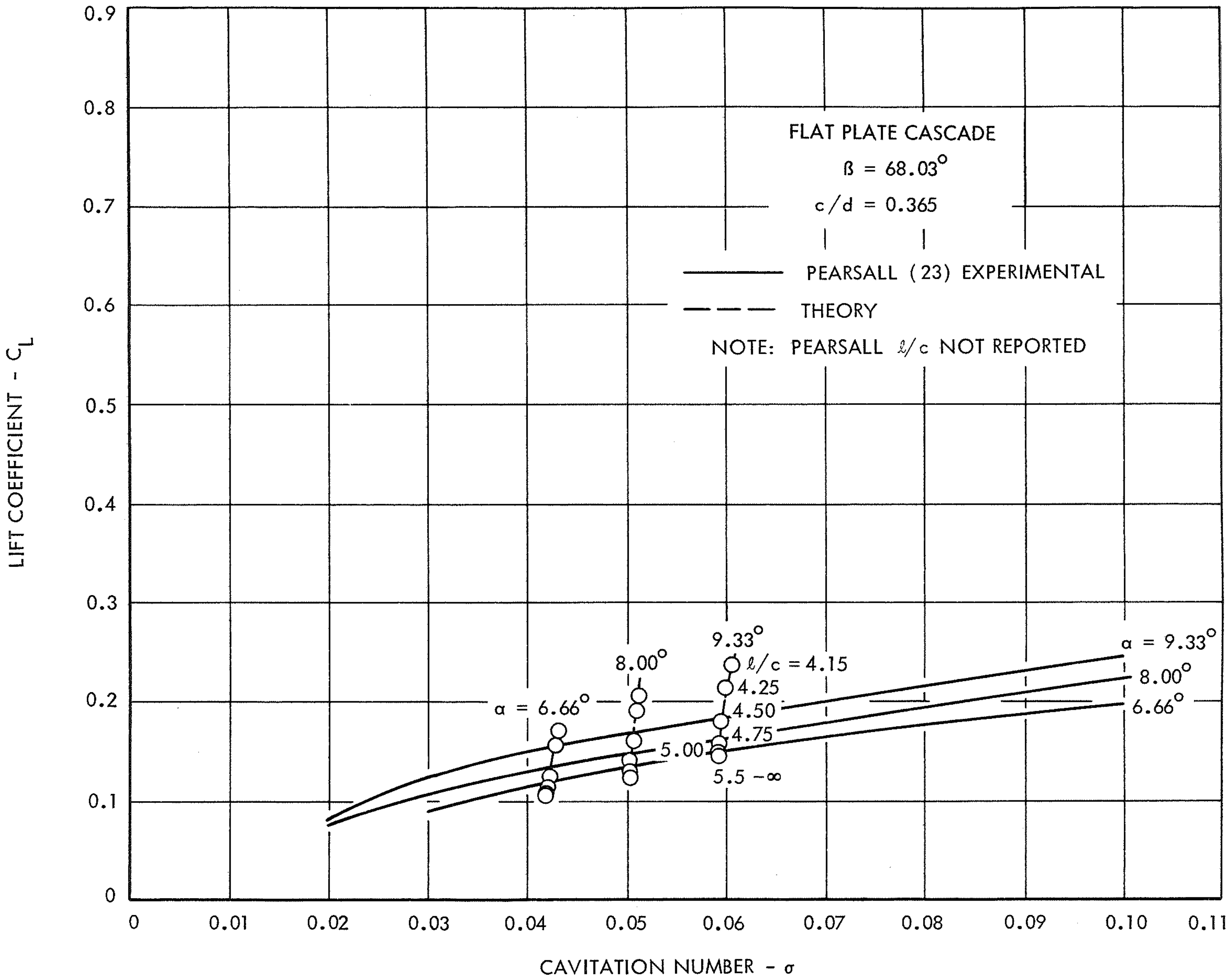

FIGURE 27 - COMPARISON OF PRESENT CALCULATIONS AND EXPERIMENTS OF PEARSALL (23)

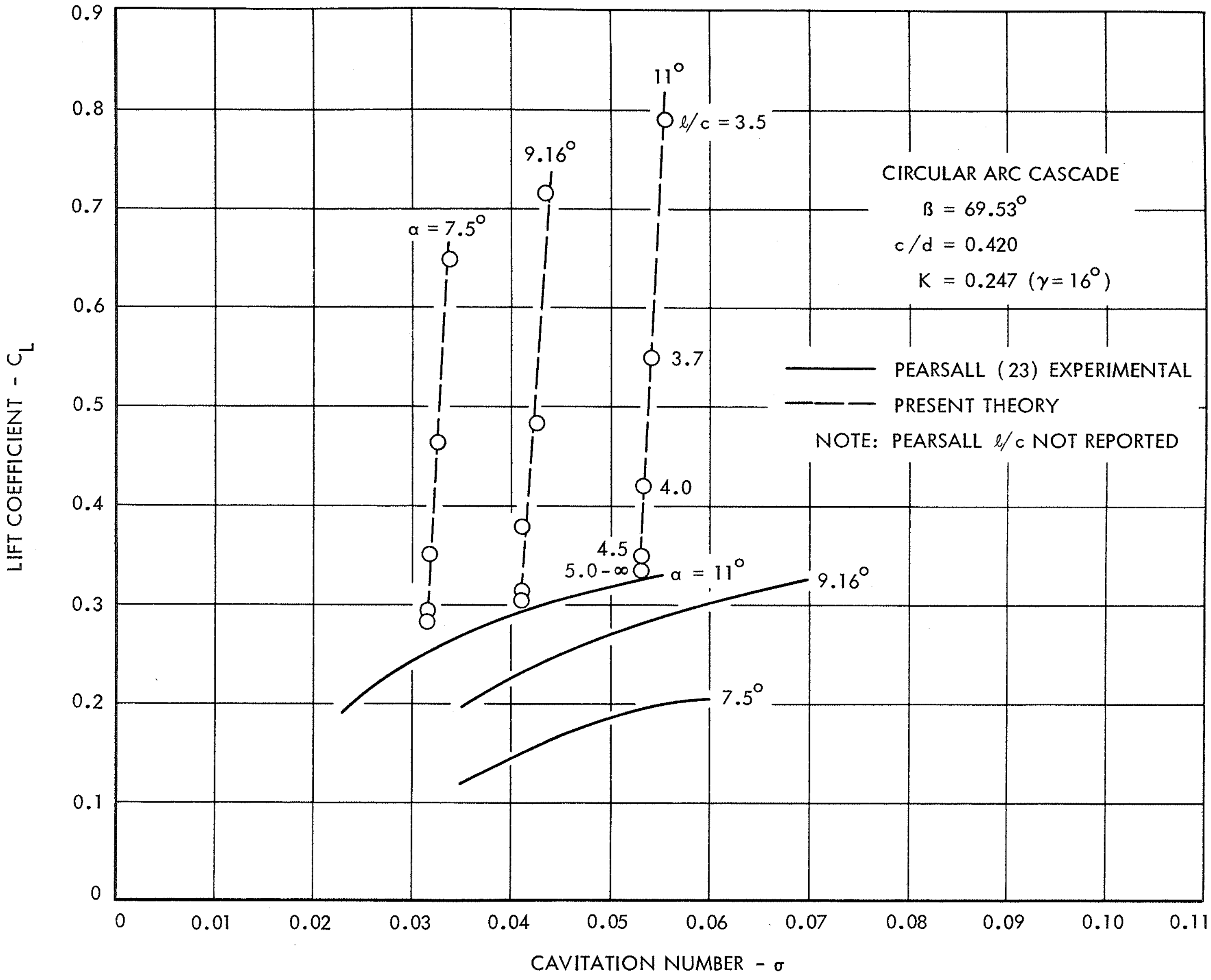

FIGURE 28 - COMPARISON OF PRESENT CALCULATIONS AND EXPERIMENTS OF PEARSALL (23)

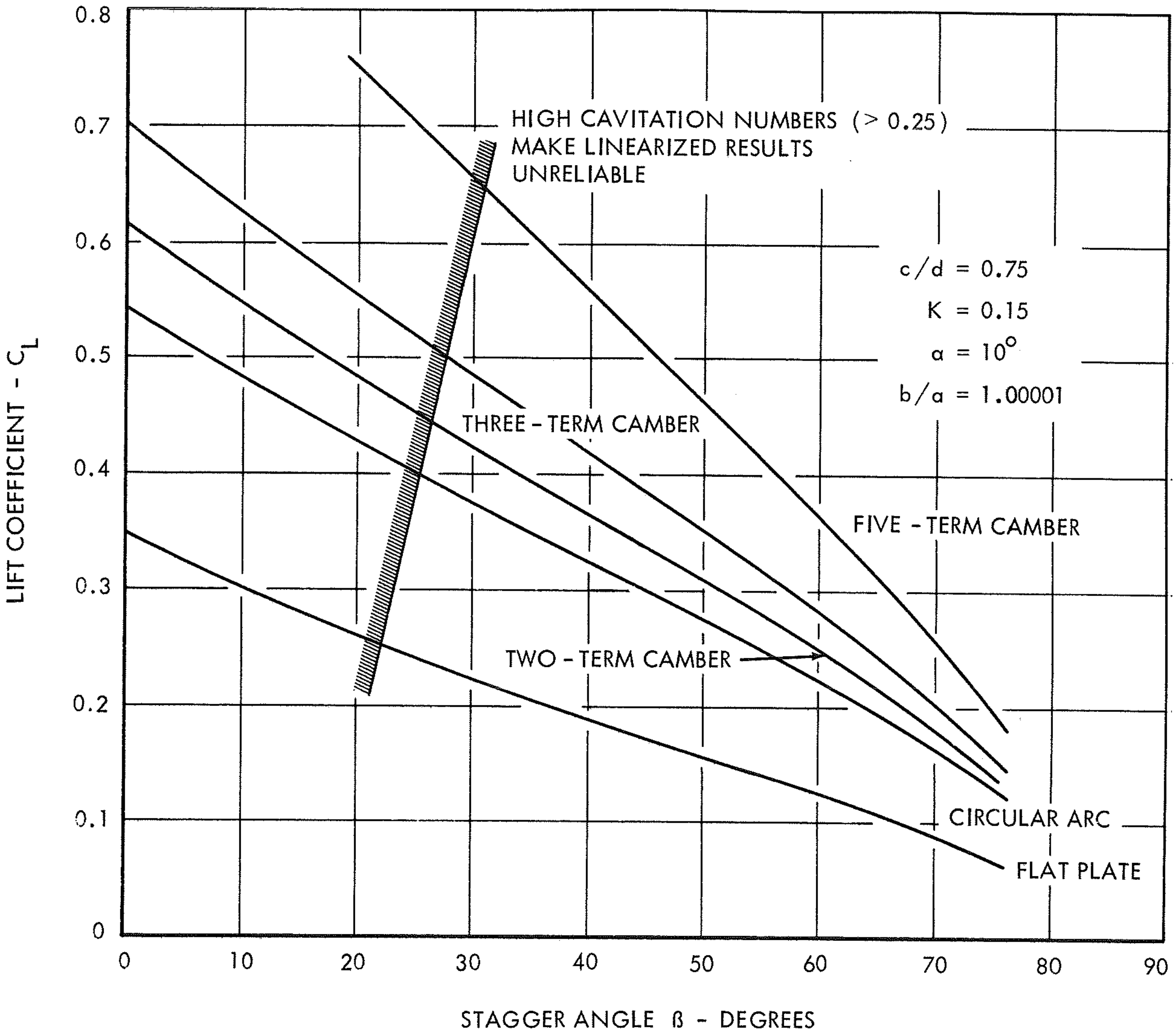

FIGURE 29 - INFLUENCE OF STAGGER ANGLE ON LIFT COEFFICIENT FOR 0.75 SOLIDITY FOR VARIOUS CAMBER TYPES

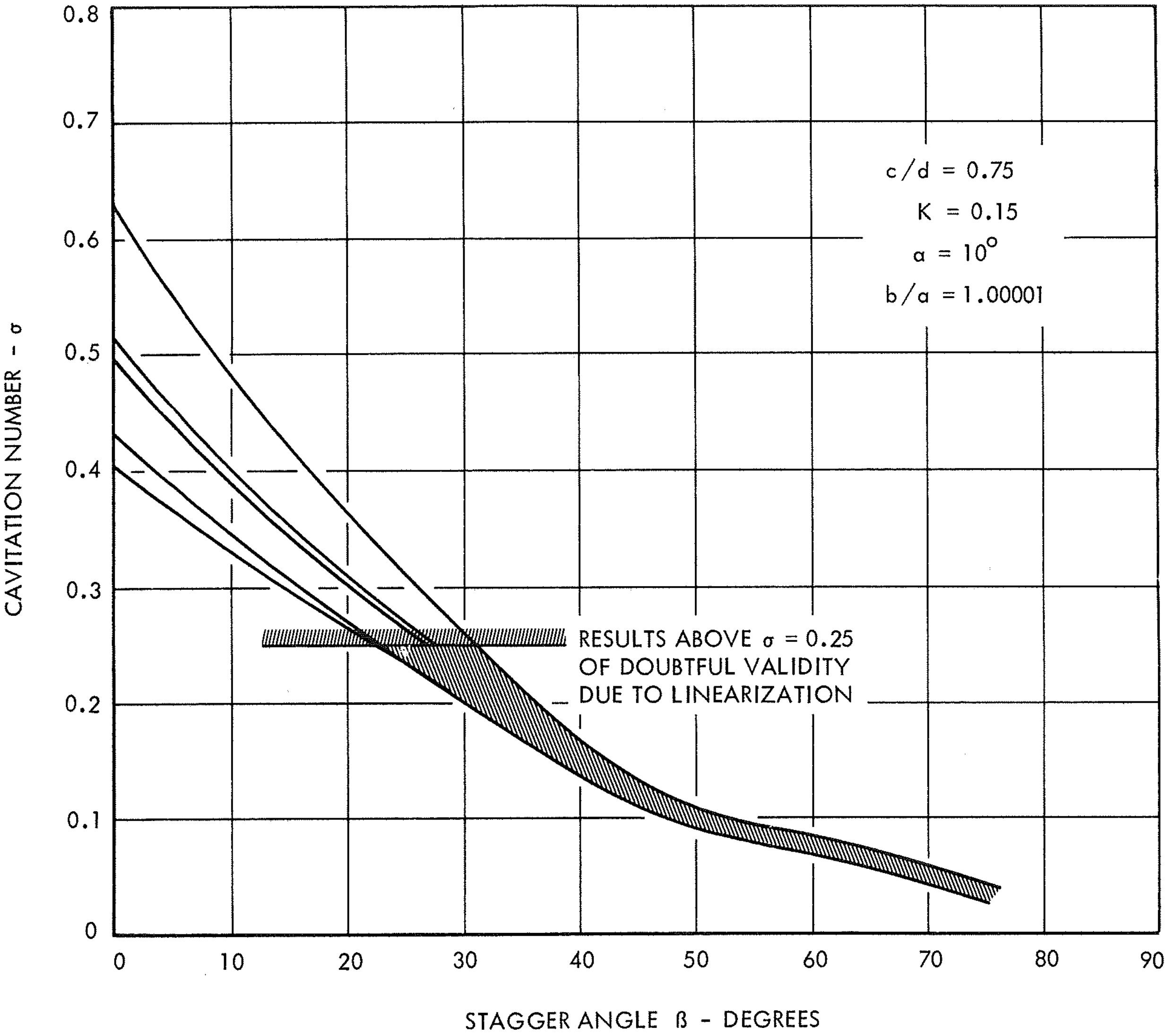

FIGURE 30 - INFLUENCE OF STAGGER ANGLE ON CAVITATION NUMBER FOR 0.75 SOLIDITY FOR VARIOUS CAMBER TYPES

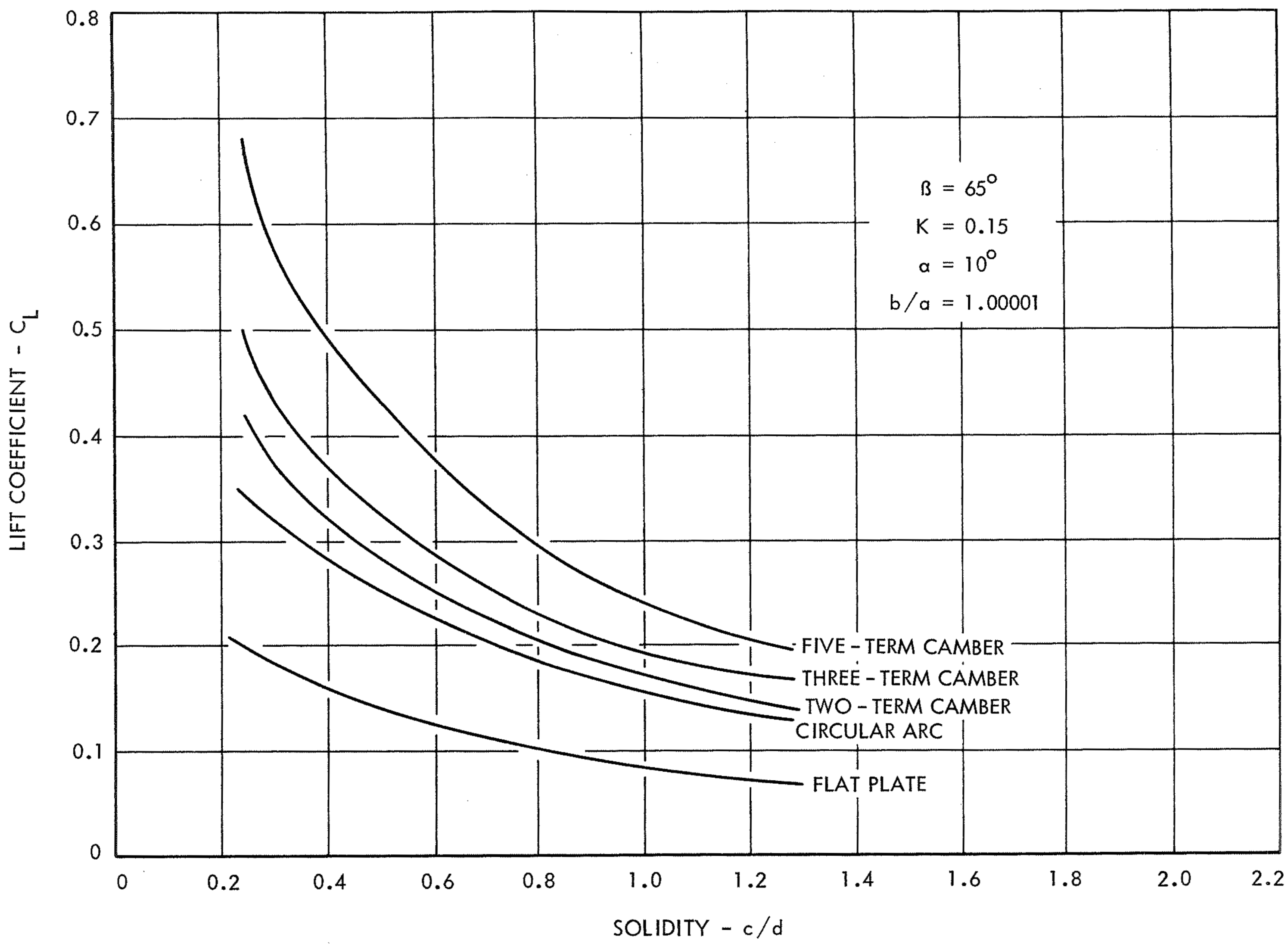

FIGURE 31 - INFLUENCE OF SOLIDITY ON LIFT COEFFICIENT FOR 65° STAGGER ANGLE AND VARIOUS CAMBER TYPES

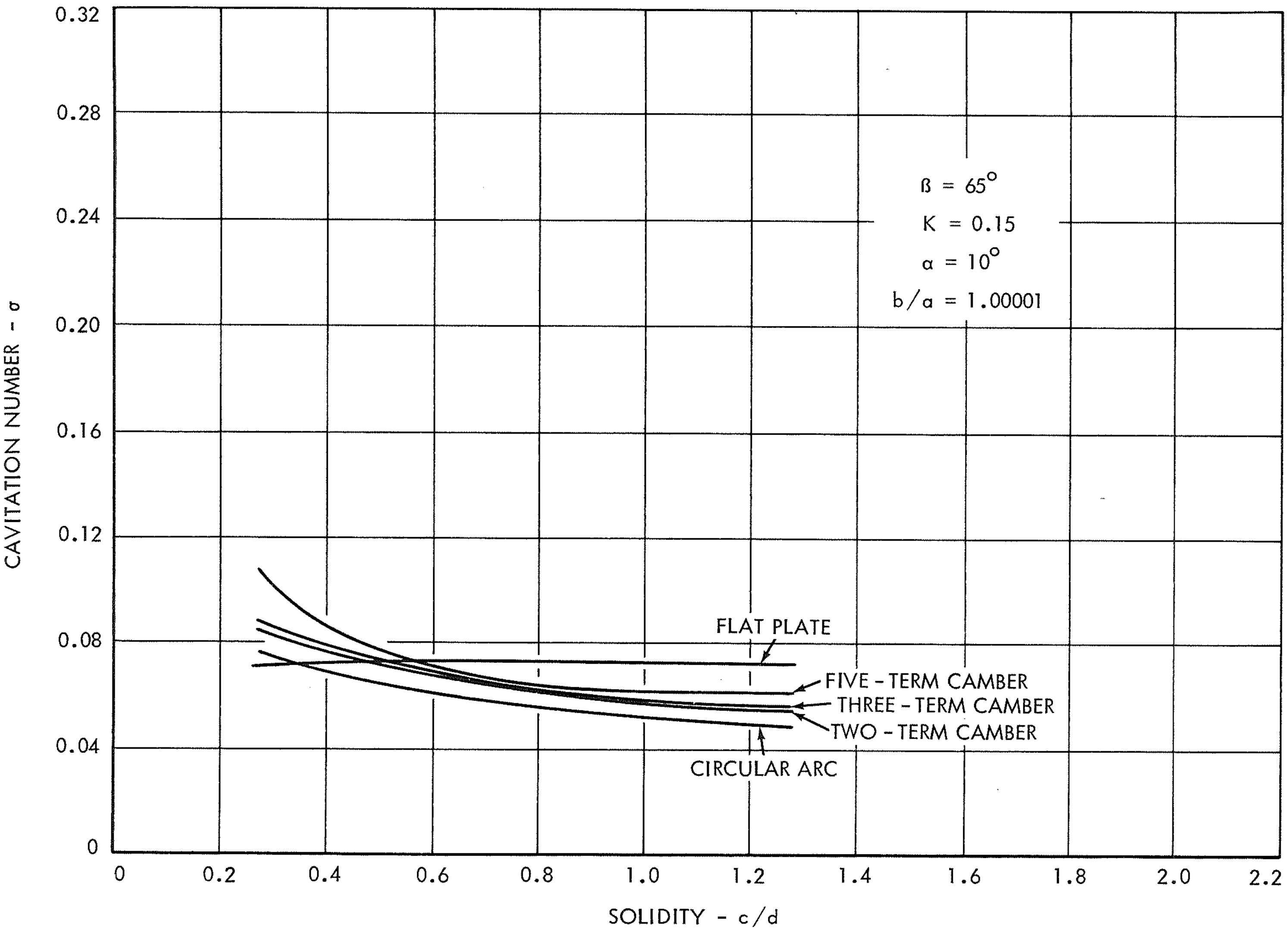

FIGURE 32 - INFLUENCE OF SOLIDITY ON CAVITATION NUMBER FOR 65° STAGGER ANGLE AND VARIOUS CAMBER TYPES

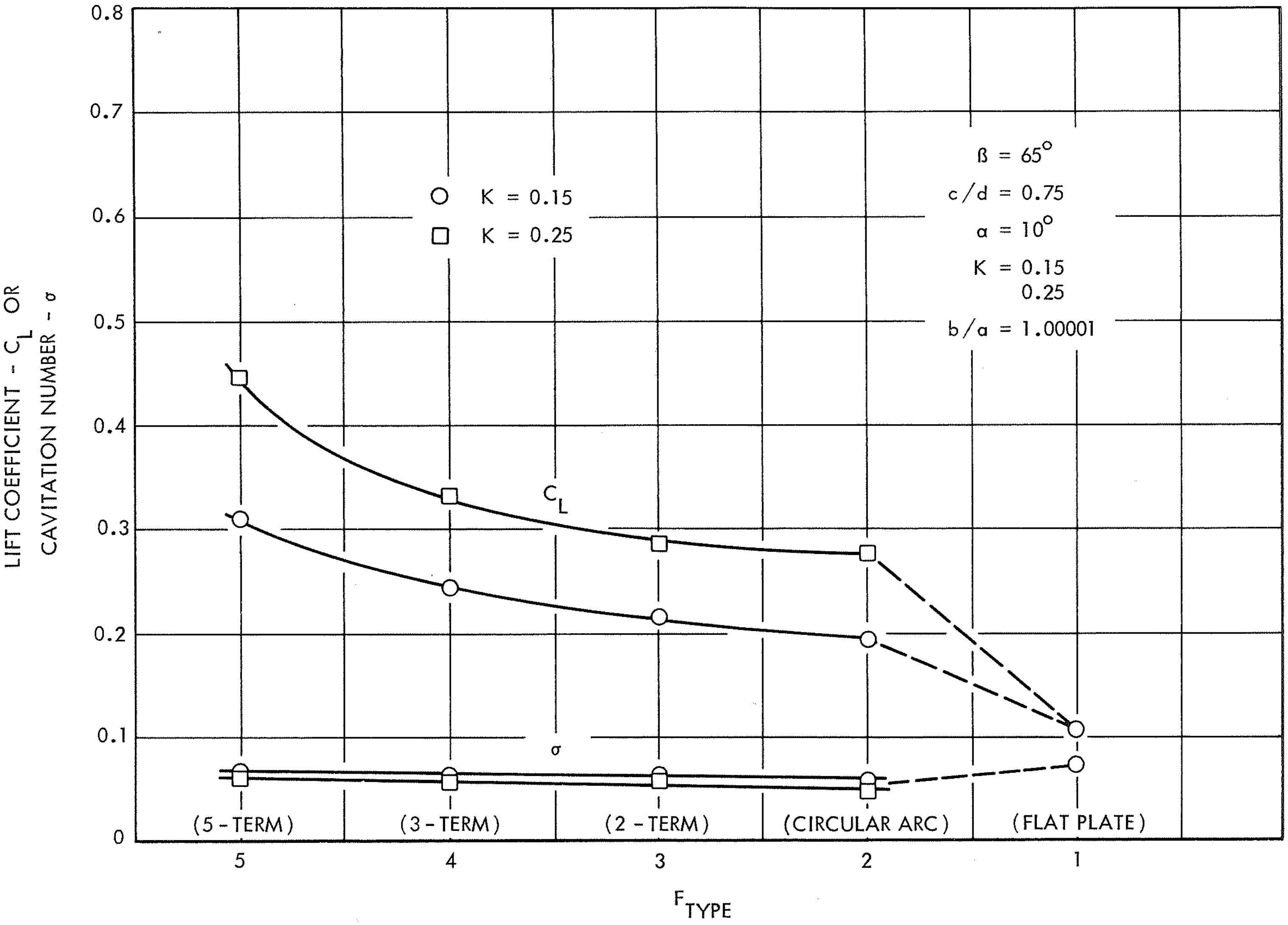

FIGURE 33 - VARIATION OF LIFT COEFFICIENT AND CAVITATION NUMBER WITH CAMBER TYPE AND CAMBER INDEX

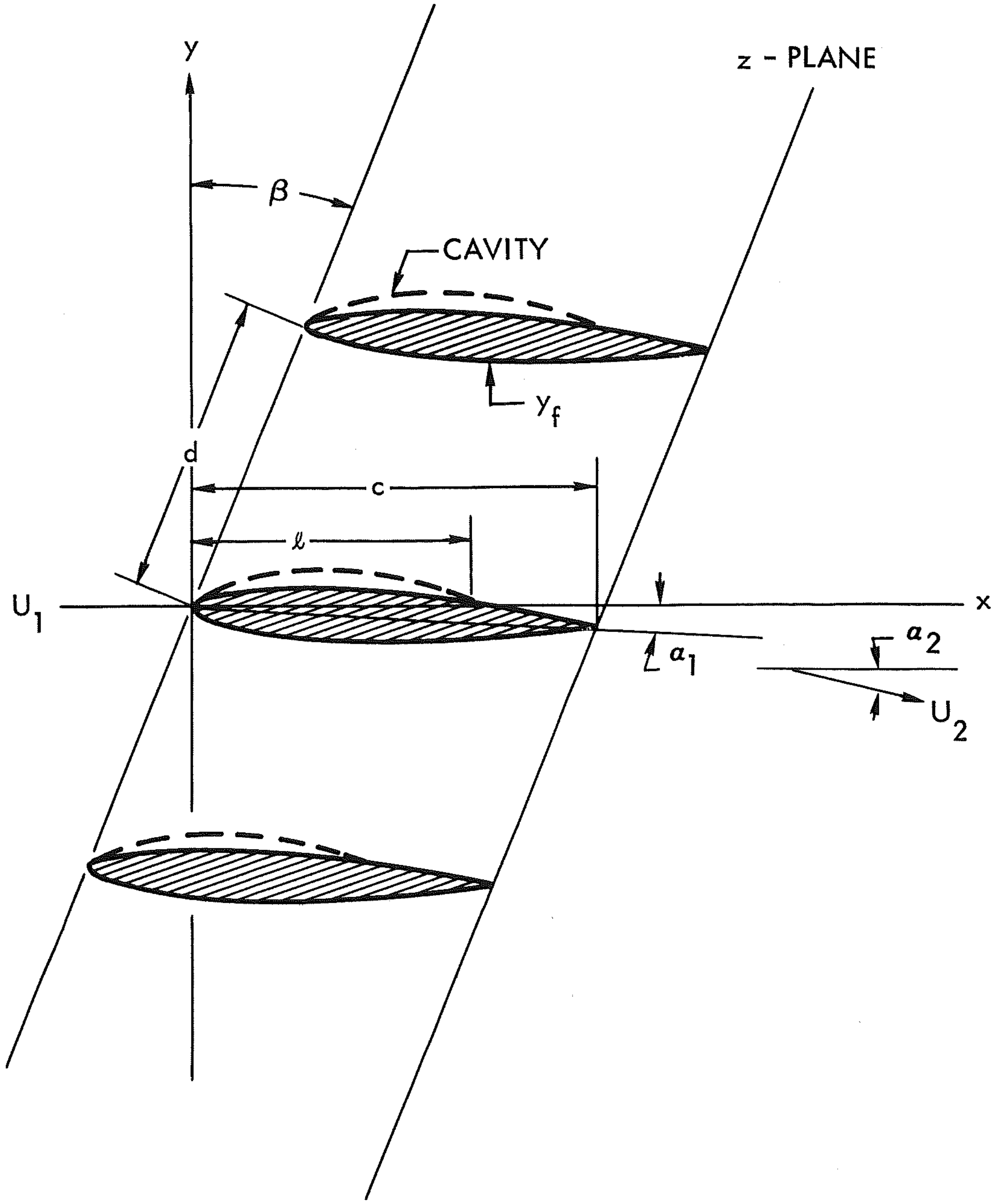

FIGURE 34 - DEFINITION SKETCH FOR A PARTIALLY CAVITATING CASCADE

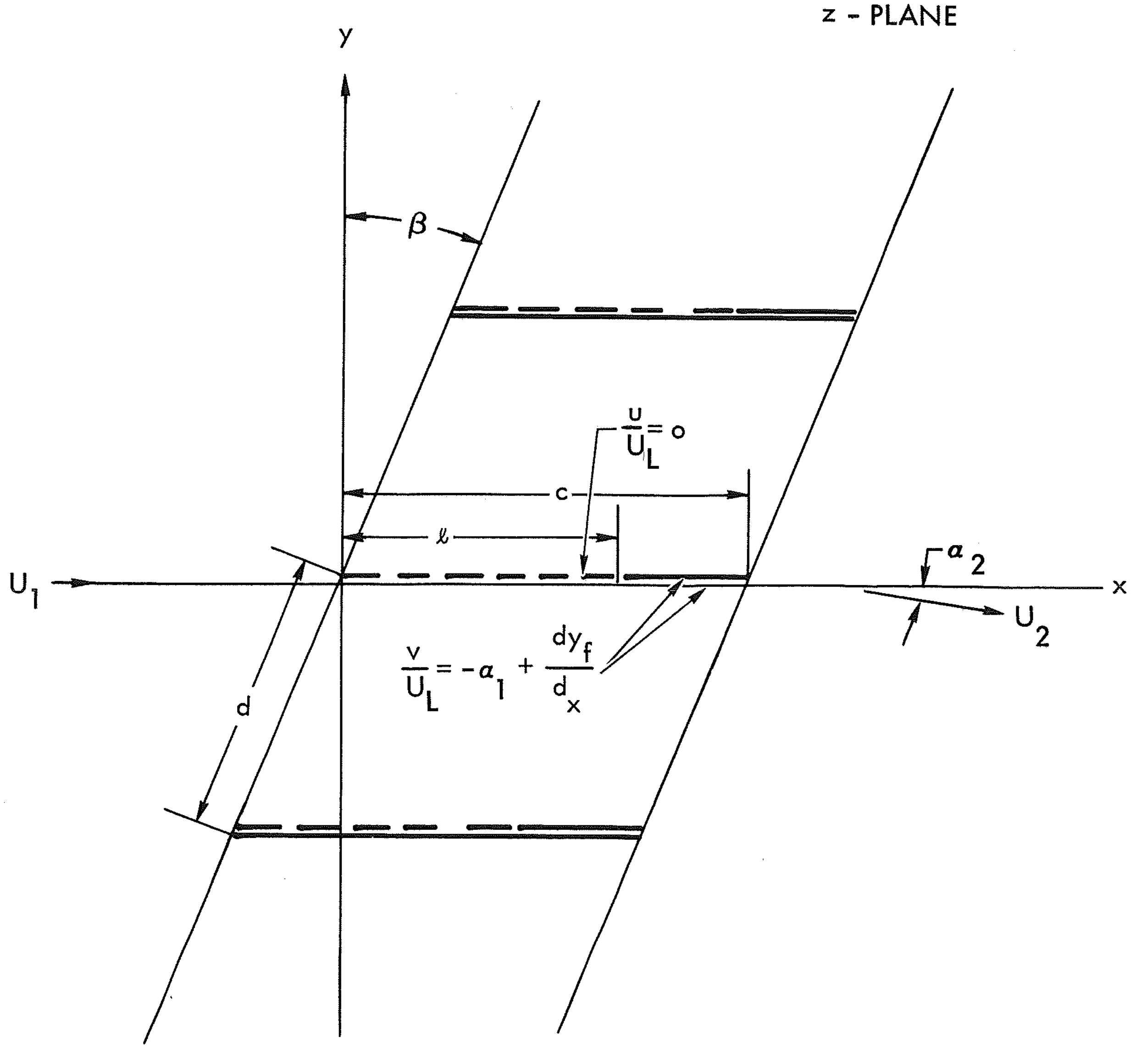

FIGURE 35 - LINEARIZED BOUNDARY VALUE PROBLEM IN THE PHYSICAL PLANE FOR A PARTIALLY CAVITATING CASCADE

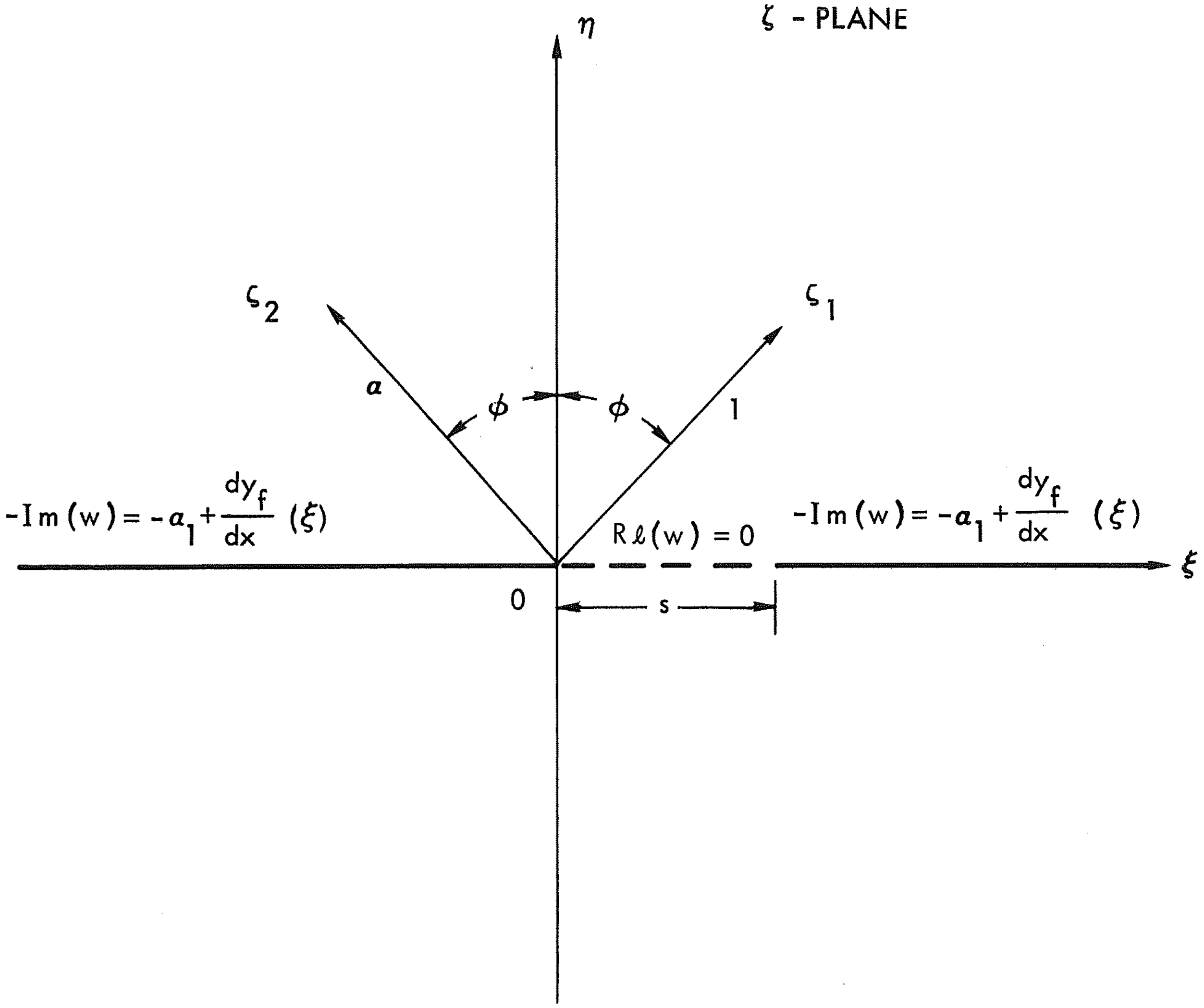

FIGURE 36 - LINEARIZED BOUNDARY VALUE PROBLEM IN THE TRANSFORMED PLANE FOR A PARTIALLY CAVITATING CASCADE

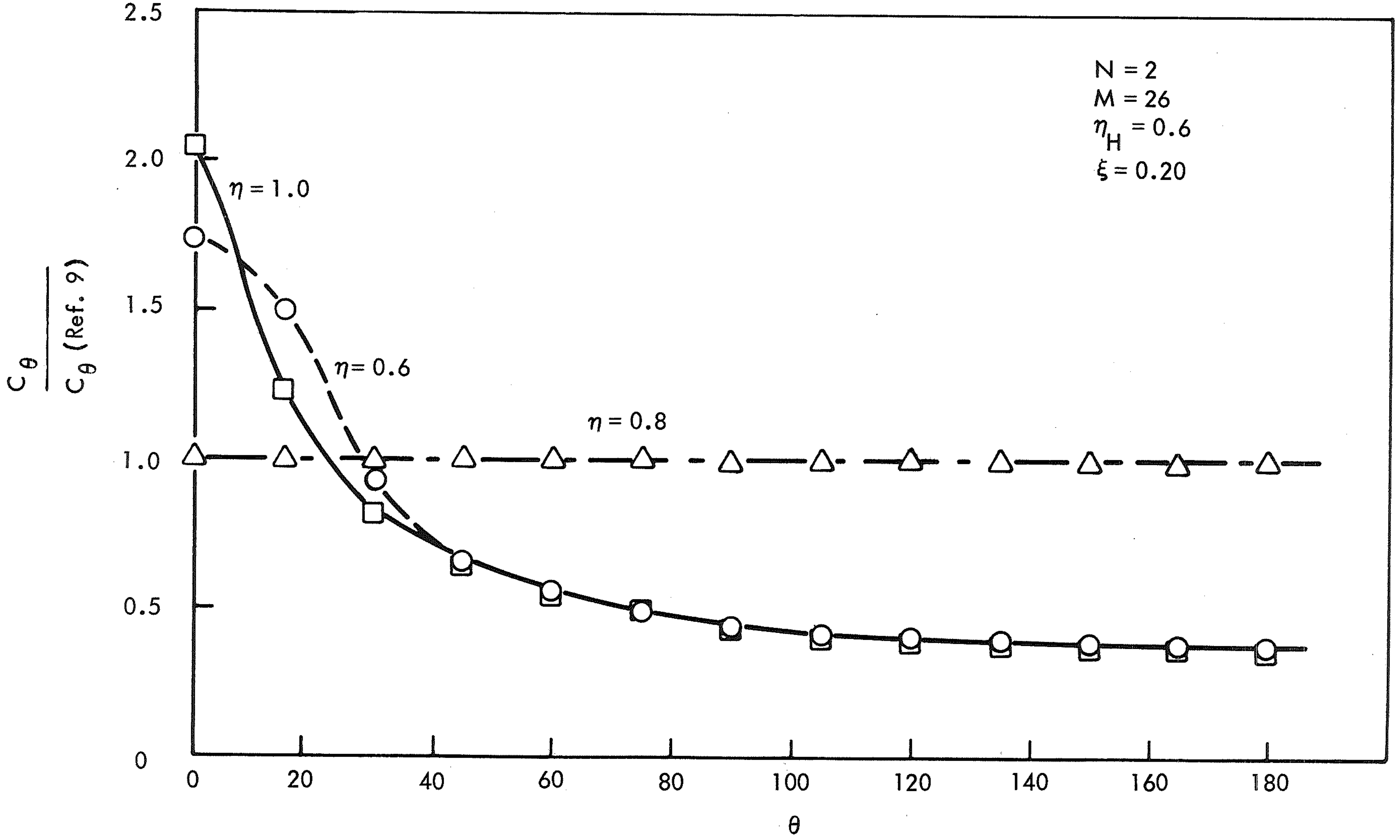

FIGURE 37 - COMPARISON OF THREE-DIMENSIONAL TANGENTIAL VELOCITY TO THE RESULTS OF REFERENCE (9), N = 2, M = 26, $\xi = 0.20$, $\eta_H = 0.60$

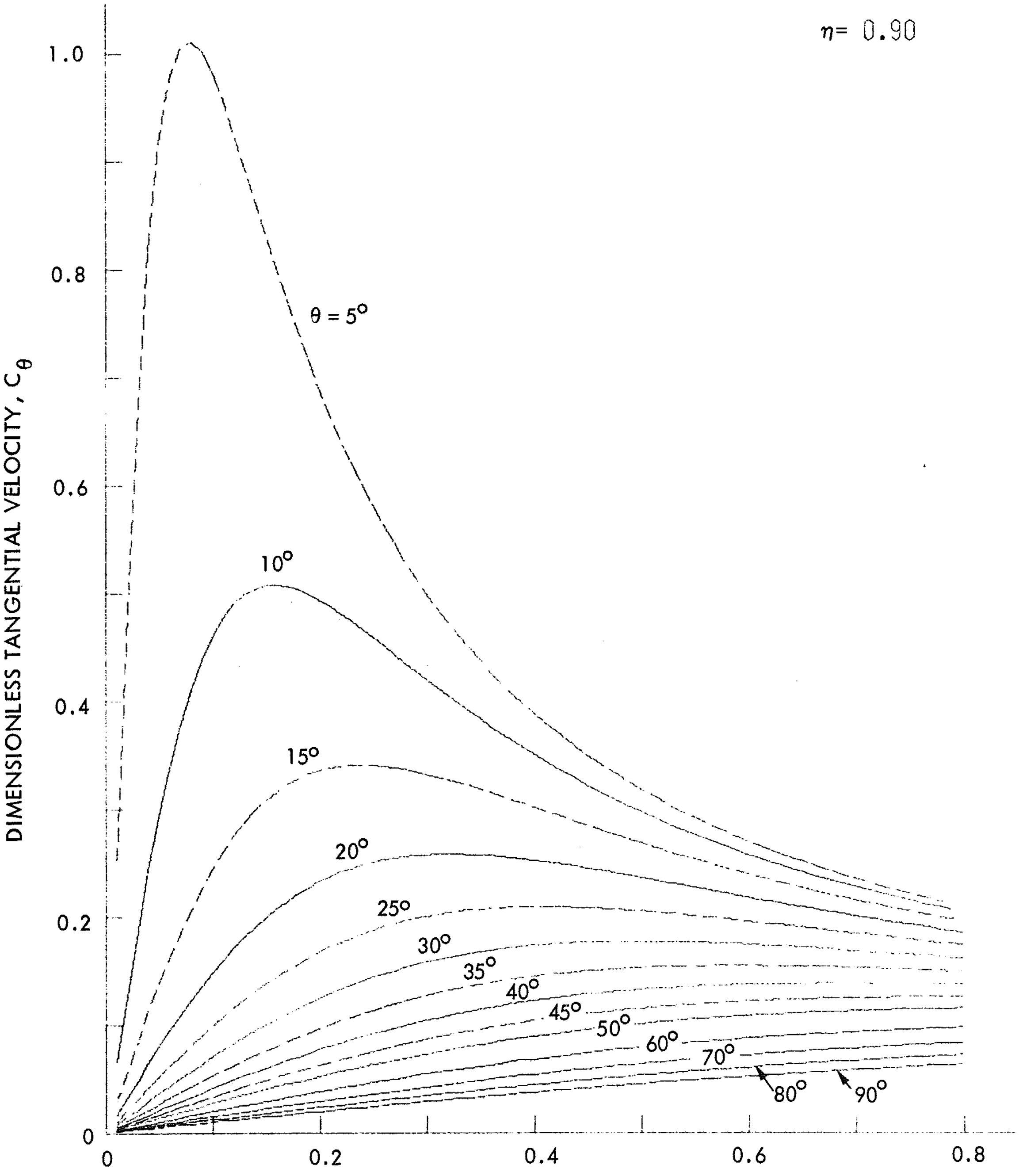

FIGURE 38 - TWO-DIMENSIONAL SOLUTION OF TANGENTIAL VELOCITY FOR η = 0.90

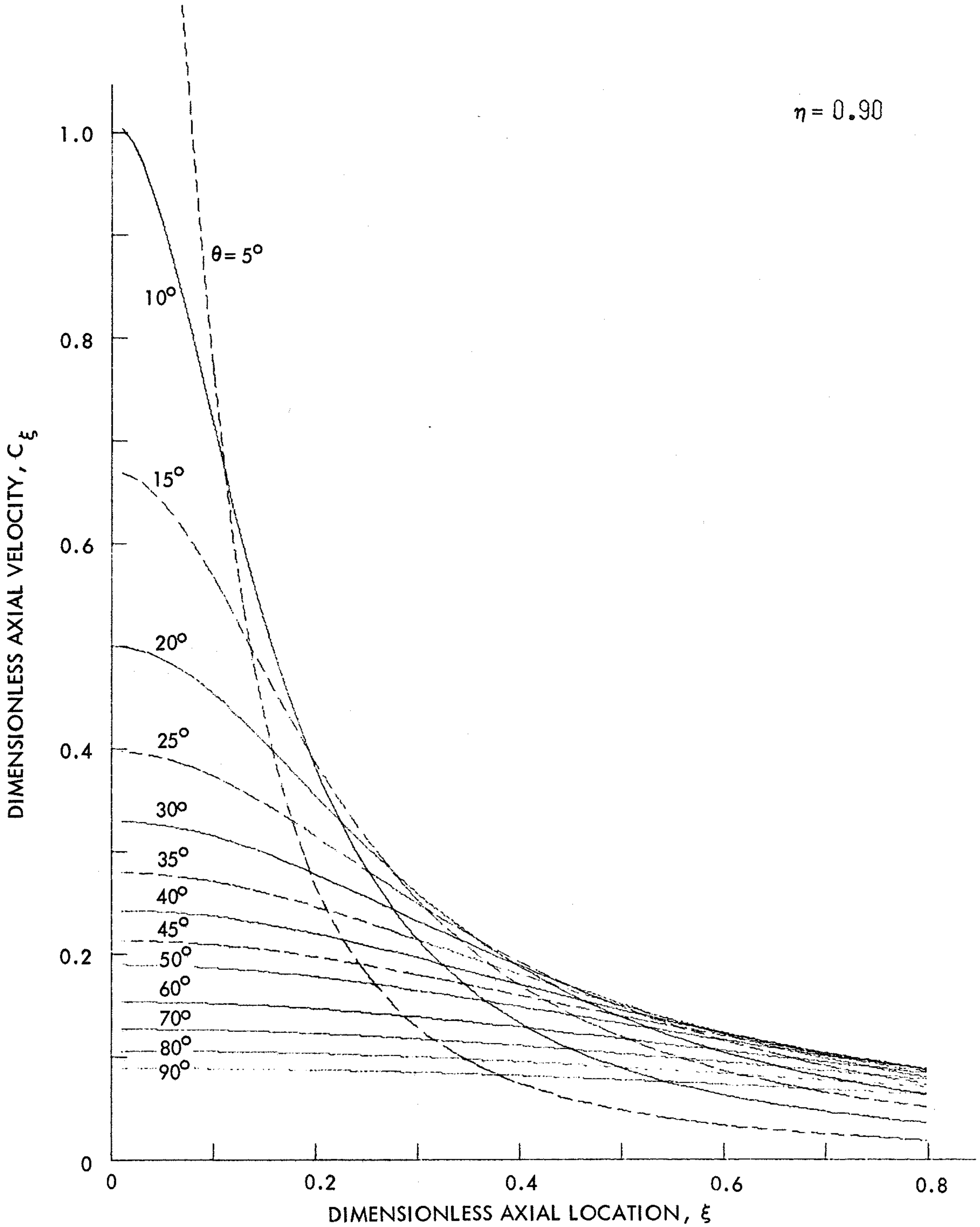

FIGURE 39 - TWO-DIMENSIONAL SOLUTION OF AXIAL VELOCITY FOR $\eta = 0.90$

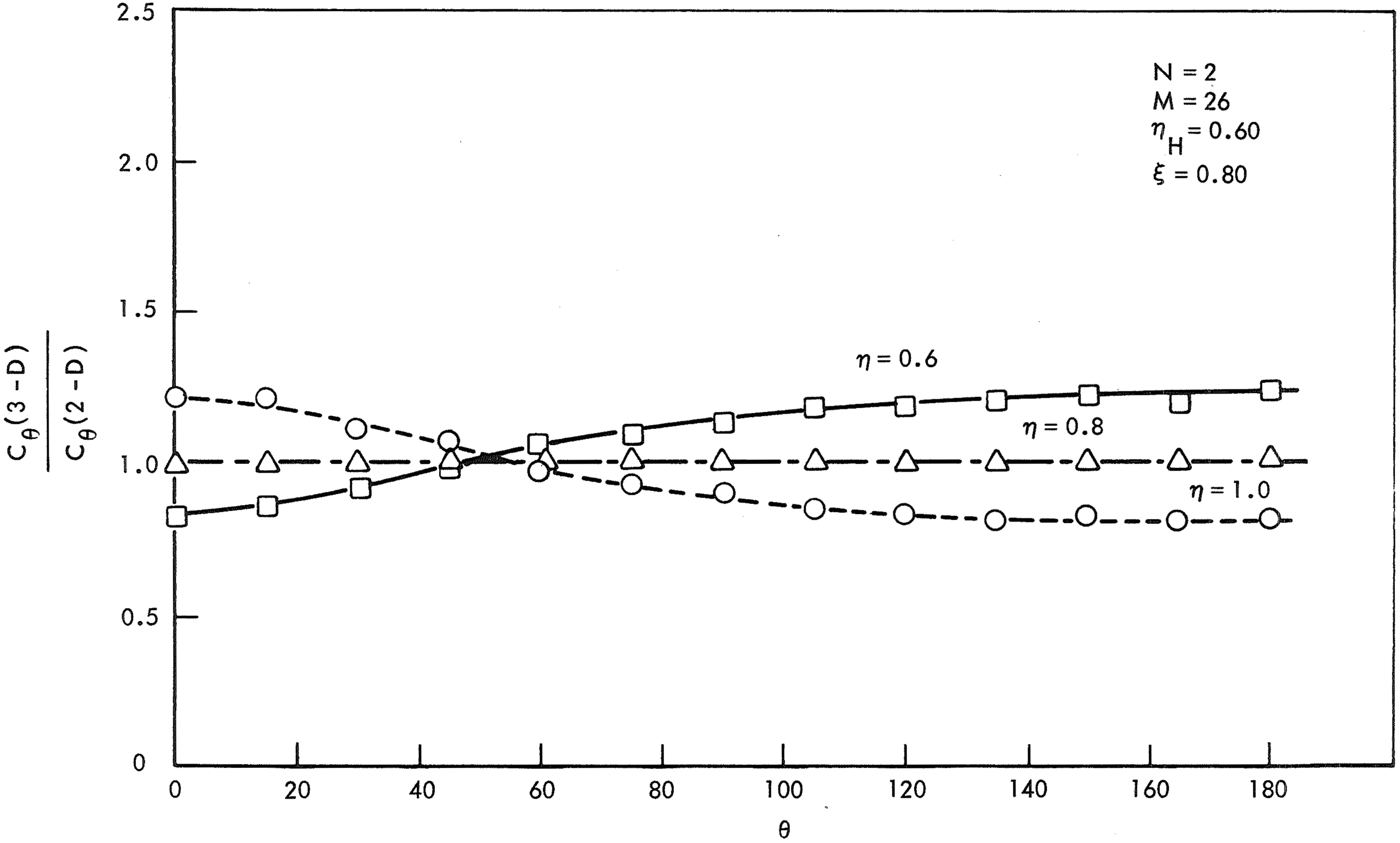

FIGURE 40 - COMPARISON OF THREE-DIMENSIONAL TANGENTIAL VELOCITY THE APPROXIMATE TWO-DIMENSIONAL SOLUTION N = 2, M = 26, $\xi = 0.800$, $\eta_H = 0.600$

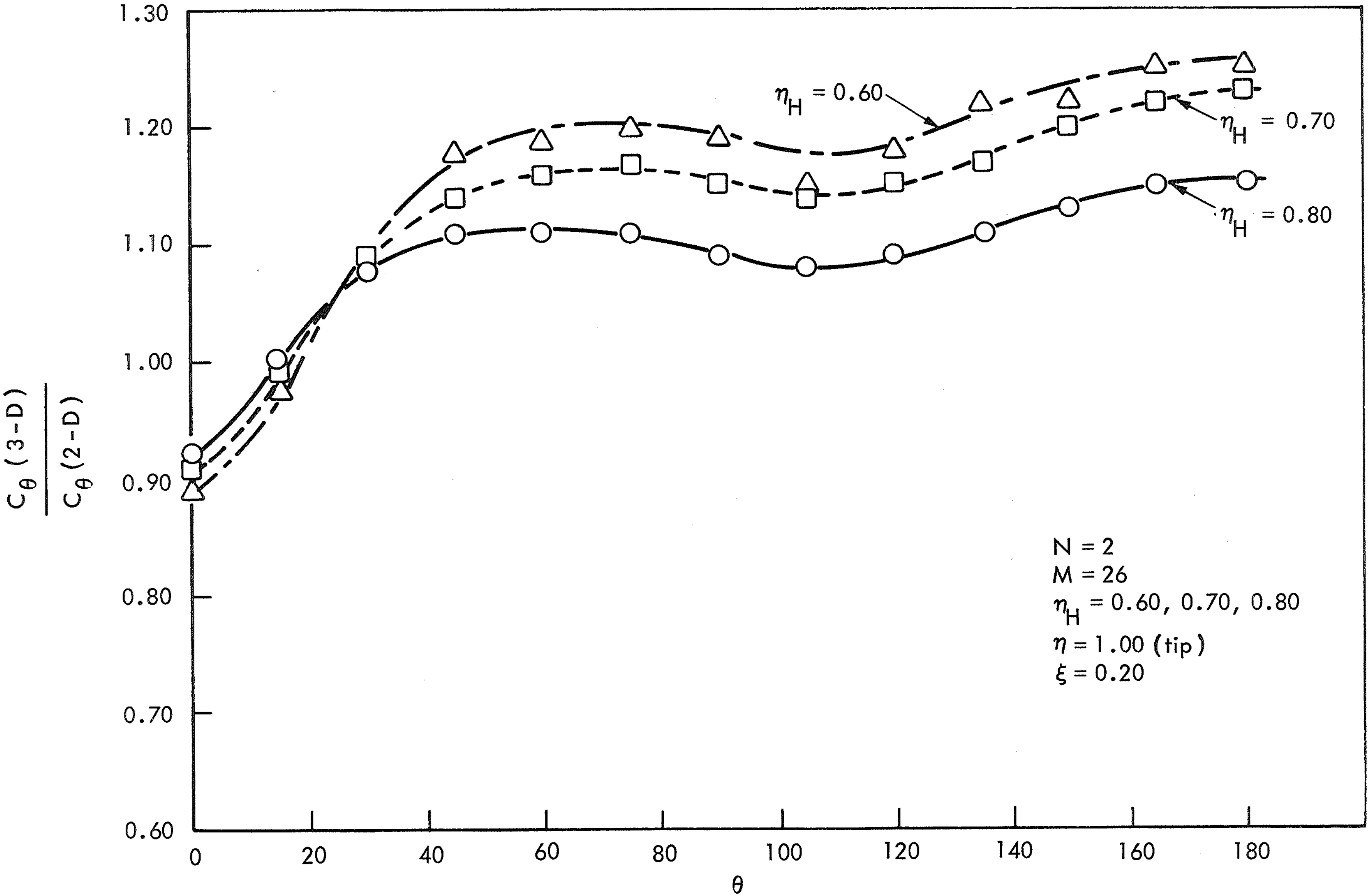

FIGURE 41 - INFLUENCE OF HUB RATIO ON THE RATIO OF THREE DIMENSIONAL TANGENTIAL VELOCITY TO THE APPROXIMATE TWO-DIMENSIONAL SOLUTION AT THE TIP RADIUS

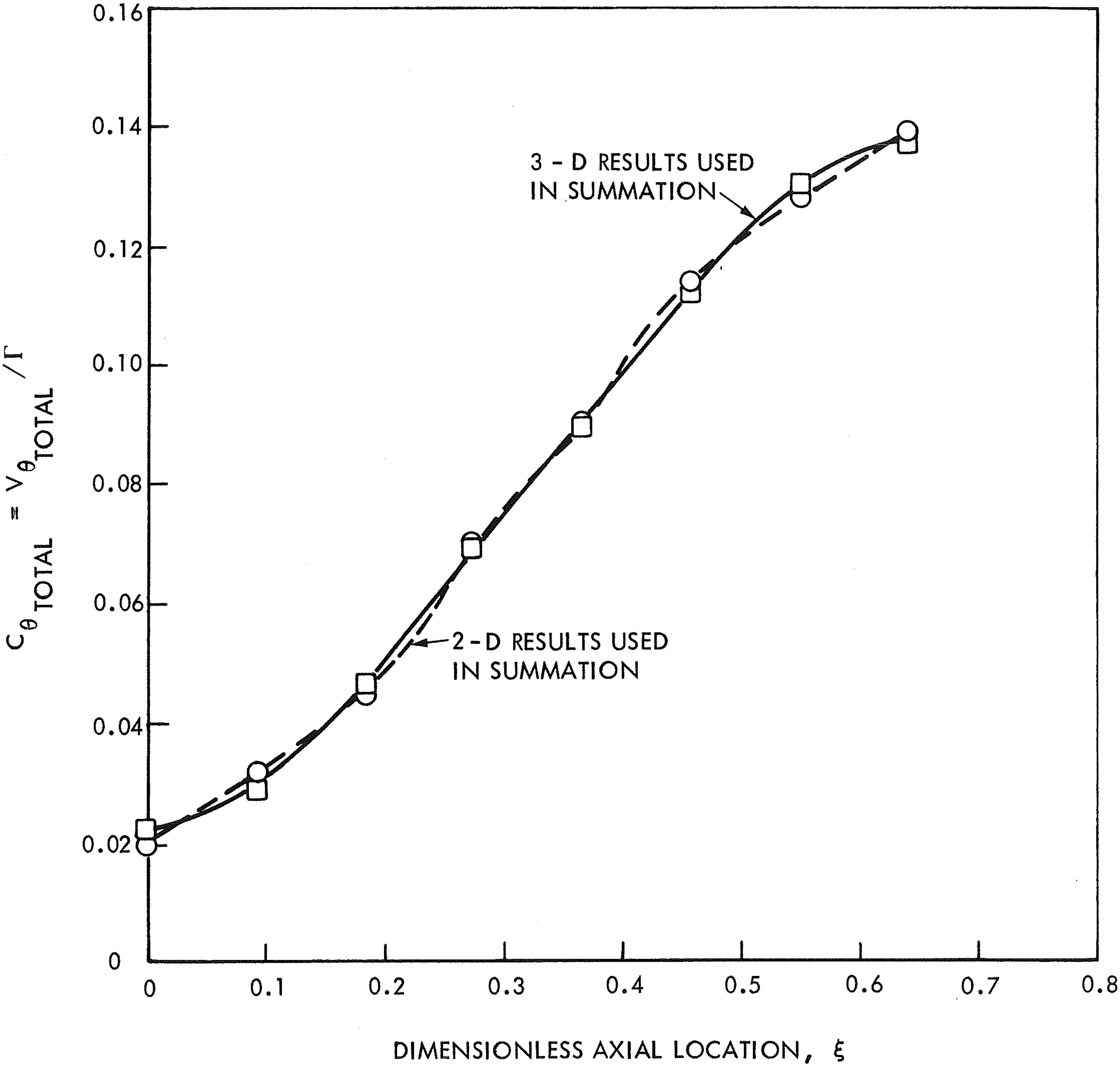

FIGURE 42 - SAMPLE INTERFERENCE STREAMLINE CALCULATION USING BOTH TWO AND THREE DIMENSIONAL RESULTS

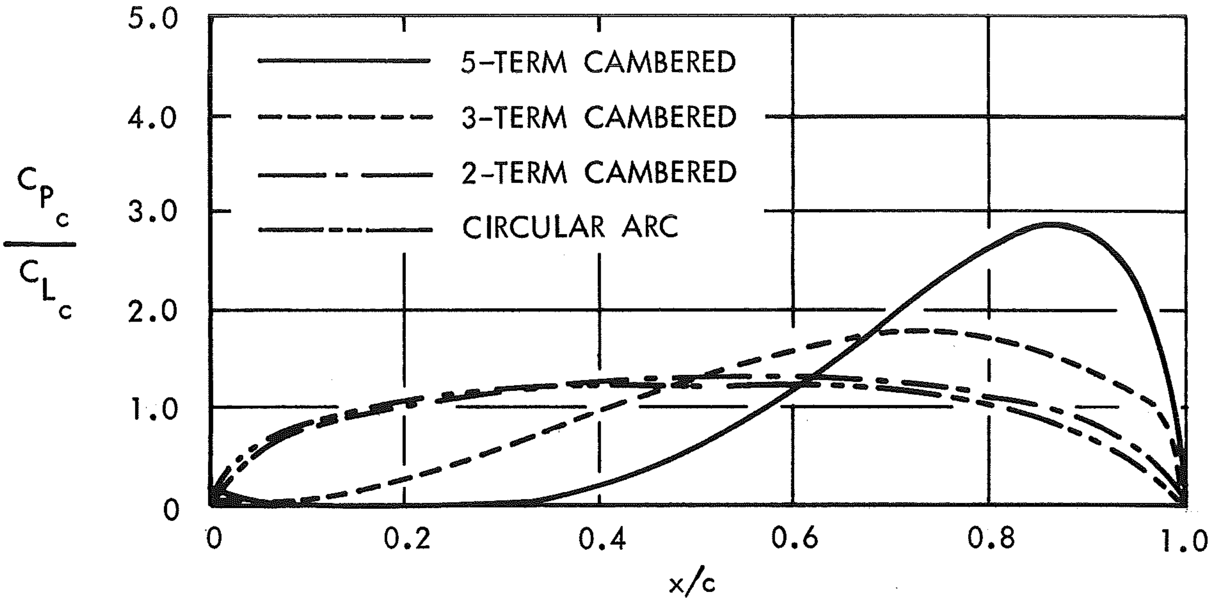

(a) CONTRIBUTION DUE TO CAMBER

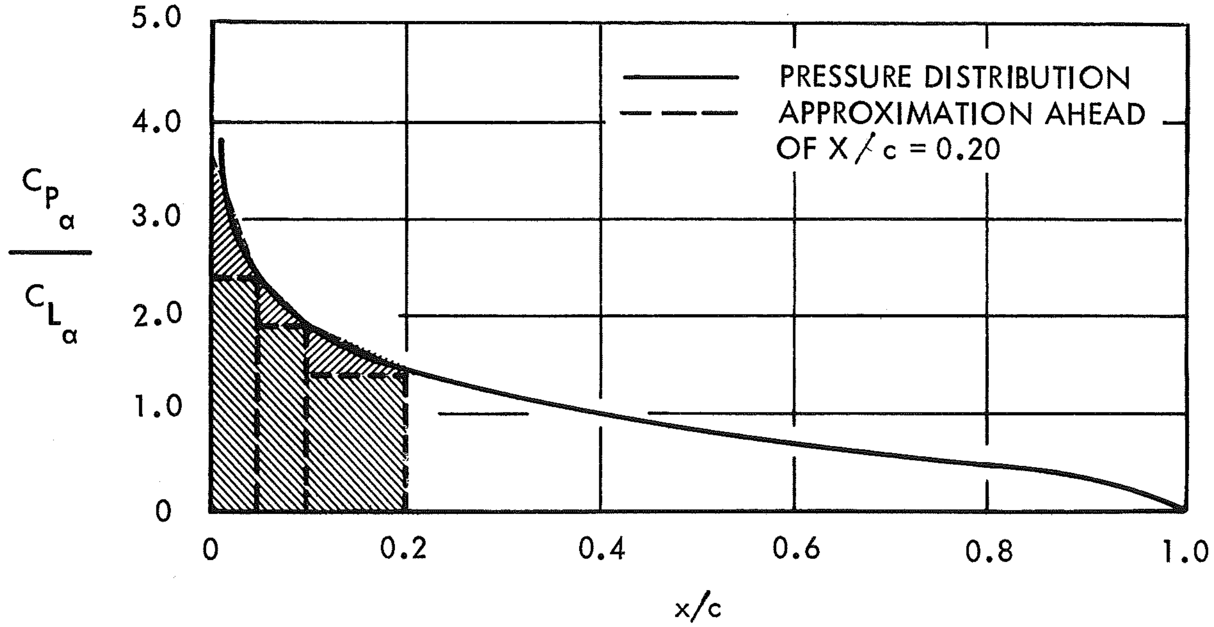

(b) CONTRIBUTION DUE TO ANGLE OF ATTACK

FIGURE 43 – PRESSURE DISTRIBUTION ON FOUR TYPES OF ISOLATED FOIL PROFILES (AFTER REF (6))

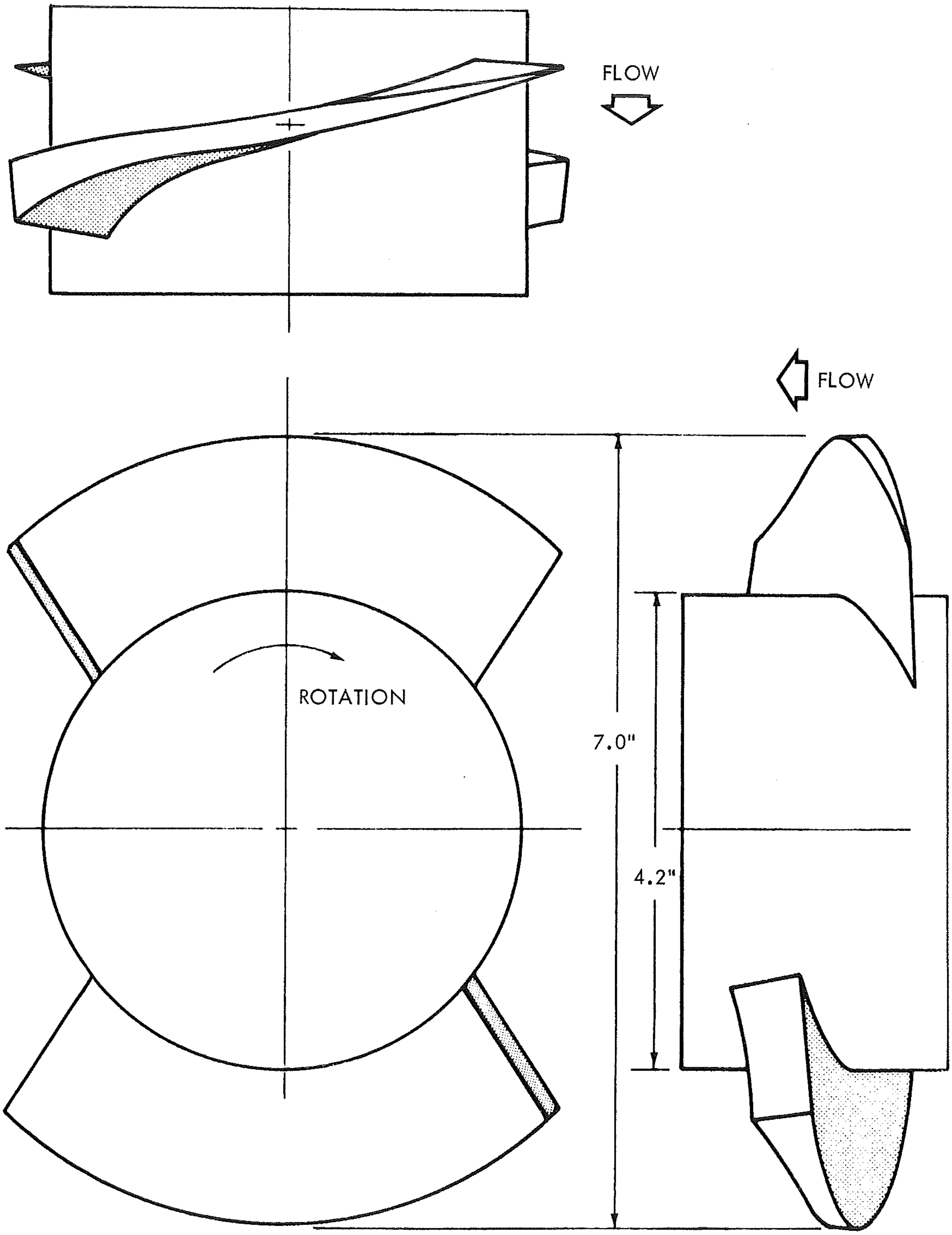

FIGURE 44 - THREE VIEWS OF THE FIVE-TERM CAMBERED, TWO-BLADED FIRST STAGE IMPELLER

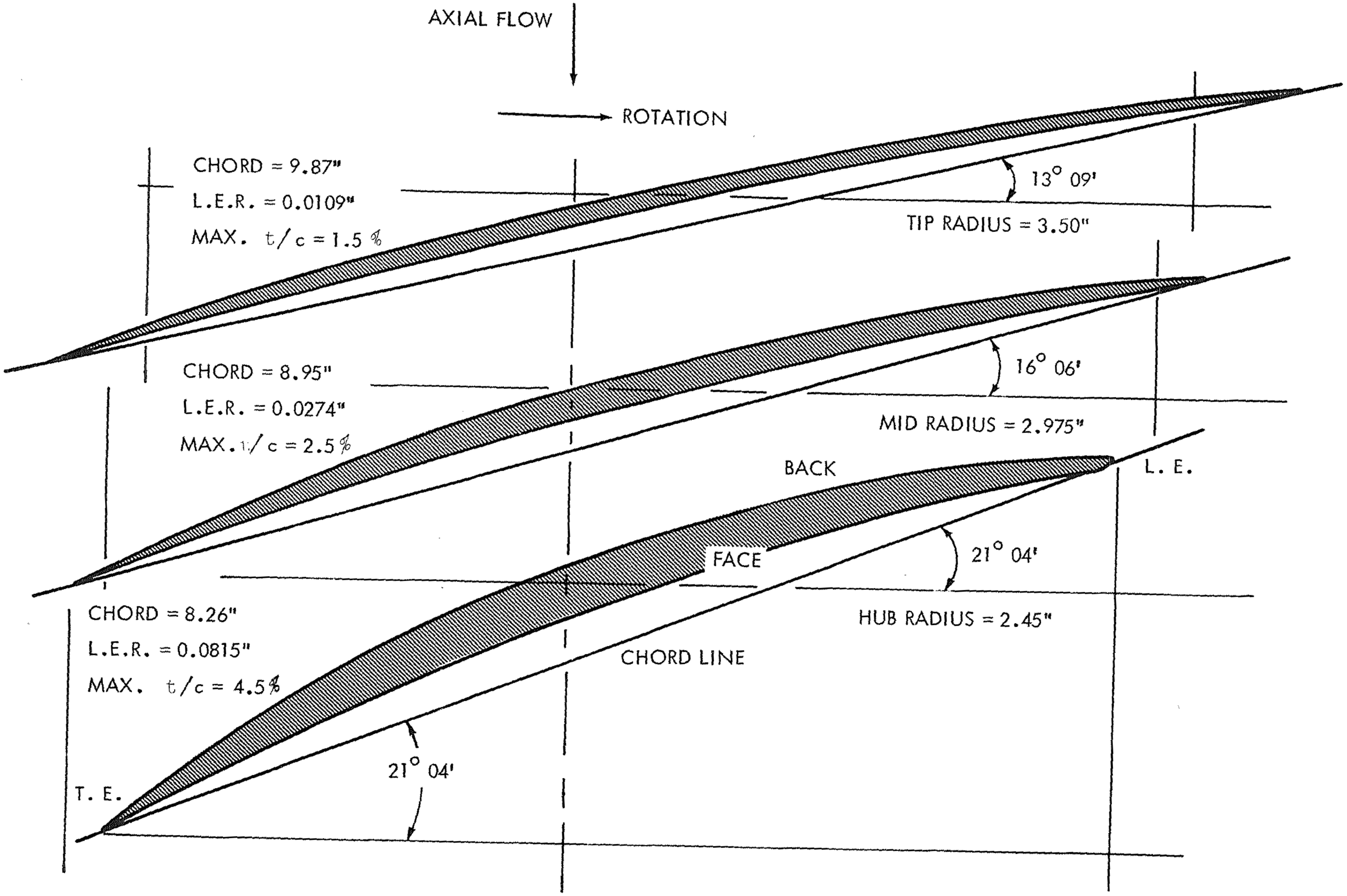

FIGURE 45 - SECOND STAGE TWO DIMENSIONAL BLADE PROFILES AT THREE RADII.
(FOUR BLADES, 0.70 HUB)

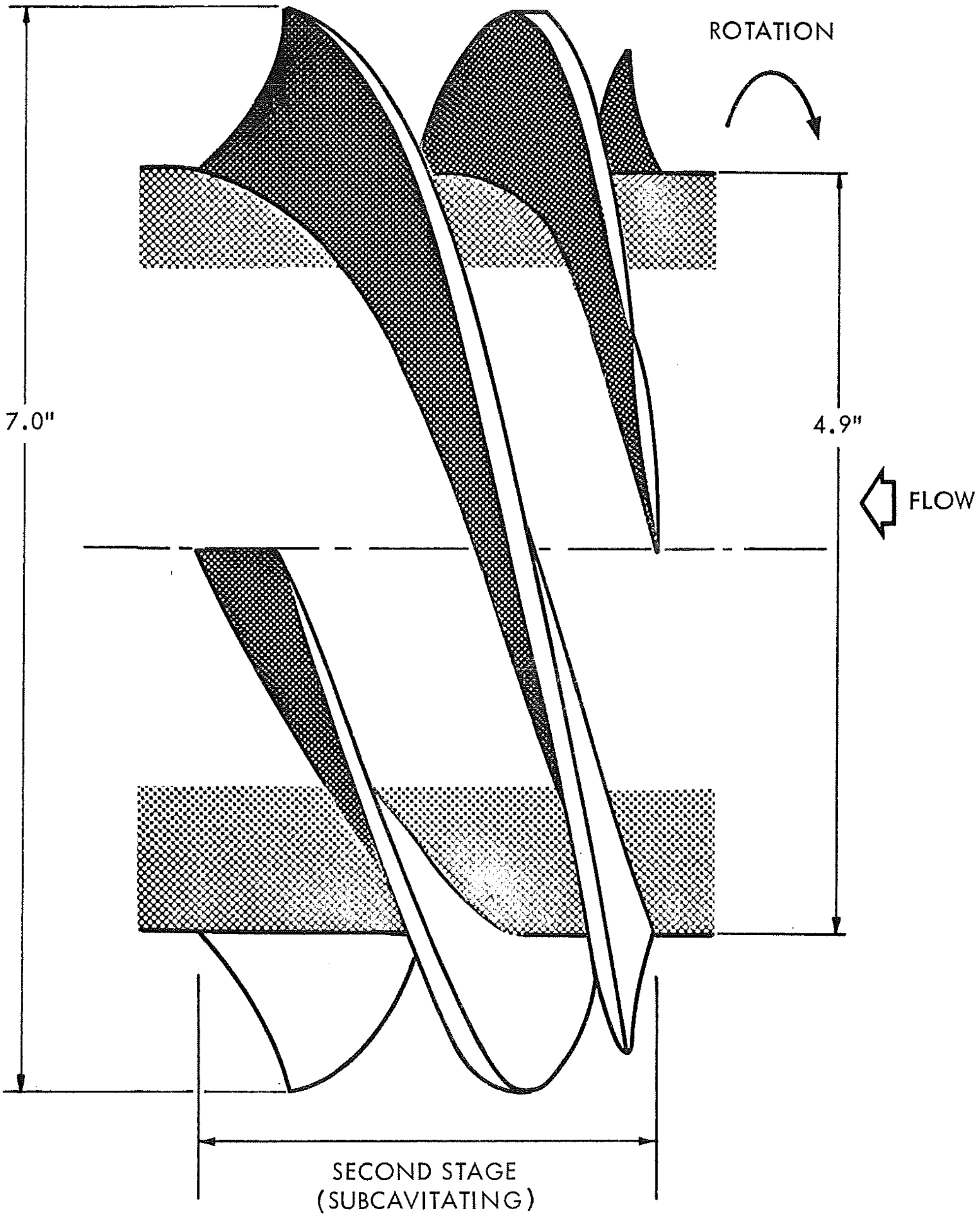

FIGURE 46 - SECOND STAGE IMPELLER USING FOUR BLADES AND 0.70 HUB

DISTRIBUTION LIST
Contract No. NAS 8-20625

NASA Marshall Space Flight Center
Huntsville, Alabama 35812
Attn: Code PR-RC 1
Code MS-DL 1
Technology Utilization Office, MS-T 1
Code MS-I 1
Loren A. Gross, S and E-ASTN-PPA 1
Technical Manager, S and E-ASTN-PPA 2
Dale Burrows, S and E-ASTN-PJ 1
Office of Tech. Inf. MS-IP 2
Technical Library 1
Purchasing Office, PR-EC 1
Patent Office, M-PAT 1

Fort Holabird
Baltimore, Maryland 21219
Attn: Code DCASA (DCRP-DB) 1

Chief, Liquid Propulsion Technology, RPL
Office of Advanced Res. and Tech.
NASA Headquarters
Washington, D. C. 20546 3

Director
Technology Utilization Division
Office of Tech. Utilization
NASA Headquarters
Washington, D C. 20546 1

NASA Scientific and Tech. Inf. Facility
P. O. Box 33
College Park, Maryland 20740 73

Director
Launch Vehicles and Prop, SV
Office of Space Science and Applications
NASA Headquarters
Washington, D. C. 20546 1

Director
Advanced Manned Missions, MT
Office of Manned Space Flight
NASA Headquarters
Washington, D. C. 20546 1

Mission Analysis Division
NASA Ames Research Center
Moffett Field, Calif. 24035 1

NASA Ames Research Center
Moffett Field, Calif. 94035
Attn: Hans M. Mark 1

Goddard Space Flight Center
Greenbelt, Maryland 20771
Attn: Merland L. Moseson Code 620 1

Jet Propulsion Laboratory
Calif. Inst. of Technology
4800 Oak Grove Drive
Pasadena, Calif. 91103
Attn: Henry Burlage, Jr. Prop. Div. 38 2

Langley Research Center
Langley Station
Hampton, Virginia 23365
Attn: Ed. Cortwright, Dir. 2

Lewis Research Center
21000 Brookpark Road
Cleveland, Ohio 44135
Attn: Dr. A. Silverstein, Dir. 2

Manned Spacecraft Center
Houston, Texas 77001
Attn: Joseph G. Thibodaux, Jr.
Chief, Prop. and Power
Division 2

John F. Kennedy Space Center
NASA
Cocoa Beach, Florida 32931
Attn: Dr. Kurt H. Debus 1

Georgia Institute of Technology
Atlanta, Georgia 30332 1

Pennsylvania State University
State College, Penn.
Attn: Dr. W. Holl 19111 1

Iowa State University
Ames, Iowa
Attn: Dr. George Serovy 52241 1

Calif. Inst. of Technology
Pasadena, Calif.
Attn: Dr. Acosta 91101 1

Naval Postgraduate Training Center
Monterey, Calif.
Attn: Dr. Vavra 93940 1

Dr. George Wislicenus
4641 Coronado Drive
Tucson, Arizona 85718 1

Case Western Reserve Univ.
University Circle
Cleveland, Ohio 44106
Attn: Dr. E. Resnotko 1

Stanford University
Palo Alto, California 94305
Attn: Dr. S. Kline 1

University of Michigan
Ann Arbor, Michigan
Attn: Dr. F.G. Hammitt 48108 1

Mass. Inst. of Technology
Cambridge, Mass. 02139
Attn: Dr. Mann 1

Purdue University
Layfayette, Indiana 47907
Dr. Bruce Reese 1

Cornell University
Ithaca, New York 14850
Attn: Dr. D.L. Turcott 1

Rensselaer Polytechnic Inst.
Troy, New York 12181
Attn: Dr. Foa 1

Princeton University
Princeton, New Jersey 08540
Attn: Dr. G.L. Mellor 1

Mr. Werner Britsch
Lewis Research Center
Mail Stop 500-209
Cleveland, Ohio 44135 1